

AD-767 240

A MATHEMATICAL MODEL OF UNSTEADY
AERODYNAMICS AND RADIAL FLOW FOR
APPLICATION TO HELICOPTER ROTORS

Ronald E. Gormont

Boeing Vertol Company

Prepared for:

Army Air Mobility Research and Development
Laboratory

May 1973

DISTRIBUTED BY:

NTIS

National Technical Information Service
U. S. DEPARTMENT OF COMMERCE
5285 Port Royal Road, Springfield Va. 22151

AD

USAAMRDL TECHNICAL REPORT 72-67

A MATHEMATICAL MODEL OF UNSTEADY AERODYNAMICS AND RADIAL FLOW FOR APPLICATION TO HELICOPTER ROTORS

AD 767240

By

Ronald E. Gormont

May 1973

EUSTIS DIRECTORATE

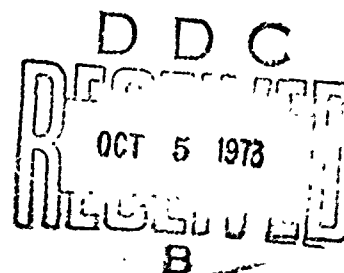
U. S. ARMY AIR MOBILITY RESEARCH AND DEVELOPMENT LABORATORY
FORT EUSTIS, VIRGINIA

CONTRACT DAAJ02-71-C-0045
THE BOEING COMPANY, VERTOL DIVISION
PHILADELPHIA, PENNSYLVANIA

Approved for public release;
distribution unlimited.



NATIONAL TECHNICAL
INFORMATION SERVICE



DISCLAIMERS

The findings in this report are not to be construed as an official Department of the Army position unless so designated by other authorized documents.

When Government drawings, specifications, or other data are used for any purpose other than in connection with a definitely related Government procurement operation, the U.S. Government thereby incurs no responsibility nor any obligation whatsoever; and the fact that the Government may have formulated, furnished, or in any way supplied the said drawings, specifications, or other data is not to be regarded by implication or otherwise as in any manner licensing the holder or any other person or corporation, or conveying any rights or permission, to manufacture, use, or sell any patented invention that may in any way be related thereto.

Trade names cited in this report do not constitute an official endorsement or approval of the use of such commercial hardware or software.

DISPOSITION INSTRUCTIONS

Destroy this report when no longer needed. Do not return it to the originator.

ACCESSION 100	
NTIS	White Section <input checked="" type="checkbox"/>
DDC	Blue Section <input type="checkbox"/>
UNANNOUNCED	<input type="checkbox"/>
JUSTIFICATION	
BY	
DISTRIBUTION AVAILABILITY CODES	
Dist.	Special
A	

Unclassified

Security Classification

DOCUMENT CONTROL DATA - R & D		
(Security classification of title, body of abstract and indexing annotation must be entered when the overall report is classified)		
1. ORIGINATING ACTIVITY (Corporate author) The Boeing Company, Vertol Division Boeing Center, P.O. Box 16858 Philadelphia, Pa.		2a. REPORT SECURITY CLASSIFICATION Unclassified
		2b. GROUP
3. REPORT TITLE A MATHEMATICAL MODEL OF UNSTEADY AERODYNAMICS AND RADIAL FLOW FOR APPLICATION TO HELICOPTER ROTORS		
4. DESCRIPTIVE NOTES (Type of report and inclusive dates) Final Report (May 1971 - July 1972)		
5. AUTHOR(S) (First name, middle initial, last name) Ronald E. Gormont		
6. REPORT DATE May 1973	7a. TOTAL NO. OF PAGES 145	7b. NO. OF REFS 28
8a. CONTRACT OR GRANT NO. DAAJ02-71-C-0045		9a. ORIGINATOR'S REPORT NUMBER(S) USAAMRDL Technical Report 72-67
b. PROJECT NO. Task 1F162204AA4101		9b. OTHER REPORT NO(S) (Any other numbers that may be assigned this report)
c.		Boeing D210-10492-1
d.		
10. DISTRIBUTION STATEMENT Approved for public release; distribution unlimited.		
11. SUPPLEMENTARY NOTES		12. SPONSORING MILITARY ACTIVITY Eustis Directorate, U.S. Army Air Mobility Research and Development Laboratory, Fort Eustis, Virginia
13. ABSTRACT <p>This report documents the development of a mathematical model which represents force coefficients acting on an airfoil in an unsteady environment. In addition, the model is extended to account for the three-dimensional effects of radial flow experienced by rotor blade sections. The methods developed in this report are aimed at obtaining improved capability for predicting rotor blade section force coefficients, particularly at or above stall conditions. The mathematical model has been incorporated into the Government's Rotorcraft Flight Simulation Program C-81 (AGAJ71 version). The mathematical model was correlated with two-dimensional oscillating airfoil test data, and the Government's Rotorcraft Flight Simulation Program C-81 (AGAJ71 version) was correlated with full scale and model rotor test data. The results of the correlation indicate substantial improvement in rotor prediction capability at high speeds and rotor thrust coefficients above stall.</p>		

DD FORM 1473
1 NOV 65

30
11

Unclassified
Security Classification

Unclassified
Security Classification

14.	KEY WORDS	LINK A		LINK B		LINK C	
		ROLE	WT	ROLE	WT	ROLE	WT
	Unsteady Aerodynamics Rotor Blade Section Stall Rotor Blade Radial Flow Three-Dimensional Effect Dynamic Stall						

110

Unclassified
Security Classification



DEPARTMENT OF THE ARMY
U. S. ARMY AIR MOBILITY RESEARCH & DEVELOPMENT LABORATORY
EUSTIS DIRECTORATE
FORT EUSTIS, VIRGINIA 23604

This report has been reviewed by the Eustis Directorate,
U. S. Army Air Mobility Research and Development Laboratory,
and is considered to be technically sound.

The report documents the development of a mathematical
model that represents force coefficients acting on an airfoil
in an unsteady environment. The report is published for the
exchange of information and the stimulation of ideas.

The program was conducted under the technical management
of Mr. G. Thomas White of the Technology Applications
Division of this Directorate.

Task 1F162204AA4101
Contract DAAJ02-71-C-0045
USAAMRDL Technical Report 72-67
May 1973

A MATHEMATICAL MODEL OF UNSTEADY AERODYNAMICS
AND RADIAL FLOW FOR APPLICATION TO HELICOPTER ROTORS

Final Report

Boeing Document D210-10492-1

By
Ronald E. Gormont

Prepared by
The Boeing Company, Vertol Division
Philadelphia, Pa.

for

EUSTIS DIRECTORATE
U.S. ARMY AIR MOBILITY RESEARCH AND DEVELOPMENT LABORATORY
FORT EUSTIS, VIRGINIA

Approved for public release;
distribution unlimited.

cc/
11b

SUMMARY

This report documents the development of a mathematical model which represents force coefficients acting on an airfoil in an unsteady environment. In addition, the model is extended to account for the three-dimensional effects of radial flow experienced by rotor blade sections. The methods developed in this report are aimed at obtaining improved capability for predicting rotor blade section force coefficients, particularly at or above stall conditions. The mathematical model has been incorporated into the Government's Rotorcraft Flight Simulation Program C-81 (AGAJ71 version).

The mathematical model was correlated with two-dimensional oscillating airfoil test data, and the Government's Rotorcraft Flight Simulation Program C-81 (AGAJ71 version) was correlated with full-scale and model rotor test data. The results of the correlations indicate substantial improvement in rotor prediction capability at high speeds and rotor thrust coefficients above stall.

FOREWORD

This report presents the results of rotorcraft methods development conducted under Contract DAAJ02-71-C-0045, Task 1F162204AA4101. The work was performed by The Vertol Division of The Boeing Company and was funded by the Eustis Directorate, U.S. Army Air Mobility Research and Development Laboratory (USAAMRDL). The contract covered the period May 1971 through July 1972. Ronald E. Gormont was the Vertol Project Engineer; W.D. Vann and G.T. White monitored the contract for the Eustis Directorate.

The scope of the contract work included:

- review of available analytical methods for representing unsteady aerodynamics,
- selection of the most appropriate representation based on correlation with existing two-dimensional oscillating airfoil test data and requirements of the USAAMRDL C-81 Rotorcraft Flight Simulation digital computer program,
- development of the selected representation for incorporation in the C-81 (AGAJ71 version) program, and
- development and incorporation of a method for representing radial flow effects.

This effort was conducted as part of USAAMRDL's continuing effort to improve analytical prediction methodologies for design and evaluation of rotorcraft.

The author gratefully acknowledges the assistance of F.D. Harris, Manager of the Boeing V/STOL Wind Tunnel, and F.J. Marzanin, Jr., Senior Engineer in Vertol Division's Rotor Systems Group, for their technical comments, and Mr. T. Moffa, Boeing Computer Services, for incorporating the program revisions in the C-81 analysis.

This report is intended to provide a theoretical background of the work conducted under the contract, and to serve as a user's manual for operation of the revised Rotorcraft Flight Simulation Program.

TABLE OF CONTENTS

	<u>Page</u>
SUMMARY	iii
FOREWORD	v
LIST OF ILLUSTRATIONS	viii
LIST OF SYMBOLS	xi
INTRODUCTION	1
SURVEY OF UNSTEADY AERODYNAMICS METHODS	4
DESCRIPTION AND DEVELOPMENT OF SELECTED UNSTEADY AERODYNAMICS METHOD	13
Incompressible Potential Flow Solution of Oscillating Airfoils	13
Modification to Compressible Flow and Rotating Environment	22
Stall Hysteresis Representation	32
RADIAL FLOW REPRESENTATION	45
Review of Radial Flow Methods	45
The Effects of Radial Flow	48
Effect of Radial Flow on Drag	48
Effect of Radial Flow on Lift	54
USER'S MANUAL	58
Revised Input Requirements	58
Program Flow for Revised Areas	59
Numerical Stability and Effect of Unsteady Aerodynamics on C-81 Convergence	61
LITERATURE CITED	62
APPENDIXES	
I. Correlation of Theory and Two-Dimensional Oscillating Airfoil Test Data	66
II. Correlation of Theory With Isolated Rotor and Helicopter Test Data	105
III. Sample Input and Output	126
DISTRIBUTION	132

LIST OF ILLUSTRATIONS

<u>Figure</u>		<u>Page</u>
1	Theory of Ericsson and Reding	5
2	Comparison of Oscillating Airfoil Data and Carta Reconstructed Data	8
3	Engineering Approximation Accounting for Potential Flow Unsteady Aerodynamics Below Stall	9
4	Improved Prediction of Rotor Performance	10
5	Theodorsen's Sign Conventions	15
6	Theodorsen Unsteady Aerodynamic Functions	17
7	Effective Blade Element Pitch Rate Due to Blade Coning	24
8	Velocity Components at Rotor	26
9	Blade Element Angle of Attack Assumptions	29
10	Typical Pitch Oscillation Test Data	34
11	Typical Dynamic Stall	35
12	Schematic of Stall Hysteresis Formulation	37
13	Stall Delay Functions	40
14	Influence of Empirical K_1 Factor on Correlation at Negative α	42
15	Blade Velocity Diagram	49
16	Chordwise Pressure Distributions of a 9-Percent-Thick Symmetric Hyperbolic Profile Having a t/c_{max} at 40- Percent Chord (Reference 15)	51
17	Effect of Reynolds Number on C_d	55
18	Yawed Flow Effects Delaying Stall	56
19	Flow Paths for the C-81 Rotor Analysis	60
20	Dynamic Loops for the V23010-1.58 Airfoil in Forced Pitch Oscillation	67

<u>Figure</u>		<u>Page</u>
21	Dynamic Loops for the NACA 0012 MOD Airfoil in Forced Pitch Oscillation	76
22	Dynamic Loops for the V13006-.7 Airfoil in Forced Pitch Oscillation	82
23	Dynamic Loops for the NACA 0006 Airfoil in Forced Pitch Oscillation	87
24	Dynamic Loops for the NACA 0012 MOD Airfoil in Forced Pitch Oscillation	95
25	Dynamic Loops for the V23010-1.58 Airfoil in Translation . .	100
26	Model Rotor Correlation With Elastic Blade Rotor Theory: Rotor Thrust vs. Control Axis Angle	105
27	Model Rotor Correlation With Elastic Blade Rotor Theory: Rotor Thrust vs. Rotor Propulsive Force	106
28	Model Rotor Correlation With Elastic Blade Rotor Theory: Rotor Thrust vs. Rotor Effective Drag	107
29	Model Rotor Correlation With Rigid Blade Rotor Theory: Rotor Thrust vs. Control Axis Angle	108
30	Model Rotor Correlation With Rigid Blade Rotor Theory: Rotor Thrust vs. Rotor Propulsive Force	109
31	Model Rotor Correlation With Rigid Blade Rotor Theory: Rotor Thrust vs. Rotor Effective Drag	110
32	Model Rotor Correlation With Elastic Blade Rotor Theory: Rotor Thrust vs. Steady Root Torsion Load	111
33	Model Rotor Correlation With Elastic Blade Rotor Theory: Rotor Thrust vs. Alternating Root Torsion Load	112
34	Correlation of Theory and Model Rotor Blade Root Torsion Loads: Blade Root Torsion Load vs. Blade Azimuth Position	113
35	Correlation of Theory and Model Rotor Blade Root Torsion Loads: Blade Root Torsion Load vs. Blade Azimuth Position	114
36	Model Rotor Correlation With Azimuthal Coefficient-of-Lift Variation at .75 Radius	115

<u>Figure</u>		<u>Page</u>
37	Model Rotor Correlation With Azimuthal Coefficient-of-Lift Variation at .75 Radius	116
38	Correlation of Elastic Blade Rotor Theory With UH-1H Test Data	120
39	Correlation of Rigid Blade Rotor Theory With CH-47C Forward Rotor Test Data	121
40	Correlation of Theory With CH-47C Test Data	123
41	Correlation of Theory With CH-47C Pull-Up Maneuver	124
42	Typical Input	127
43	Typical Final Trim Output	130
44	Typical Airloads Output	131

LIST OF SYMBOLS

A	Rotor disc area, πR^2 , ft ²
a	Lift curve slope, C_l/rad , or pitch change axis location from mid chord
B _{1c}	Rotor longitudinal cyclic pitch, deg
b	Airfoil semi-chord, ft
C	Theodorsen's complex function, $F + iG$
C _{DE} /σ	Rotor effective drag coefficient, $D_E/\rho (\Omega R)^2 bcR = P/V_{FLT} (\Omega R)^2 bcR - X/\rho (\Omega R)^2 bcR$
C _c	Section chord force coefficient
C _d	Section drag coefficient
C _f	Flat plate skin friction coefficient
C _l	Section lift coefficient
\overline{C}_l	Collected terms (see Equation 33)
C _m	Section pitching moment coefficient
C _n	Section normal force coefficient
C _T /σ	Rotor thrust coefficient, $T/\rho (\Omega R)^2 bcR$
C _T '/σ	Rotor lift coefficient, $L_R/\rho (\Omega R)^2 bcR$
c	Blade chord, ft
D	Drag per unit span, lb/ft
D _e	Rotor effective drag $P/V_{FLT} - X$, lb
d	Rotor diameter, ft
F	Theodorsen's lift deficiency function, function of k
f	Frequency of oscillation, Hz
G	Theodorsen's phase lag function, function of k
GW	Gross weight, lb
H _D	Density altitude, ft

H_p	Pressure altitude, ft
HP	Horsepower
h	Translational position, positive down, semichords
\dot{h}	Time derivative of h , ft/sec
\ddot{h}	Second time derivative of h , ft/sec ²
i	$\sqrt{-1}$
K_1	Unsteady aero empirical factor for $\dot{\alpha} < 0$
k	Reduced frequency, $\pi f c/V$
L	Lift per unit span, lb/ft
L_R	Rotor lift, lb
M	Pitching moment per unit span, ft-lb/ft
M_N	Local Mach number, V/V_{SOUND}
M_{N1}	Mach number above which γ decreases linearly
$M_{N(\gamma_2=0)}$	Mach number at $\gamma_2=0$
$M(1)(90)$	Advancing tip Mach number $(V_{FLT} + \Omega R)/V_{SOUND}$
n	Load factor
OAT	Outside air temperature, °C
P	Power, ft-lb/sec
PA	Dimensionless pitch change axis location from leading edge
P/q	Pressure coefficient, $(p_{STATIC} - p_o)/q$
P_o	Free stream static pressure, lb/ft ²
p_{STATIC}	Local static pressure, lb/ft ²
q	Dynamic pressure, lb/ft ²
R	Blade radius, ft
R_c	Reynolds number based on chord, $\rho Vc/\mu$
r	Radial distance, ft
T	Rotor thrust, lb

t	Time, sec
t/c	Section thickness ratio
U _P	Perpendicular velocity component, mutually perpendicular to the blade and U _T , ft/sec
U _R	Velocity component along blade span, ft/sec
U _{RESULT}	Resultant velocity, $\sqrt{U_P^2 + U_T^2}$, ft/sec
U _T	Tangential velocity component, perpendicular to blade and in disc plane, ft/sec
U _{TOT}	Total velocity, $\sqrt{U_T^2 + U_R^2}$, ft/sec
V	Blade element resultant velocity, ft/sec
V _{FLT}	Free stream flight velocity, ft/sec
V _Ω	Blade rotational velocity about the shaft, ft/sec
v	Induced velocity, ft/sec
X	Rotor propulsive force, lb
x	Dimensionless radial position, r/R
x/c	Dimensionless chord position
\dot{Z}	Axial flight velocity, ft/sec
α	Angle of attack, deg or rad
$\dot{\alpha}$	Time derivative of angle of attack, rad/sec
α _{CA}	Rotor control axis angle, α _S - B _{1c} , deg
α _S	Shaft angle, positive aft, deg
$\bar{\alpha}$	Collected dynamic angle of attack terms (eqn 48)
β	Rotor blade flap position, rad
γ	Stall delay function, $\Delta\alpha_{STALL}/\Delta \sqrt{\frac{c\dot{\alpha}}{2V}}$, rad
γ ₁	γ at low pitch rates in stall delay formulation
γ ₂	γ at high pitch rates in stall delay formulation

$\Delta\alpha$	Incremental angle of attack, deg or rad
ΔD	Incremental drag, lb
Δh	Magnitude of forced translation motion, semichords
ϵ	Incremental angle, rad
θ	Blade pitch angle, rad
$\dot{\theta}$	Time derivative of blade pitch angle, rad/sec
$\ddot{\theta}$	Second time derivative of blade pitch angle, rad/sec ²
Λ	Yaw angle, $\tan^{-1} \frac{U_R}{U_T}$, deg
μ	Air absolute viscosity, lb-sec/ft ²
μ	Advance ratio, $V_{FLT}/\Omega R$
π	3.14159----
ρ	Air density, slugs/ft ³
σ	Rotor solidity, $bc/\pi R$
ψ	Azimuth position, deg
Ω	Rotor angular speed, rad/sec
ω	Angular velocity, rad/sec
1/rev, 3/rev, etc.	One per revolution, three per revolution, etc.

Subscripts

APP	Apparent
BE	Blade element
CA	Control axis
Cl	Lift coefficient
EQU	Equivalent
FLT	Flight

f	Friction
INT	Interference
L	Lift
M	Moment
MAX	Maximum
O	Average or mean
PA	Pitch axis
P	Perpendicular
p	Pressure
REF	Reference
S	Shaft
SF	Skin friction
T	Tangential
TOT	Total
v	Vibratory
Z	Axial
2-D	Two-dimensional
A	Radial flow

INTRODUCTION

The basis for helicopter rotor loads and performance analysis was formed in the 1920's, when Glauert extended propeller strip theory to the case of rotary wings. Although improvements were made to Glauert's analysis, the assumption of linear lift curve slopes and incompressible drag coefficients remained until the advent of digital computers. The computers permitted the inclusion of static airfoil force coefficients as functions of angle of attack and Mach number.

Rotor analysis methods became more sophisticated when nonuniform downwash and blade elasticity were incorporated. However, the use of static airfoil force coefficients beyond stall angles of attack precluded proper analysis of the rotor when operating at high lift levels. The cause was traced to the omission of dynamic effects due to rate of change of angle of attack. This was first analyzed by Theodorsen and later verified by tests of airfoils undergoing unsteady motions.

In 1969, F. D. Harris³ demonstrated significantly improved correlation of theoretic prediction of rotor stall with rotor test data. He used an analog computer program that incorporated a functional representation of oscillating airfoil data. Since analog computers are not well suited for day-to-day production use and they cannot simulate the effects of nonuniform downwash (more pronounced $\dot{\alpha}$ over the rotor disc), a digital method was developed to predict unsteady airfoil coefficients.

The Eustis Directorate, U. S. Army Air Mobility Research and Development Laboratory, funded the development of methods (reported in this document) to predict rotor performance in the stall regimes. This work produced a mathematical representation which was incorporated in the Government's Rotorcraft Flight Simulation Program C-81 (AGAJ71 version).

The C-81 (AGAJ71 version) digital computer program is a general flight simulation analysis for rotorcraft. It may be used to determine rotorcraft trim, performance, stability, stress loads, and aerodynamic forces in both steady flight and maneuver conditions. The program can be used to analyze single-rotor, tandem-rotor

and side-by-side rotor helicopter configurations as well as isolated wind tunnel model rotors. The rotor blade simulation includes a fully coupled aeroelastic modal analysis. Prior to the work described in this report, the C-81 program had a simplified unsteady aerodynamics representation, but it was not sufficiently rigorous to satisfy the requirements of general rotorcraft configurations. The effort described in this report produced representations for unsteady aerodynamics (including stall hysteresis) and radial flow effects.

The C-81 (AGAJ71 version) digital computer program can be used to analyze the following rotorcraft features:

- Configuration - Single-rotor, tandem-rotor, or side-by-side rotor helicopter. Wind tunnel model rotor simulation.
- Flight condition - Steady flight or time-variant maneuver.
- Phenomena - Rotor and fuselage trim condition, performance, stability, rotor airloads, and stress loads.

The C-81 (AGAJ71 version) digital computer program can be used to analyze the following rotor features:

- Blade Elastic Characteristics - Modal analysis with fully coupled flap-chord-pitch modes.
- Nonuniform Downwash Approximation - Uniform downwash with empirical variation over blade radius and azimuth.
- Rotor Blade Aerodynamics - The program originally represented only simplified unsteady aerodynamics and radial flow effects. As revised herein, the program can represent rigorous, comprehensive, unsteady aerodynamics and radial flow effects. The original program's capability of computing lift, drag, and moment loads at 20 radial stations and at 15-degree azimuthal increments is unchanged.
- Rotor Configuration - Analysis of articulated, teetering, gimbaled or hingeless rotors.

The discussion which follows presents a review of available analytical methods for representing unsteady aerodynamics, selection of the most appropriate representation, development of the selected representation for incorporation in the C-81 (AGAJ71 version) program, and development of a method for representing radial flow effects.

The unsteady aerodynamics methodology is correlated with two-dimensional oscillating airfoil data in Appendix I. Appendix II contains correlations of the revised C-81 (AGAJ71) analysis with test data for isolated rotors and complete rotorcraft configurations.

SURVEY OF UNSTEADY AERODYNAMICS METHODS

The initial effort under the contract consisted of a comprehensive review and evaluation of available methods for the prediction of aerodynamic force and moment coefficients of oscillating airfoils. The methods were evaluated according to these criteria. First was correlation with available test data from airfoils of varying camber and thickness ratio (specifically NACA 0006, NACA 0012, Vertol 23010-1.58, and Vertol 13006-.7). Second was correlation with two-dimensional oscillating data (on the airfoils just named) for the following conditions:

- Below static stall to above dynamic stall.
- With and without yawed airload data.
- With and without the spanwise flow effects.

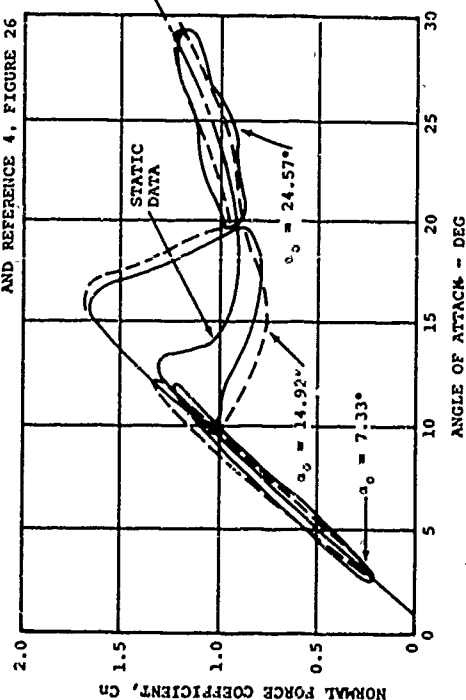
The third criterion was compatibility with the Government's Rotorcraft Flight Simulation Computer Program. Three approaches offered potentially acceptable solutions. They were the methods of Ericsson and Reding¹, Carta et al², and Harris et al³. The following paragraphs summarize the significant points of the analyses and data correlations presented in the three referenced methods. The references do not address each of the above selection criteria in all cases; however, based on the available information, a judgement was made concerning the merits and deficiencies of each method.

Ericsson and Reding¹ describe a quasi-steady theory in which time history effects are lumped into one discrete past-time event, and accelerated flow effects (due to pitch rate) are represented by an equivalent time lag. The method yielded acceptable correlation results. However, the approach uses a semiempirical graphical technique and is not amenable to computer methods. In a more recent report, Ericsson and Reding⁴ documented results of a functional representation of their method. However, the functional approach is obtained at the expense of accuracy. Figure 1 presents the correlation results from Ericsson and Reding⁴ and shows that the graphic technique produces good correlation with the test results, but that the functional technique degrades accuracy. The figure also shows that the graphic technique correlates reasonably well with NACA 0012 pitching moment data.

Carta et al² offered a technique of generalizing available sinusoidal pitch oscillation data for an NACA 0012 section. Carta hypothesized that the airfoil force

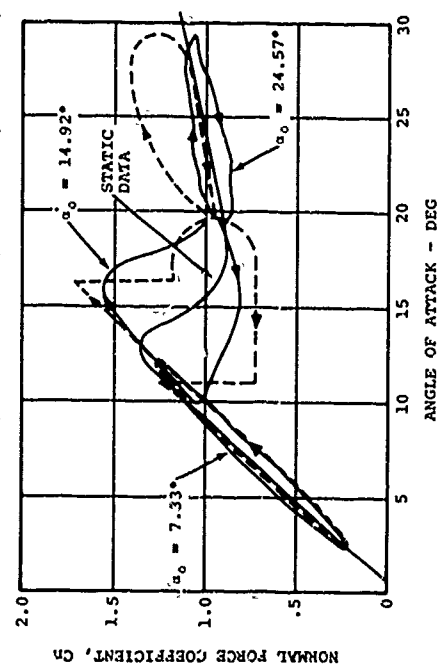
REFERENCE 3, FIGURES 48 AND 49
AND REFERENCE 4, FIGURE 26

GRAPHIC TECHNIQUE

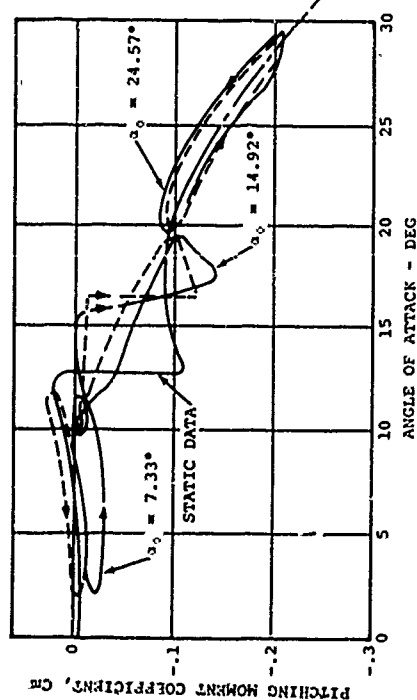


(REFERENCE 4, FIGURE 40)

FUNCTIONAL TECHNIQUE



5



LEGEND

V23010-1.58 AIRFOIL

— EXPERIMENTAL RESULTS

- - - ANALYTICAL ESTIMATES

MACH NO. = 0.4

RED. FREQ = 0.124

$\Delta\alpha = 4.85^\circ$

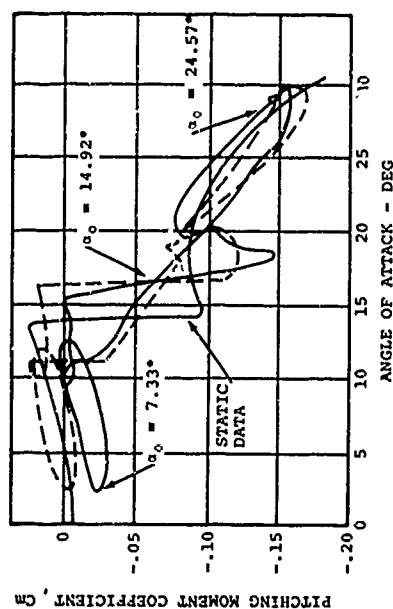


Figure 1. Theory of Ericsson and Reding (Sheet 1 of 2).

LEGEND

NACA 0012 AIRFOIL

— EXPERIMENTAL RESULTS

- - - ANALYTICAL ESTIMATES

$M = 0.2$

RED. FREQ = 0.224

$\Delta\alpha = 6^\circ$

GRAPHIC TECHNIQUE

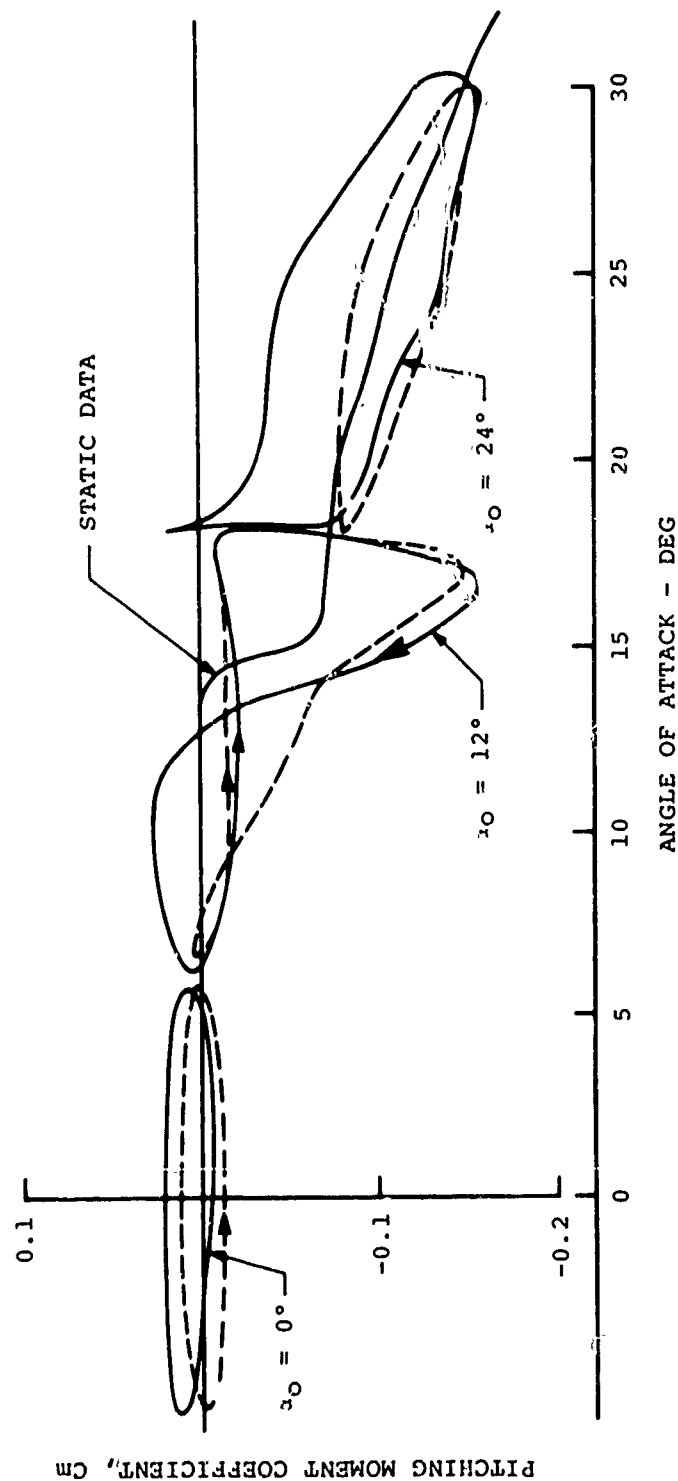


Figure 1. Continued (Sheet 2 of 2).

coefficients could be generalized as functions of instantaneous angle of attack, angular velocity, and angular acceleration. In an attempt to isolate the dynamic contribution to the force coefficients, he subtracted the static force coefficients from the measured two-dimensional dynamic test data. The resulting incremented data, due to dynamic effects, were assembled in the form of tabular cross-plots for use in computer analyses. Figure 2 depicts a comparison of Carta's reconstituted dynamic loops with the measured test loops. Although this method provided an improved representation of blade element force coefficients, there are serious drawbacks which make it unsuitable for other airfoils. The table generated by Carta is peculiar to the NACA 0012 airfoil section and also requires excessive computer storage space which is undesirable in large computer simulations like the C-81 analysis. Oscillating airfoil tests for four different sections (Liiva and Gray^{6,7}) show that the incremental force coefficients between static and dynamic tests are dependent on the airfoil section tested. (Figures 11 and 13 of this report illustrate the variation in stall delay of four different airfoils.) Thus, to utilize the Carta technique requires the generation of a table for the particular airfoil of interest which is both undesirable and impractical.

The approach utilized by Harris et al³, although semiempirical, gives good correlation with section tests data and is amenable to computer methods. Figure 3 illustrates Harris' correlation with the V23010-1.58 airfoil, two-dimensional oscillating data. The semiempirical method is an extension of theory developed by Theodorsen⁵ and relies primarily on utilizing static 2-D section force characteristics and a stall hysteresis formulation based on observed oscillating airfoil test data. Harris developed functional equations for this method and avoids the computer storage requirement inherent in Carta's method. Harris' method is also sufficiently general to allow application to general airfoil types. An additional feature pointed out by Harris³ is that utilization of the method in an analog rotor analysis yielded greatly improved correlation with existing model rotor and full-scale rotor test data. Figure 4 shows the improved rotor correlations obtained by Harris. Of particular importance are the improved correlations at high rotor lift coefficients.

Based on the criteria for selection, the method of Harris³ was chosen as offering the best potential for yielding a successful representation of unsteady aerodynamics in the Government's Rotorcraft Flight Simulation Computer Program. In order to ensure that the Harris method satisfied all of the selection criteria, it

LEGEND

REFERENCE 2

NACA 0012 AIRFOIL

— EXPERIMENTAL RESULTS

--- RECONSTRUCTED LOOP

MACH NO. = 0.4

RED FREQ = 0.112

$\Delta\alpha = 0^\circ$

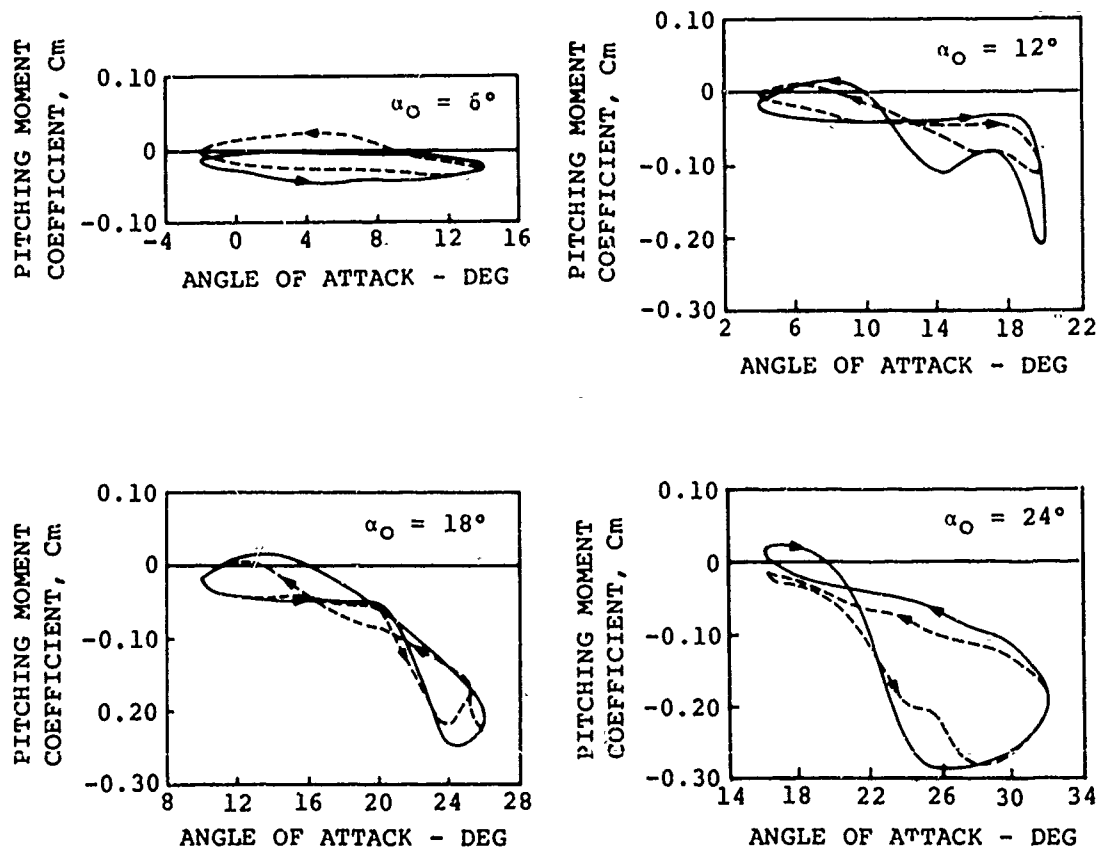


Figure 2. Comparison of Oscillating Airfoil Data and Carta Reconstructed Data.

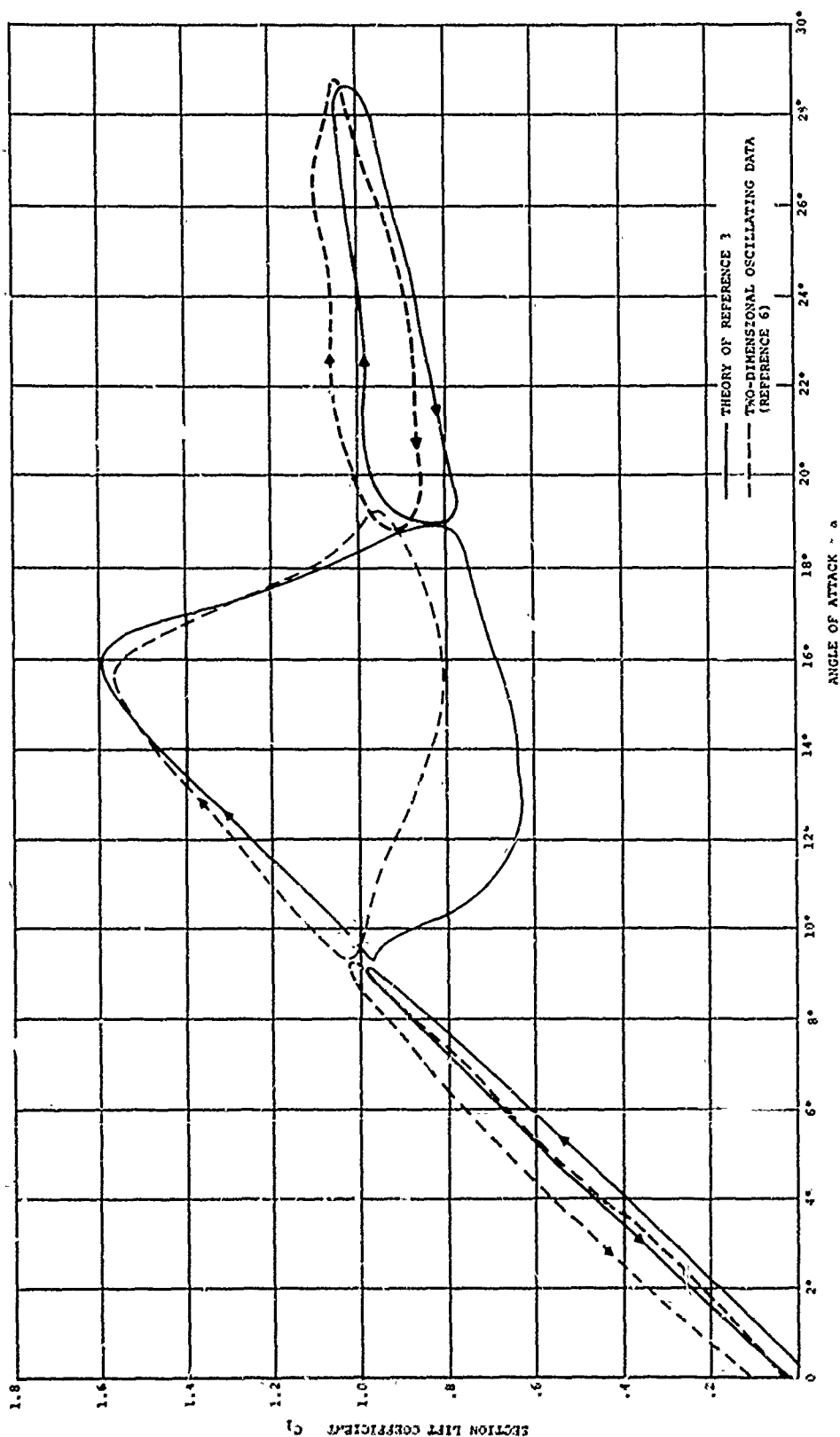


Figure 3. Engineering Approximation Accounting for Potential Flow Unsteady Aerodynamics Below Stall.

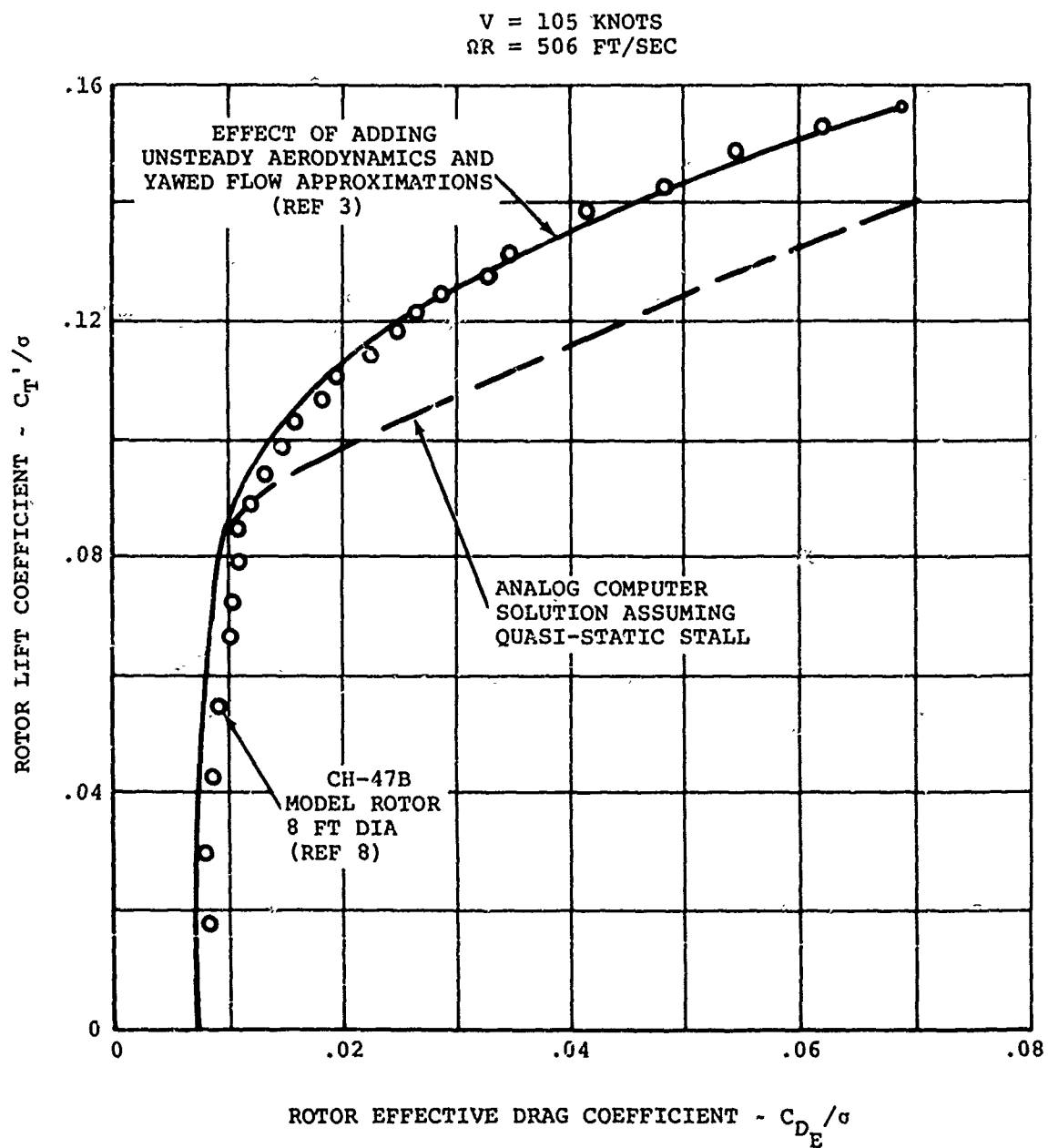


Figure 4. Improved Prediction of Rotor Performance
 (Sheet 1 of 2).

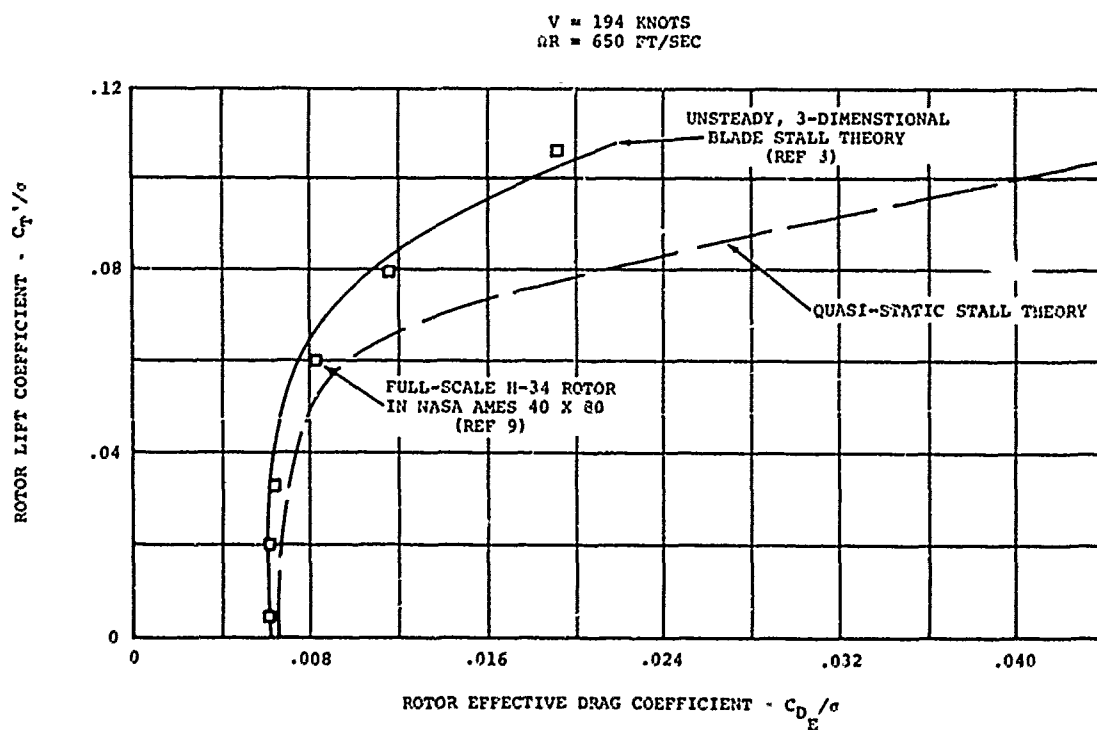
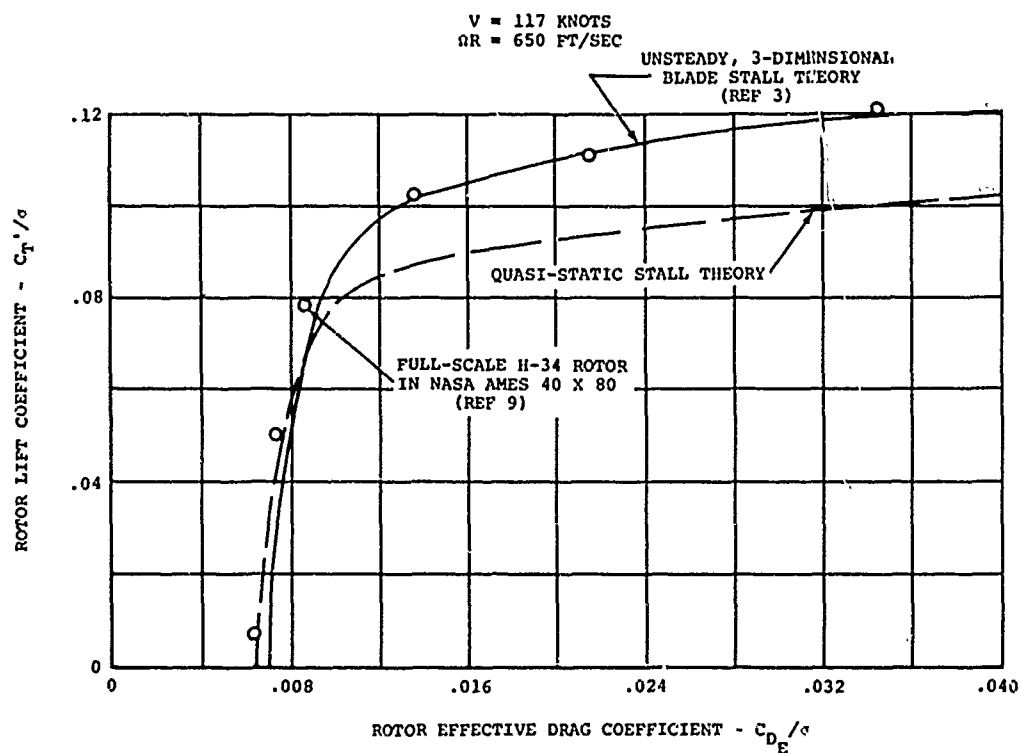


Figure 4. Continued (Sheet 2 of 2).

was correlated with two-dimensional oscillating data for the four previously mentioned airfoils. Appendix I contains the results of the extensive correlation. Since no data is available for yawed oscillating section data, the effects of radial flow were assessed by correlating the C-81 analysis with measured rotor test data. C-81 was run with and without radial flow effects in order to determine the impact on correlation. These data are presented in Appendix II

DESCRIPTION AND DEVELOPMENT OF SELECTED UNSTEADY AERODYNAMICS METHOD

INCOMPRESSIBLE POTENTIAL FLOW SOLUTION OF OSCILLATING AIRFOILS

The flow environment encountered by a helicopter blade element changes rapidly as the blade traverses the azimuth. At azimuthal positions (ψ) of 0 and 180 degrees, the velocity components are caused by the angular rotation of the rotorblade. At ψ of 90 and 270 degrees, the velocity is the sum of (90) and the difference between the (270) rotational and translational velocities. The variations around the azimuth can result in blade elements encountering velocities near-zero and near-sonic in one rotor revolution (which typically takes 1/4 second for full-scale rotors). At the same time the velocity variation is occurring, the blade elements are subjected to angle-of-attack variations from zero or negative values to values well beyond the stall angle. Most classical rotor analyses have ignored the time-variant aspect of rotorcraft aerodynamics and have assumed a quasi-static relationship which allowed the use of static airfoil force coefficients in evaluating local aerodynamic forces acting on a blade element. Harris³ and other observers noted that the utilization of static airfoil characteristics in conventional rotor analyses did not account for the demonstrated ability of rotors to produce lift values well beyond the maximum values predicted theoretically. Some phenomenon was enabling rotor blade elements to generate more lift than could be explained with two-dimensional static airfoil data. Harris's goal was to generate methodology which would accurately predict rotor performance throughout the normal operating range and well into the rotor stall regime. The following development is based on Harris's work and extends it to include second-order effects which were ignored in the original formulation due to the limited capability of the analog computer being used. Theodorsen's⁵ development of unsteady aerodynamic theory is the basis for the method developed herein. Theodorsen's linear, incompressible potential flow theory yields the following equations for a thin airfoil oscillating in pitch and heaving in translation about a mean pitch angle of zero degrees:

$$L = \rho b^2 \left(\overset{\textcircled{1}}{V\pi \dot{\theta}} + \overset{\textcircled{2}}{\pi \ddot{h}} - \overset{\textcircled{3}}{\pi b a \ddot{\theta}} \right) + \underbrace{2 \pi \rho V b C \left(V\theta + \dot{h} + b \left(\frac{1}{2} - a \right) \dot{\theta} \right)}_{\textcircled{4}} \quad (1)$$

$$M_{PA} = -\rho b^2 \left(\overset{\textcircled{1}}{\pi \left(\frac{1}{2} - a \right) V b \dot{\theta}} + \overset{\textcircled{3}}{\pi b^2 \left(\frac{1}{8} + a^2 \right) \ddot{\theta}} - \overset{\textcircled{2}}{a \pi b \ddot{h}} \right) + 2 \pi \rho V b^2 \overset{\textcircled{4}}{\pi \left(a + \frac{1}{2} \right) C \left(V\theta + \dot{h} + b \left(\frac{1}{2} - a \right) \dot{\theta} \right)} \quad (2)$$

Figure 5 illustrates the terms and sign conventions. The following table explains the circled reference numerals.

REFERENCE KEY TO EQUATIONS 1 AND 2			
Reference Numerals	Term in Lift Equation	Moment Arm for Pitching Moment	Source
(1)	$\pi \rho b^2 V \dot{\theta}$	$b (1/2 - a)$	Noncirculatory, acting at 3/4 chord
(2)	$\pi \rho b^2 \ddot{h}$	ab	Noncirculatory, acting at 1/2 chord
(3)	$\pi \rho b^3 a \ddot{\theta}$	ab	
The pitching moment also includes a $\pi \rho b^4 \ddot{\theta} / 8$ term which reflects the inertial effects for a cylinder of air circumscribing the airfoil.			
(4)	$2 \pi \rho V b C$ $(V \theta + \dot{h} + b (1/2 - a) \dot{\theta})$	$(a + 1/2b)$	Circulatory, acting at 1/4 chord

Theodorsen's equations were obtained by integrating pressure distributions over a thin airfoil (flat plate) subjected to arbitrary pitch and heaving motion. The pressure distributions were obtained by specifying a system of velocity potentials (sources, sinks and rectilinear flows) over the airfoil section. Equations (1) and (2) are the resulting integrated force equations for section lift and section pitching moment about the quarter chord. The terms in these equations are of two types: circulatory -- those which produce a trailed or shed wake (terms multiplied by

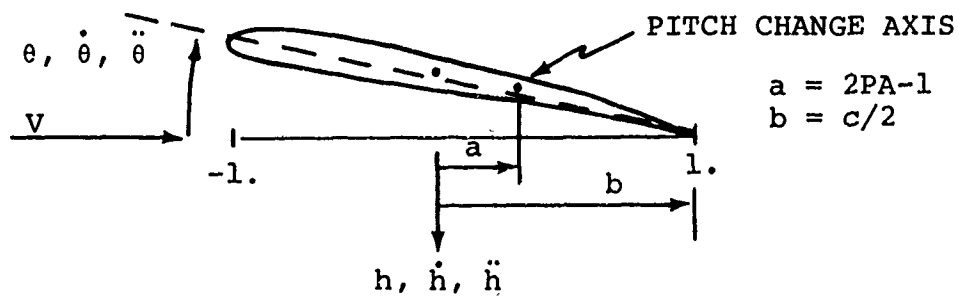


Figure 5. Theodorsen's Sign Conventions.

Theodorsen's C function)--and noncirculatory--those which are due to oscillating pitch or heaving motion and do not produce shed wake. By comparing the lift and moment equations term by term, an analogy can be drawn for the effective location of lumped components of the integrated lift forces. Referenced to the circled numerals in Equations (1) and (2), the source and analogous location of the lumped lift components are given in the preceding table.

For further understanding of Equations (1) and (2), the reader is referred to Bisplinghof et al ¹⁰, who devote considerable material to this subject.

Rearranging terms and introducing chord c and dimensionless pitch axis location PA , the following form is obtained:

$$L = (2\pi) \frac{\rho}{2} V^2 \frac{c^2}{4} \left(\frac{\dot{\theta}}{V} + \frac{\ddot{h}}{V^2} - c (PA - 1/2) \frac{\ddot{\theta}}{V^2} \right) + (2\pi) \frac{\rho}{2} V^2 c C \left(\theta + \frac{\dot{h}}{V} + c (3/4 - PA) \frac{\dot{\theta}}{V} \right) \quad (3)$$

$$M_{PA} = - (2\pi) \frac{\rho}{2} V^2 \frac{c^2}{4} \left((3/4 - PA) \frac{c \dot{\theta}}{V} + c^2 (1/32 + (PA - 1/2)^2) \frac{\ddot{\theta}}{V^2} - (PA - 1/2) \frac{c \ddot{h}}{V^2} \right) + (2\pi) \frac{\rho}{2} V^2 c^2 (PA - 1/4) C \left(\theta + \frac{\dot{h}}{V} + c (3/4 - PA) \frac{\dot{\theta}}{V} \right) \quad (4)$$

In the above equations, Theodorsen's $C_{(k)}$ term is a complex quantity and a function of reduced frequency k

$$C = F + i G \quad (5)$$

$$\text{where } k = \frac{c \omega}{2V} \quad (6)$$

and ω is the oscillation frequency.

Figure 6 presents values for F and G which were determined by Theodorsen. Physically, the F term represents a lift deficiency term due to oscillation and iG represents a phase lag between the airfoil oscillatory motion and the resulting aerodynamic forces.

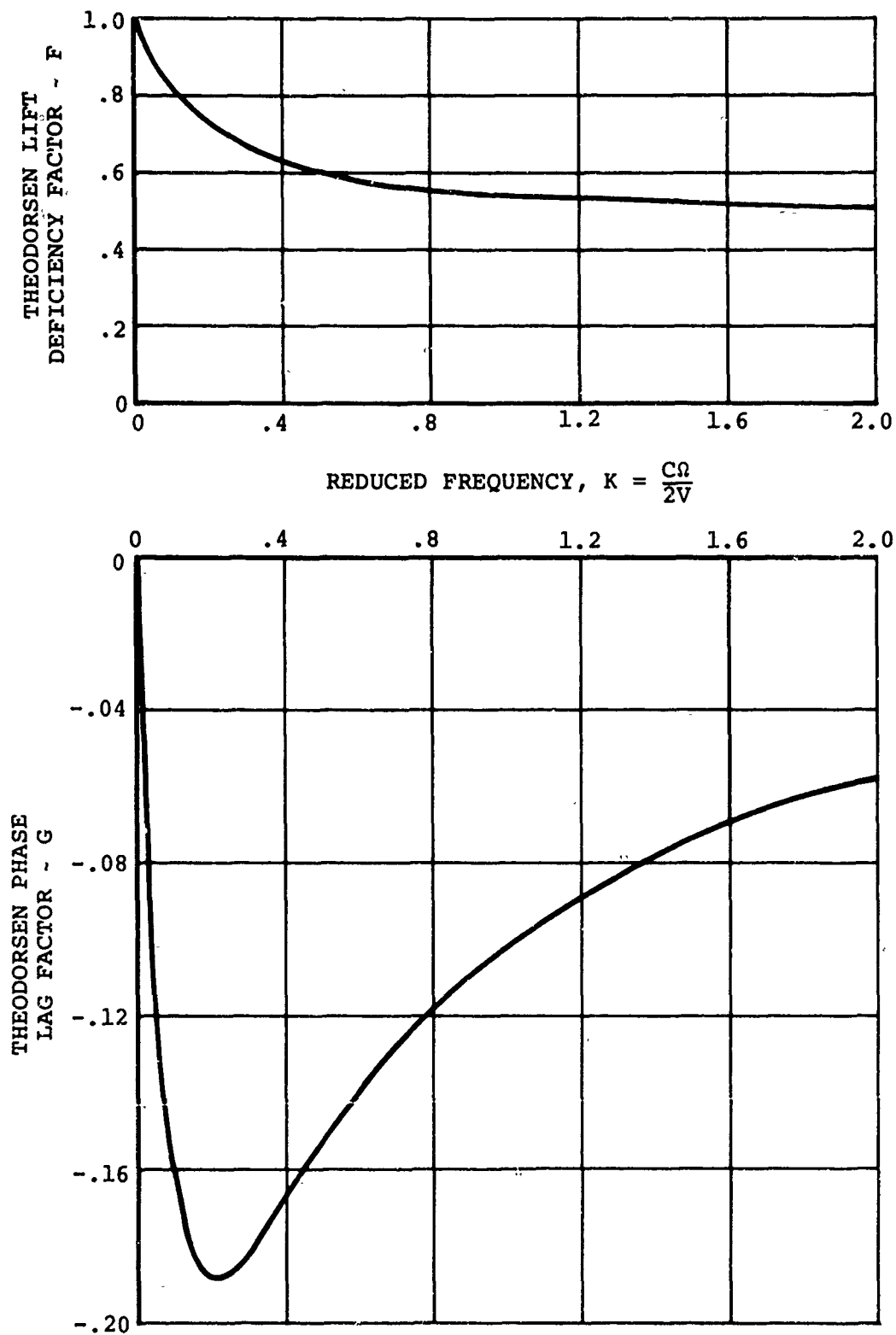


Figure 6. Theodorsen Unsteady Aerodynamic Functions.

For the trivial case of no pitch oscillation and a steady vertical translation velocity (corresponding to inflow and flapping velocity for a rotor), $F = 1$ and $G = 0$ and Equations (3) and (4) reduce to

$$L = (2\pi) \frac{\rho}{2} V^2 c \left(\theta + \frac{\dot{h}}{V} \right) \quad (7)$$

$$M_{PA} = (2\pi) \frac{\rho}{2} V^2 c^2 (PA - 1/4) \left(\theta + \frac{\dot{h}}{V} \right) \quad (8)$$

The $(\theta + \dot{h}/V)$ quantity is the quasi-steady angle of attack. Equations (7) and (8) are the classical potential flow solution for lift and moment on a thin airfoil section.

When the terms of Equations (3) and (4) are expanded, the C term introduces imaginary quantities. However, the following formulation is useful in performing the expansion. Since Theodorsen's equations are for deviations from a zero mean angle of attack and are, therefore, vibratory in nature,

let

$$\left. \begin{aligned} \theta_v &= \theta_\omega \sin \omega t \\ h_v &= h_\omega \sin \omega t \end{aligned} \right\} \quad (9)$$

and

$$\left. \begin{aligned} \dot{\theta}_v &= \omega \theta_\omega \cos \omega t = i \omega \theta_v \\ \ddot{\theta}_v &= -\omega^2 \theta_\omega \sin \omega t = -\omega^2 \theta_v \\ \dot{h}_v &= \omega h_\omega \cos \omega t = i \omega h_v \\ \ddot{h}_v &= -\omega^2 h_\omega \sin \omega t = -\omega^2 h_v \end{aligned} \right\} \quad (10)$$

Substituting,

$$L = (2\pi) \frac{\rho}{2} V^2 \frac{c^2}{4} \left(\frac{\dot{\theta}_v}{V} + \frac{\ddot{h}_v}{V^2} - c (PA - 1/2) \frac{\ddot{\theta}_v}{V^2} \right) + (2\pi) \frac{\rho}{2} V^2 c (F + iG) \left(\theta_v + \frac{i \omega h_v}{V} + c (3/4 - PA) \frac{i \omega \theta_v}{V} \right) \quad (11)$$

$$M_{PA} = -(2\pi) \frac{\rho}{2} V^2 \frac{c^2}{4} \left((3/4 - PA) \frac{c \dot{\theta}_v}{V} + c^2 (1/32 + (PA - 1/2)^2) \frac{\ddot{\theta}_v}{V^2} \right. \\ \left. - (PA - 1/2) \frac{c \ddot{h}_v}{V^2} \right) \quad (12)$$

$$+ (2\pi) \frac{\rho}{2} V^2 c^2 (PA - 1/4) (F + iG) \left(\theta_v + \frac{i\omega h_v}{V} + c(3/4 - PA) \frac{i\omega \theta_v}{V} \right)$$

Expanding yields

$$L = (2\pi) \frac{\rho}{2} V^2 \frac{c^2}{4} \left(\frac{\dot{\theta}_v}{V} + \frac{\ddot{h}_v}{V^2} - c(PA - 1/2) \frac{\ddot{\theta}_v}{V^2} \right) \\ + (2\pi) \frac{\rho}{2} V^2 c^2 \left(F \theta_v + \frac{Fi\omega h_v}{V} + Fc(3/4 - PA) \frac{i\omega \theta_v}{V} + iG \theta_v \right. \\ \left. - \frac{G\omega h_v}{V} - Gc(3/4 - PA) \frac{\omega \theta_v}{V} \right) \quad (13)$$

$$M_{PA} = -(2\pi) \frac{\rho}{2} V^2 \frac{c^2}{4} \left((3/4 - PA) \frac{c \dot{\theta}_v}{V} + c^2 (1/32 + (PA - 1/2)^2) \frac{\ddot{\theta}_v}{V^2} \right. \\ \left. - (PA - 1/2) \frac{c \ddot{h}_v}{V^2} \right) \quad (14)$$

$$+ (2\pi) \frac{\rho}{2} V^2 c^2 (PA - 1/4) \left(F \theta_v + \frac{Fi\omega h_v}{V} + Fc(3/4 - PA) \frac{i\omega \theta_v}{V} \right. \\ \left. + iG \theta_v - \frac{G\omega h_v}{V} - Gc(3/4 - PA) \frac{\omega \theta_v}{V} \right)$$

Referring to Equation (10), and noting that

$$\left. \begin{aligned} i \theta_v &= \frac{\dot{\theta}_v}{\omega} \\ i h_v &= \frac{\dot{h}_v}{\omega} \\ \omega h_v &= \frac{-\ddot{h}_v}{\omega} \end{aligned} \right\} \quad (15)$$

Combining Equations (15) with (13) and (14) yields

$$\begin{aligned} L = & (2\pi) \frac{\rho}{2} V^2 \frac{c^2}{4} \left(\frac{\dot{\theta}_v}{V} + \frac{\ddot{h}_v}{V^2} - c (PA-1/2) \frac{\ddot{\theta}_v}{V^2} \right) + \\ & (2\pi) \frac{\rho}{2} V^2 c \left(F \left(\theta_v + \frac{\dot{h}_v}{V} + c (3/4-PA) \frac{\dot{\theta}_v}{V} \right) + \right. \\ & \left. G \left(\frac{\dot{\theta}_v}{\omega} + \frac{\ddot{h}_v}{\omega V} - c (3/4-PA) \frac{\omega \theta_v}{V} \right) \right) \end{aligned} \quad (16)$$

$$\begin{aligned} M_{PA} = & (2\pi) \frac{\rho}{2} V^2 \frac{c^2}{4} \left((PA-3/4) \frac{c \dot{\theta}_v}{V} - c^2 (1/32 + (PA-1/2)^2) \frac{\ddot{\theta}_v}{V^2} + \right. \\ & \left. (PA-1/2) \frac{c \ddot{h}_v}{V^2} \right) + (2\pi) \frac{\rho}{2} V^2 c^2 (PA-1/4) \\ & \left(F \left(\theta_v + \frac{\dot{h}_v}{V} + c (3/4-PA) \frac{\dot{\theta}_v}{V} \right) + \right. \\ & \left. G \left(\frac{\dot{\theta}_v}{\omega} + \frac{\ddot{h}_v}{\omega V} - c (3/4-PA) \frac{\omega \theta_v}{V} \right) \right) \end{aligned} \quad (17)$$

To this point, the development has considered oscillation about a mean angle of zero. Extending the theory to include oscillation about a nonzero mean, θ_0 , and rearranging terms gives

$$L = (2\pi) \frac{\rho}{2} V^2 \frac{c^2}{4} \left(\frac{\dot{\theta}_v}{V} + \frac{\ddot{h}_v}{V^2} - c (PA - 1/2) \frac{\ddot{\theta}_v}{V^2} \right) +$$

$$(2\pi) \frac{\rho}{2} V^2 c \left(\theta_0 + \left(F - c (3/4 - PA) \frac{G}{\omega} \right) \theta_v + \frac{F \dot{h}_v}{V} + \right. \quad (18)$$

$$\left. \frac{G \ddot{h}_v}{\omega V} + \left(\frac{G}{\omega} + c (3/4 - PA) \frac{F}{V} \right) \dot{\theta}_v \right)$$

$$M_{PA} = (2\pi) \frac{\rho}{2} V^2 \frac{c^2}{4} \left((PA - 3/4) \frac{c \dot{\theta}_v}{V} - c^2 (1/32 + (PA - 1/2)^2) \frac{\ddot{\theta}_v}{V^2} + \right.$$

$$\left. (PA - 1/2) \frac{c \ddot{h}_v}{V^2} \right) + (2\pi) \frac{\rho}{2} V^2 c^2 (PA - 1/4)$$

$$\left(\theta_0 + \left(F - c (3/4 - PA) \frac{G}{\omega} \right) \theta_v + \frac{F \dot{h}_v}{V} + \right. \quad (19)$$

$$\left. \frac{G \ddot{h}_v}{\omega V} + \left(\frac{G}{\omega} + c (3/4 - PA) \frac{F}{V} \right) \dot{\theta}_v \right)$$

Theodorsen's F and G functions act only on oscillatory terms which produce a shed wake. Since θ_0 is a steady term, let $F = 1$ and $G = 0$ for the mean pitch term.

Equations (18) and (19) are the resultant formulation for the lift and moment on an airfoil section which is pitching and heaving about a mean pitch angle of θ_0 . The equations as shown are for incompressible two-dimensional flow. The next section will modify these expressions to the three-dimensional, compressible flow of a rotary wing.

MODIFICATION TO COMPRESSIBLE FLOW AND ROTATING ENVIRONMENT

Equations (18) and (19) discussed previously related section incompressible lift and pitching moment to airfoil pitch and heaving rates and accelerations. In addition, the equations contain an angular rate term ω which corresponds to the oscillation frequency. For the case of a rotating wing, the dominant frequency for pitch and blade motion is a 1/rev sinusoidal variation. Therefore, the angular frequency reference is equal to the rotor angular speed, Ω , and Theodorsen's F and G functions will be evaluated for the 1/rev frequency. Equations (18) and (19) take the form

$$L = (2\pi) \frac{\rho}{2} V^2 \frac{c^2}{4} \left(\frac{\dot{\theta}_v}{V} + \frac{\dot{h}_v}{V^2} - c (PA - 1/2) \frac{\ddot{\theta}_v}{V^2} \right) +$$

$$(2\pi) \frac{\rho}{2} V^2 c \left(\theta_o + (F - c (3/4 - PA) \frac{G\Omega}{V}) \theta_v + \frac{F\dot{h}_v}{V} + \right. \quad (20)$$

$$\left. \frac{G\ddot{h}_v}{\Omega V} + \left(\frac{G}{\Omega} + c (3/4 - PA) \frac{F}{V} \right) \dot{\theta}_v \right)$$

$$M_{PA} = (2\pi) \frac{\rho}{2} V^2 \frac{c}{4} \left((PA - 3/4) \frac{c\dot{\theta}_v}{V} - c^2 (1/32 + (PA - 1/2)^2) \frac{\ddot{\theta}_v}{V^2} + \right.$$

$$(PA - 1/2) \frac{c\ddot{h}_v}{V^2} + (2\pi) \frac{\rho}{2} V^2 c^2 (PA - 1/4)$$

$$\left(\theta_o + (F - c (3/4 - PA) \frac{G\Omega}{V}) \theta_v + \frac{F\dot{h}_v}{V} + \right. \quad (21)$$

$$\left. \frac{G\ddot{h}_v}{\Omega V} + \left(\frac{G}{\Omega} + c (3/4 - PA) \frac{F}{V} \right) \dot{\theta}_v \right)$$

where

$$F = f \left(\frac{c\Omega}{2V} \right)$$

$$G = f \left(\frac{c\Omega}{2V} \right)$$

In the development of Equations (1) and (2), Theodorsen computed the potential flow effects of airfoil velocity distributions due to pitching ($\dot{\theta}$ and $\ddot{\theta}$) and heaving (\dot{h} and \ddot{h}). For the case of a rotating airfoil, additional terms are encountered.

Blade coning position produces a term which is derived in Figure 7. The top in Figure 7 shows the velocity vectors V_Ω at the leading and trailing edges of an airfoil which are caused by blade rotation about the shaft. Utilizing the small angles, ϵ_1 and ϵ_2 , and resolving the V_Ω vectors into components which are both perpendicular to the shaft and in the direction of the span, we obtain the vectors $V_\Omega \epsilon_1$ and $V_\Omega \epsilon_2$. Now when these vectors are transferred to the side view in Figure 7, they resolve into components parallel to the span and components perpendicular to the blade element ($V_\Omega \epsilon_1 \beta$ and $V_\Omega \epsilon_2 \beta$). These latter components give the airfoil a sense of pitch motion, as shown in the velocity distribution diagram in Figure 7. The apparent pitch rate is

$$\dot{\theta}_{APP} = \Omega \sin \beta \quad (22)$$

To illustrate this effect, examine the extreme case of a blade coned to 90° ($\sin \beta = 1$) and having an angular velocity Ω . The apparent pitch rate $\dot{\theta}_{APP}$ is equal to Ω . In the other extreme, the trivial case of $\beta = 0$ yields $\dot{\theta}_{APP} = 0$ since the resultant velocity due to rotation is parallel to the section chord line.

For small coning angles

$$\left. \begin{aligned} \dot{\theta}_{APP} &= \Omega \beta = \Omega (\beta_o + \beta_v) \\ \ddot{\theta}_{APP} &= \Omega \dot{\beta} = \Omega (\dot{\beta}_v) \end{aligned} \right\} \quad (23)$$

where β_o is the mean coning angle and β_v is the instantaneous deviation from the mean.

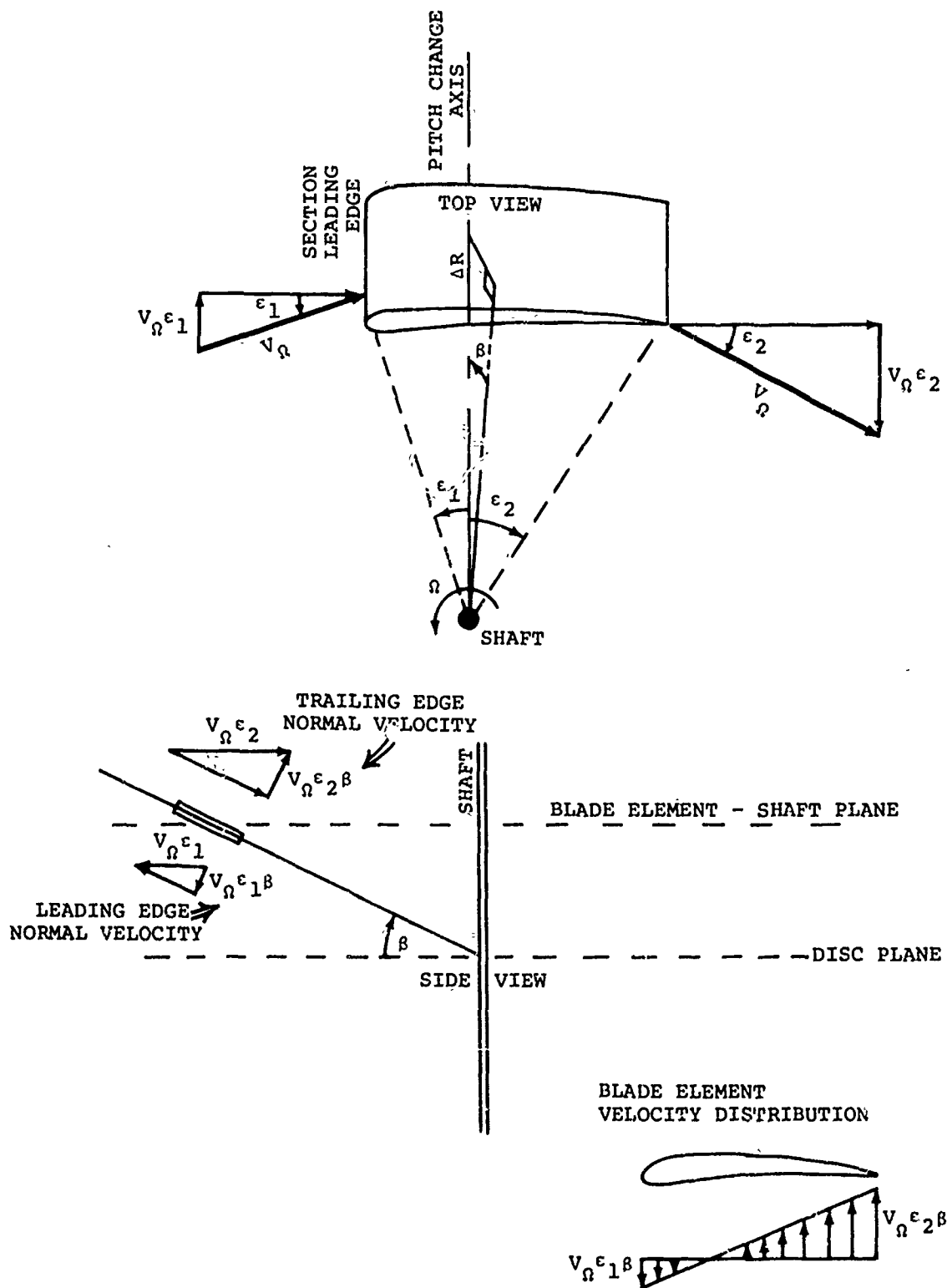


Figure 7. Effective Blade Element Pitch Rate Due to Blade Coning.

Another term peculiar to the rotary-wing problem is caused by steady terms in the normal velocity component, \dot{h} . The velocity component normal to the blade section (Figure 8) is given by

$$\dot{h} = V_{FLT} \sin \alpha_s \cos \beta - V_{FLT} \sin \beta \cos \alpha_s \cos \Psi - (\dot{v}_z + \dot{Z}) \cos \beta \quad (24)$$

For small flapping angles

$$\dot{h} = V_{FLT} \sin \alpha_s - V_{FLT} \beta \cos \alpha_s \cos \Psi - \dot{v}_z - \dot{Z} \quad (25)$$

For steady rectilinear flight, the \dot{h} term is made up of steady plus vibratory components and can be written

$$\left. \begin{aligned} \dot{h} &= \dot{h}_o + \dot{h}_v \\ \ddot{h} &= \ddot{h}_v \\ \dot{h}_o &= V_{FLT} \sin \alpha_s - v_{z(c)} - \dot{Z} \\ \dot{h}_v &= -V_{FLT} \beta \cos \alpha_s \cos \Psi - v_{z(v)} \end{aligned} \right\} \quad (26)$$

where $v_{z(o)}$ is the mean value of induced velocity and $v_{z(v)}$ is the instantaneous deviation from the mean.

Again, since the β_o and \dot{h}_o terms from Equations (23) and (26) are steady terms, Theodorsen's $F = 1$ and $G = 0$ for them. Combining (23) and (26) with (20) and (21) gives the final form for the rotating environment.

$$\begin{aligned} L = (2\pi) \frac{\rho}{2} V^2 \frac{c^2}{4} & \left(\frac{1}{V} (\dot{\theta}_v + \Omega \beta) + \frac{\ddot{h}_v}{V^2} - (PA - 1/2) (\ddot{\theta}_v + \Omega \dot{\beta}_v) \frac{c}{V^2} \right) + \\ & (2\pi) \frac{\rho}{2} V^2 c \left(\theta_o + \left(F - c(3/4 - PA) \frac{G\Omega}{V} \right) \theta_v + \frac{F \dot{h}_v}{V} + \frac{\dot{h}_o}{V} + \frac{G \ddot{h}_v}{\Omega V} + \right. \\ & \left. c(3/4 - PA) \frac{\Omega \beta_o}{V} + \left(c(3/4 - PA) \frac{F}{V} + \frac{G}{\Omega} \right) (\dot{\theta}_v + \Omega \beta_v) \right) \quad (27) \end{aligned}$$

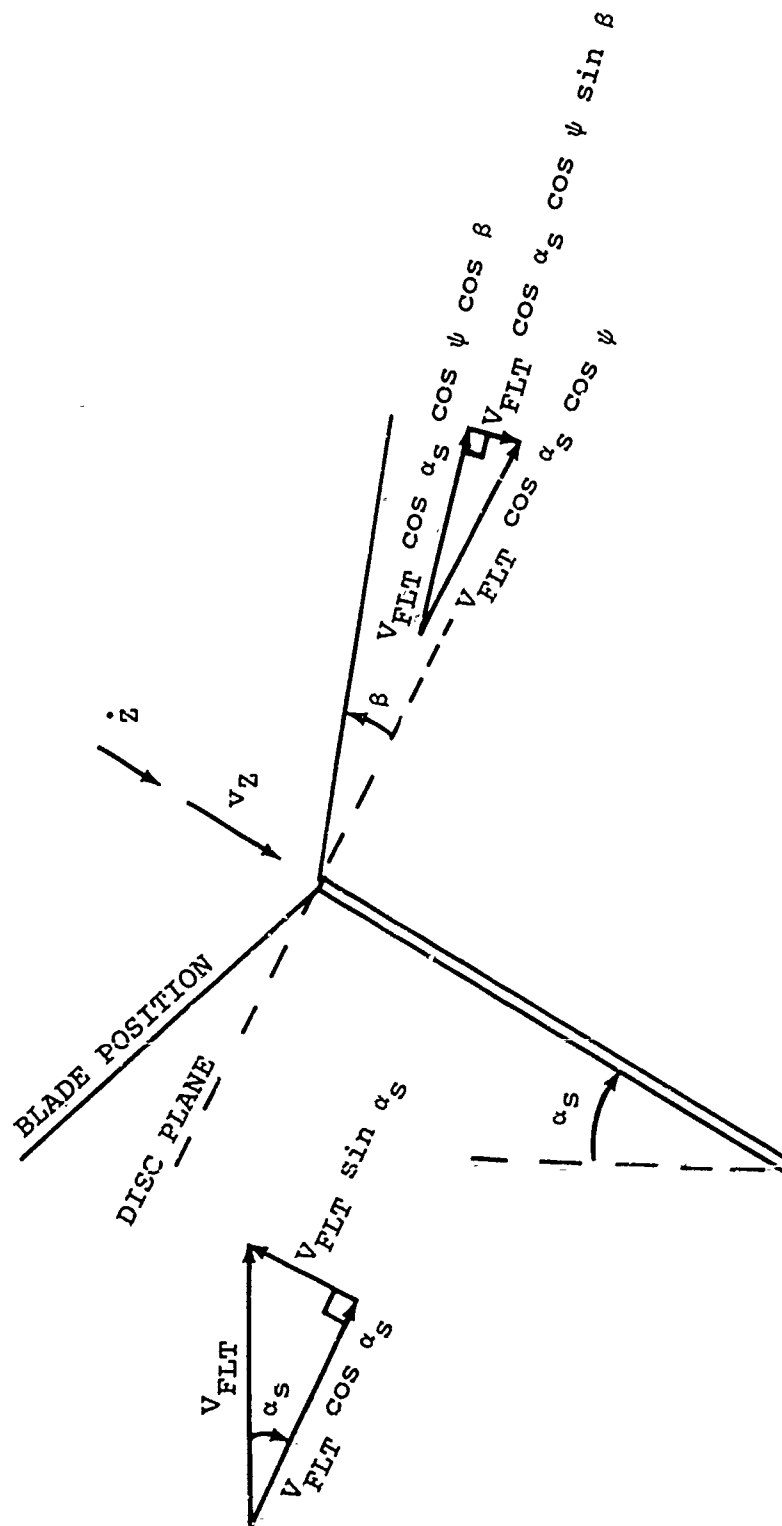


Figure 8. Velocity Components at Rotor.

$$\begin{aligned}
M_{PA} = (2\pi) \frac{\rho}{2} V^2 \frac{c^2}{4} & \left((PA-3/4) (\dot{\theta}_v + \Omega\beta) \frac{c}{V} - (1/32 + (PA-1/2)^2) \right. \\
& \left. (\ddot{\theta}_v + \Omega\dot{\beta}_v) \frac{c^2}{V^2} + (PA-1/2) \frac{c\ddot{h}_v}{V^2} \right) \\
& + (2\pi) \frac{\rho}{2} V^2 c^2 (PA-1/4) \left(\theta_0 + \left(F - c(3/4-PA) \frac{G\Omega}{V} \right) \theta_v + \right. \\
& \left. \frac{F\dot{h}_v}{V} + \frac{\dot{h}_0}{V} + \frac{G\ddot{h}_v}{\Omega V} + c(3/4-PA) \frac{\Omega\beta_0}{V} + \right. \\
& \left. \left(c(3/4-PA) \frac{F}{V} + \frac{G}{\Omega} \right) (\dot{\theta}_v + \Omega\beta_v) \right) \quad (28)
\end{aligned}$$

Rearranging the first group of terms in Equation (28) for future use,

$$\begin{aligned}
M_{PA} = (2\pi) \frac{\rho}{2} V^2 \frac{c^3}{4} (PA-3/4) & \left((\dot{\theta}_v + \Omega\beta_v) \frac{1}{V} + \frac{\ddot{h}_v}{V^2} - (PA-1/2) \right. \\
& \left. (\ddot{\theta}_v + \Omega\dot{\beta}_v) \frac{c}{V^2} \right) \\
& + 2\pi \frac{\rho}{2} V^2 \frac{c^3}{4} \left(\frac{\ddot{h}_v}{4V^2} - (PA-3/8) (\ddot{\theta}_v + \Omega\dot{\beta}_v) \frac{c}{4V^2} \right) \quad (29) \\
& + (2\pi) \frac{\rho}{2} V^2 c^2 (PA-1/4) \left(\theta_0 + \left(F - c(3/4-PA) \frac{G\Omega}{V} \right) \theta_v + \frac{F\dot{h}_v}{V} + \right. \\
& \left. \frac{\dot{h}_0}{V} + \frac{G\ddot{h}_v}{\Omega V} + c(3/4-PA) \frac{\Omega\beta_0}{V} + \right. \\
& \left. \left(c(3/4-PA) \frac{F}{V} + \frac{G}{\Omega} \right) (\dot{\theta}_v + \Omega\beta_v) \right)
\end{aligned}$$

Equations (27) and (29) apply to the case of linear incompressible aerodynamics. In order to modify the expressions to nonlinear compressible flow, the following adjustments are required.

First an equivalent angle of attack may be defined by

$$\begin{aligned} \alpha_{\text{EQU}} = & \theta_o + (F - c(3/4 - PA) \frac{G\Omega}{V}) \theta_v \\ & + \left(F \dot{h}_v + \dot{h}_o + \frac{G\ddot{h}_v}{\Omega} + c(3/4 - PA)\Omega \beta_o + (c(3/4 - PA)F + \right. \\ & \left. \frac{GV}{\Omega}) (\dot{\theta}_v + \Omega \beta_v) \right) / V \end{aligned} \quad (30)$$

Here it is necessary to make a distinction between the flow environment assumed by Theodorsen and the possible flow conditions experienced by a rotorcraft blade element. See Figure 9.

Theodorsen's assumption was that the airfoil experienced small deviations from the steady-state flow condition; i.e., $\dot{h} \ll V$. However, in the possible rotor environment, \dot{h} may be large compared to the total resultant velocity. This is true of the inboard blade segments and those near the reverse flow area. In addition, small-angle assumptions inherent in Theodorsen's equations may be removed by introducing the arc tangent function with respect to the velocity component U_T , resulting in

$$\begin{aligned} \alpha_{\text{EQU}} = & \theta_o + (F - c(3/4 - PA) \frac{G\Omega}{V}) \theta_v \\ & + \tan^{-1} \left\{ \left(F \dot{h}_v + \dot{h}_o + \frac{G\ddot{h}_v}{\Omega} + c(3/4 - PA)\Omega \beta_o + \right. \right. \\ & \left. \left. (c(3/4 - PA)F + \frac{GV}{\Omega}) (\dot{\theta}_v + \Omega \beta_v) \right) / U_T \right\} \end{aligned} \quad (31)$$

For the linear case, 2π represents the lift curve slope and the product $2\pi \alpha_{\text{EQU}}$ is an equivalent C_l . To introduce compressible nonlinear effects merely requires

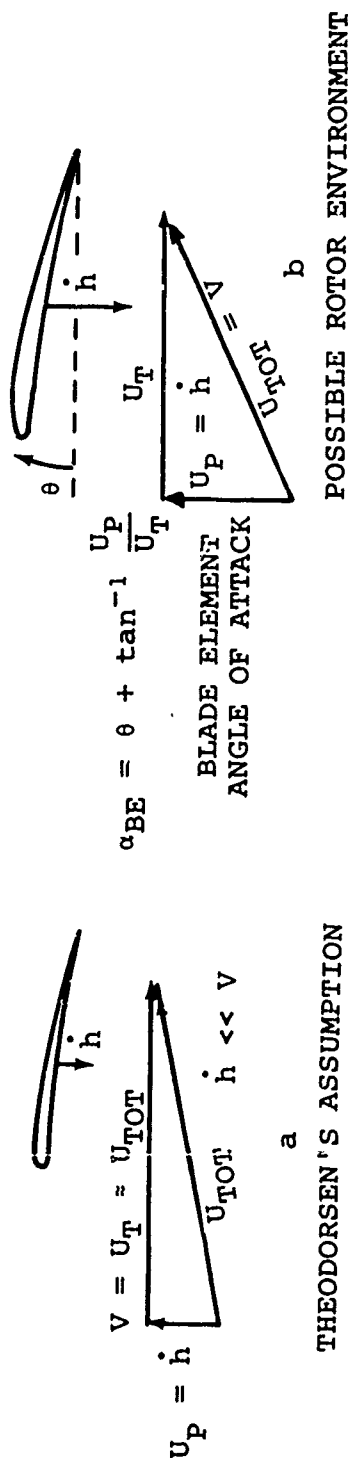


Figure 9. Blade Element Angle of Attack Assumptions.

entering equations or table look-up data for the airfoil section of interest and determining C_l , C_d and C_m as a function of α_{EQU} and Mach number.

The resulting force equations are:

$$\left. \begin{aligned}
 L &= \frac{1}{2} \rho V^2 c C_l + (2\pi) \frac{\rho}{2} V^2 \frac{c^2}{4} \left(\frac{1}{V} (\dot{\theta}_v + \Omega \beta) + \frac{\ddot{h}_v}{V^2} - (PA-1/2) \right. \\
 &\quad \left. (\ddot{\theta}_v + \Omega \dot{\beta}_v) \frac{c}{V^2} \right) \\
 D &= \frac{1}{2} \rho V^2 c C_d \\
 M_{PA} &= \frac{1}{2} \rho V^2 c^2 C_m + \frac{1}{2} \rho V^2 c^2 (PA-1/4) C_l \\
 &\quad + (2\pi) \frac{\rho}{2} V^2 \frac{c^3}{4} (PA-3/4) \left((\dot{\theta}_v + \Omega \beta) \frac{1}{V} + \frac{\ddot{h}_v}{V^2} - (PA-1/2) \right. \\
 &\quad \left. (\ddot{\theta}_v + \Omega \dot{\beta}_v) \frac{c}{V^2} \right) \\
 &\quad + (2\pi) \frac{\rho}{2} V^2 \frac{c^3}{16} \left(\frac{\ddot{h}_v}{V^2} - (PA-3/8) (\ddot{\theta}_v + \Omega \dot{\beta}_v) \frac{c}{V^2} \right)
 \end{aligned} \right\} (32)$$

The first term in the moment equation represents the basic test-measured pitching moment about quarter chord for the static airfoil section. This component is calculated to be zero when utilizing potential flow theory, but is finite for tests on airfoils. The second term, calculated by potential theory, represents the contribution to pitching moment due only to pitch-change-axis offset from the quarter chord (where the circulatory C_l acts). The third term reflects potential theory C_l contributions acting at 3/4 and 1/2 chord; the last term reflects the inertial forces of an air cylinder having a diameter equal to the chord.

Another limitation must be exercised in the event of large angles of attack. For this case, only airload components normal to the blade chord should be added to

the pitching moment. For large angles, a $\sin \alpha_{BE}$ component due to drag is introduced, and the C_l contribution is limited by $\cos \alpha_{BE}$ resulting in the formulation of Equation (34).

Further simplification of these equations is accomplished by letting

$$\bar{C}_l = (2\pi) \frac{c}{4} \left(\frac{1}{V} (\dot{\theta}_v + \Omega \beta) + \frac{\ddot{h}_v}{V^2} - (PA - 1/2) (\ddot{\theta}_v + \Omega \dot{\beta}_v) \frac{c}{V^2} \right) \quad (33)$$

$$\left. \begin{aligned} L &= \frac{1}{2} \rho V^2 c (C_l + \bar{C}_l) \\ D &= \frac{1}{2} \rho V^2 c C_d \\ M_{PA} &= \frac{1}{2} \rho V^2 c^2 C_m + \frac{1}{2} \rho V^2 c^2 C_d (PA - 1/4) \sin \alpha_{BE} \\ &\quad + \frac{1}{2} \rho V^2 c^2 \left((PA - 1/4) C_l + (PA - 3/4) \bar{C}_l \right) \cos \alpha_{BE} \\ &\quad + \frac{\pi \rho c^3}{16} \left(\ddot{h}_v - (PA - 3/8) (\ddot{\theta}_v + \Omega \dot{\beta}_v) c \right) \end{aligned} \right\} \quad (34)$$

Equation (34) represents the rotor environment formulation for two-dimensional flow. The final requirement in the representation of the rotating environment is to account for three-dimensional (radial) flow. This is described in detail later under RADIAL FLOW REPRESENTATION. However, suffice to say here that the yawed flow produces two effects. The first is an increase in $C_{l_{max}}$ for angles of attack beyond stall:

$$C_{l_{max \Lambda}} = \frac{C_{l_{max \Lambda=0}}}{\cos \Lambda} \quad (35)$$

with the limitation that $C_{l_{\max \Lambda}}$ does not exceed the linear lift curve slope; i.e.,

$$C_{l_{\max \Lambda}} \leq \left(\frac{d C_l}{d \alpha} \right)_{\text{linear}} \alpha \quad (36)$$

The second effect of yawed flow is

$$C_{d \Lambda} = C_{d \Lambda=0} + C_{d_{SF}} (\sec \Lambda - 1) \quad (37)$$

Incorporating these into Equation (34) yields

$$\left. \begin{aligned} L &= \frac{1}{2} \rho V^2 c (C_l + \overline{C}_l) / \cos \Lambda \\ D &= \frac{1}{2} \rho V^2 c C_{d \Lambda} \\ M_{PA} &= \frac{1}{2} \rho V^2 c C_m - \frac{1}{2} \rho V^2 c C_{d \Lambda} (PA - 1/4) \sin \alpha_{BE} \\ &\quad + \frac{1}{2} \rho V^2 c^2 \left((PA - 1/4) C_l + (PA - 3/4) \overline{C}_l \right) \frac{\cos \alpha_{BE}}{\cos \Lambda} \\ &\quad + \frac{\pi \rho c^3}{16} (\ddot{h}_v - (PA - 3/8) (\ddot{\theta}_v + \Omega \dot{\beta}_v)) c \end{aligned} \right\} \quad (38)$$

Equations (38) are the final formulations of forces acting on a rotorcraft blade element when experiencing steady, oscillatory pitch, oscillating heaving, or combined motions. We shall now describe the method of modifying these expressions to account for hysteresis effects encountered when airfoils oscillate into high angles of attack where stall occurs.

STALL HYSTERESIS REPRESENTATION

The unsteady aerodynamics representation just discussed may be used directly to estimate force coefficients for airfoils oscillating in the linear aerodynamics area (i.e., below stall). For angles of attack above stall, the theory is extended to account for hysteresis effects which have been observed in oscillating airfoil tests (References 6, 7, and 11).

Gross and Harris¹² developed a method of approximating the observed hysteresis loops by utilizing two-dimensional static wind tunnel data and an empirically derived stall delay representation. The representation was subsequently used by Harris³ et al to obtain improved predictions of rotor performance. The method effectively modifies an instantaneous blade element angle of attack to a reference angle α_{REF} for use in entering two-dimensional force coefficient data. The reference angle of attack is given by

$$\alpha_{REF} = \alpha_{BE} - \left(\gamma \sqrt{\left| \frac{c\dot{\alpha}_{BE}}{2V} \right|} \right) (\text{sign } \dot{\alpha}) \quad (39)$$

where the function γ has been determined empirically from available oscillating test data. Positive $\dot{\alpha}$ reduces α_{REF} and delays stall and negative $\dot{\alpha}$ increases α_{REF} and stall. The $(\text{sign } \dot{\alpha})$ term carries the sense of the stall delay. The γ functions, which are a function of Mach number, have been determined for both lift stall delay γ_L and moment stall delay γ_M . It is significant to note that the numerical values of the two functions are different, indicating that the influence of $\dot{\alpha}$ is not the same for both lift and moment stall delays. The following development summarizes the approach to be used in treating stall hysteresis effects.

Figure 10 illustrates a typical trace for an airfoil in sinusoidal pitch oscillation. As noted in the figure, an airfoil which is set at a mean pitch angle just below static stall will encounter a stall condition on the upstroke of its oscillation. The point at which moment stall and lift stall occur may be determined, and the respective values of α and $\dot{\alpha}$ are available from test measured data. Using $\dot{\alpha}$, the function $\sqrt{|c\dot{\alpha}/2V|}$ is computed for the test point. This dimensionless parameter was selected by Gross and Harris¹² because of its similarity to the reduced frequency parameter k . Test data for a series of points with various mean angles, pitch frequencies, and oscillatory angles were used to construct curves like those in Figure 11. Correlations of this type confirmed that the selected parameter does normalize measured dynamic stall delay angles for a particular airfoil and Mach number. In these figures, the values shown at $\sqrt{|c\dot{\alpha}/2V|} = 0$ represent the stall angle for the nonoscillating or static test conditions. The incremental angle from the point to any given test condition represents the measured stall delay due to $\dot{\alpha}$ effects. Data of this type was accumulated by Liiva and Gray^{6, 7} for four airfoils: the V2301C-1.58, NACA 0012 MOD, V13006-.7 and NACA 0006.

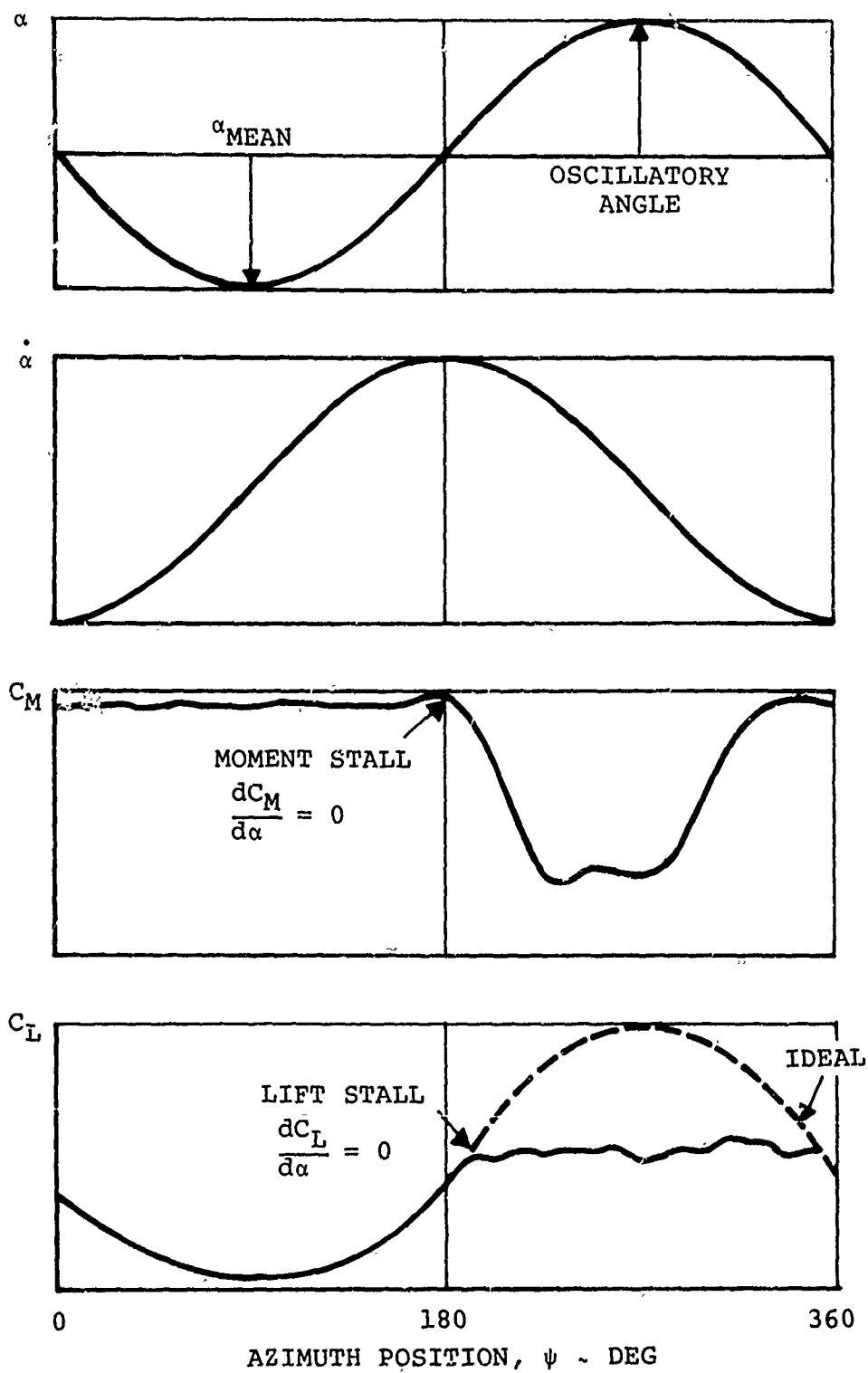
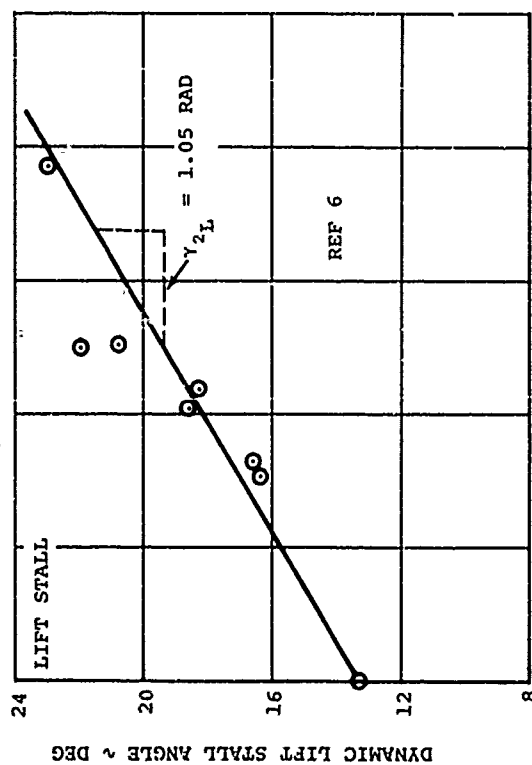


Figure 10. Typical Pitch Oscillation Test Data.

V23010-1.58 AIRFOIL
MACH NO. = .4



V13006-.7 AIRFOIL
MACH NO. = .4

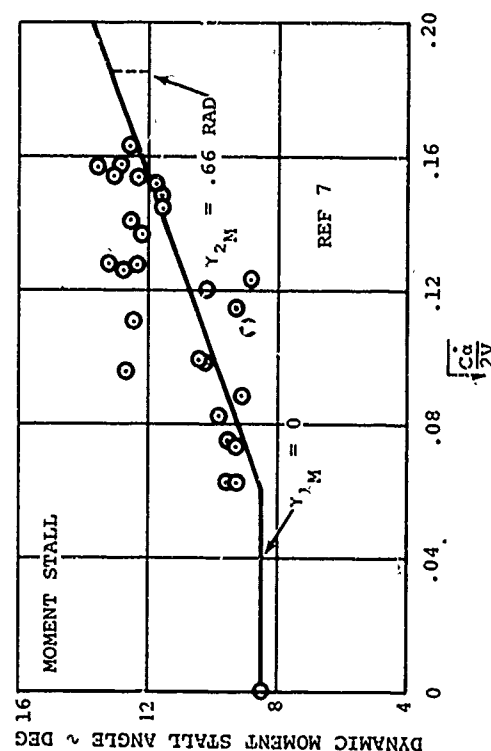
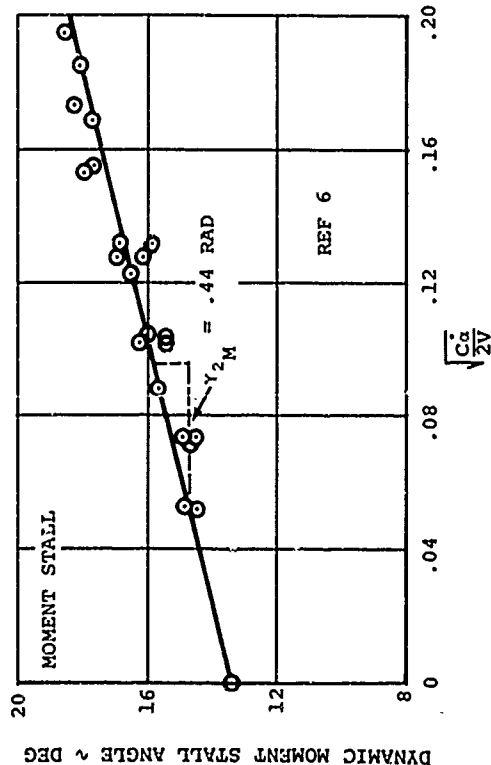
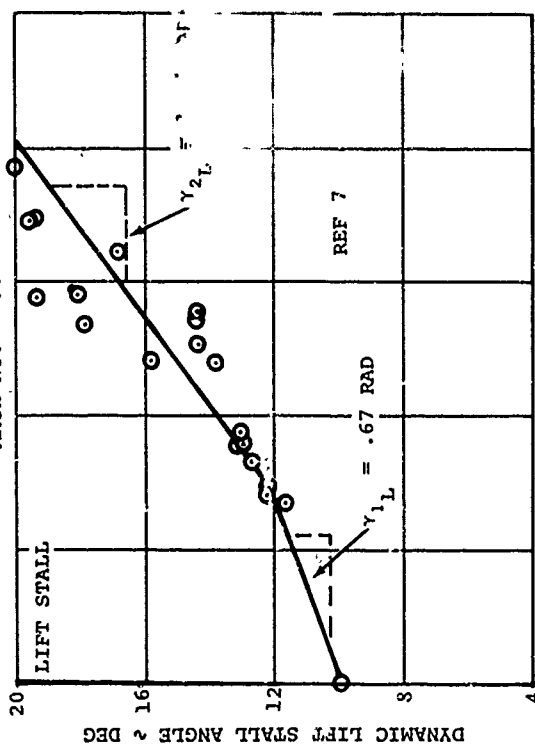


Figure 11. Typical Dynamic Stall.

Analysis of the measured test data revealed that some airfoils (in particular the 6-percent-thick sections, V13006-.7 and NACA 0006) could not be adequately represented by a single γ function. Consequently, they are represented by a compound slope formulation resulting in two γ values, γ_1 and γ_2 . For the thicker airfoils, a single value of γ was determined to be adequate for representing the variation in stall delay with $\dot{\alpha}$. This latter result is consistent with the work of Gross and Harris since they were primarily concerned with the behavior of the V230110-1.58 section in their original work.

For the four airfoils studied under this contract, a generalized formulation of the γ functions which is independent of airfoil section was developed. The airfoil maximum thickness ratio, t/c is the determining variable required to compute γ functions which agree with the measured test values. Equations (40) through (44) summarize the stall hysteresis formulation as a function of Mach number, M_N and airfoil maximum thickness ratio, t/c . Figure 12 is a schematic of the formulation; linear interpolation is used between the computed end points at M_{N1} , MAX γ_2 and at $M_N(\gamma_2 = 0)$, $\gamma_2 = 0$. The value of $\left| \frac{c\dot{\alpha}}{2V} \right|$ at which the slope changes from γ_1 to γ_2 is given in Equation (40), as illustrated in Figure 11.

$$\sqrt{\left| \frac{c\dot{\alpha}}{2V} \right|}_{\text{Break}} = .06 + 1.5 (.06 - t/c) \quad (40)$$

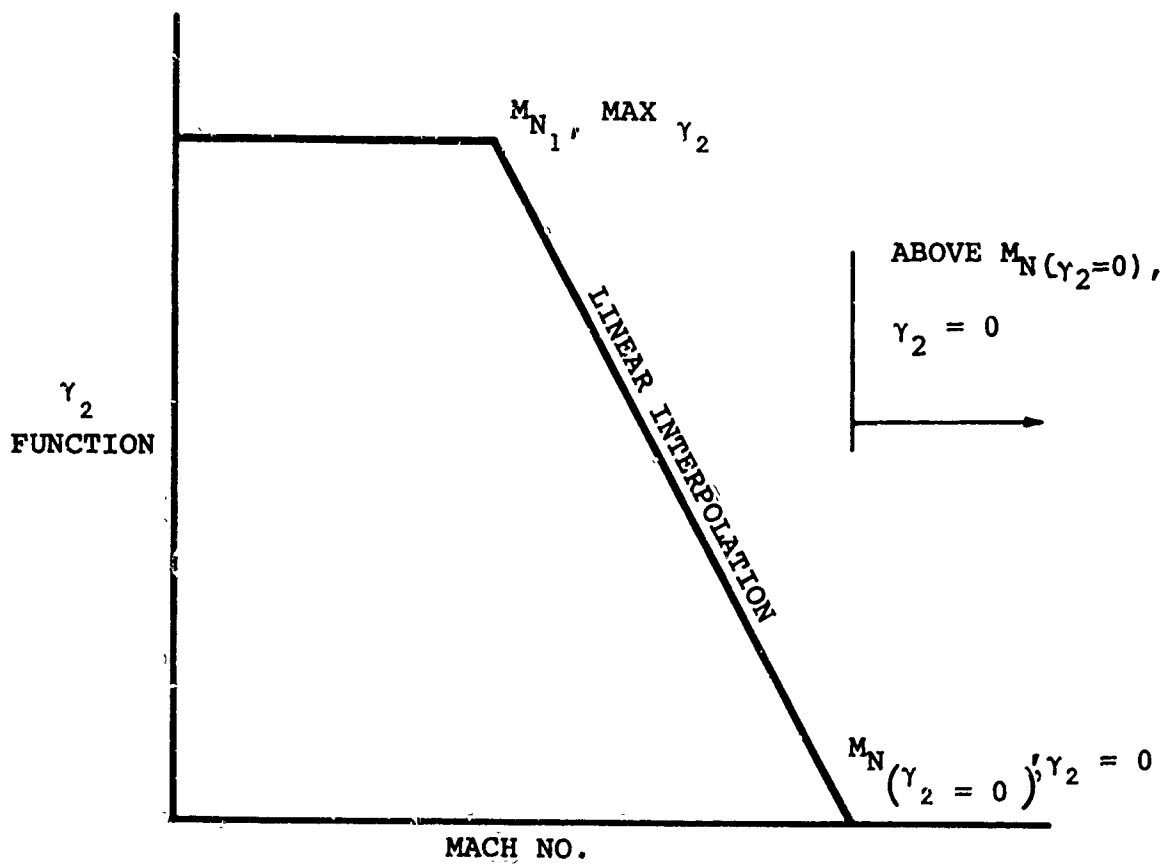


Figure 12. Schematic of Stall Hysteresis Formulation.

Lift Stall

$$M_{N_{1L}} = .4 + 5 (.06 - t/c)$$

$$\text{MAX } \gamma_{2L} = 1.4 - 6 (.06 - t/c)$$

$$M_{N(\gamma_{2L}=0)} = .9 + 2.5 (.06 - t/c)$$

$$\text{If Mach No.} < M_{N_{1L}}$$

$$\gamma_{2L} = \text{Max } \gamma_{2L}$$

$$\text{If Mach No.} > M_{N(\gamma_{2L}=0)}$$

$$\gamma_{2L} = 0.$$

$$\gamma_{1L} = .5 \gamma_{2L}$$

(41)

Moment Stall

$$M_{N_{1M}} = .2$$

$$\text{Max } \gamma_{2M} = 1. - 2.5 (.06 - t/c)$$

$$M_{N(\gamma_{2M}=0)} = .7 + 2.5 (.06 - t/c)$$

$$\text{If Mach No.} < M_{N_{1M}}$$

$$\gamma_{2M} = \text{Max } \gamma_{2M}$$

$$\text{If Mach No.} > M_{N(\gamma_{2M}=0)}$$

$$\gamma_{2M} = 0.$$

$$\gamma_{1M} = 0.$$

(42)

Dynamic Stall Angle of the Form $\alpha_{\text{Dynamic Stall}} = \alpha_{\text{Static Stall}} + \Delta \alpha_{\text{Dynamic Stall}}$

$$\text{For } \sqrt{\left| \frac{c\dot{\alpha}}{2V} \right|} < \sqrt{\left| \frac{c\dot{\alpha}}{2V} \right|}_{\text{Break}}$$

$$\alpha_{\text{Dynamic Stall (L, M)}} = \alpha_{\text{Static Stall (L, M)}} + \left(\gamma_1 (L, M) \sqrt{\left| \frac{c\dot{\alpha}}{2V} \right|} \right) (\text{sign } \dot{\alpha}) \quad (43)$$

$$\text{For } \sqrt{\left| \frac{c\dot{\alpha}}{2V} \right|} > \sqrt{\left| \frac{c\dot{\alpha}}{2V} \right|}_{\text{Break}}$$

$$\begin{aligned} \alpha_{\text{Dynamic Stall (L, M)}} = \alpha_{\text{Static Stall (L, M)}} + & \left[\gamma_1 (L, M) \sqrt{\left| \frac{c\dot{\alpha}}{2V} \right|}_{\text{Break}} \right. \\ & \left. + \gamma_2 (L, M) \left(\sqrt{\left| \frac{c\dot{\alpha}}{2V} \right|} - \sqrt{\left| \frac{c\dot{\alpha}}{2V} \right|}_{\text{Break}} \right) \right] (\text{sign } \dot{\alpha}) \quad (44) \end{aligned}$$

Figure 13 illustrates the correlation of the generalized stall delay formulation with measured test data for the airfoils studied.

Now referring to Equation (39), α_{Ref} can be represented as

$$\alpha_{\text{Ref (L, M)}} = \alpha_{\text{BE}} - K_1 \Delta \alpha_{\text{Dynamic Stall (L, M)}} \quad (45)$$

where $\Delta \alpha_{\text{Dynamic Stall}}$ is computed from Equations (40) through (44) using the incremental dynamic stall representations. This formulation has the effect of reducing angles of attack used to enter data tables for positive $\dot{\alpha}$, and increasing angle of attack for negative $\dot{\alpha}$. Hence the effect of $\dot{\alpha}$ (dependent on sign) is to adjust the reference angle of attack either out of stall (positive $\dot{\alpha}$) or deeper into stall (negative $\dot{\alpha}$). The dynamic stall formulation is derived from stall delay angles obtained during stall at positive $\dot{\alpha}$ (increasing angle of attack). An initial formulation assumed a mirror image effect for negative $\dot{\alpha}$; that is, $\Delta \alpha_{\text{Stall Dynamic}}$

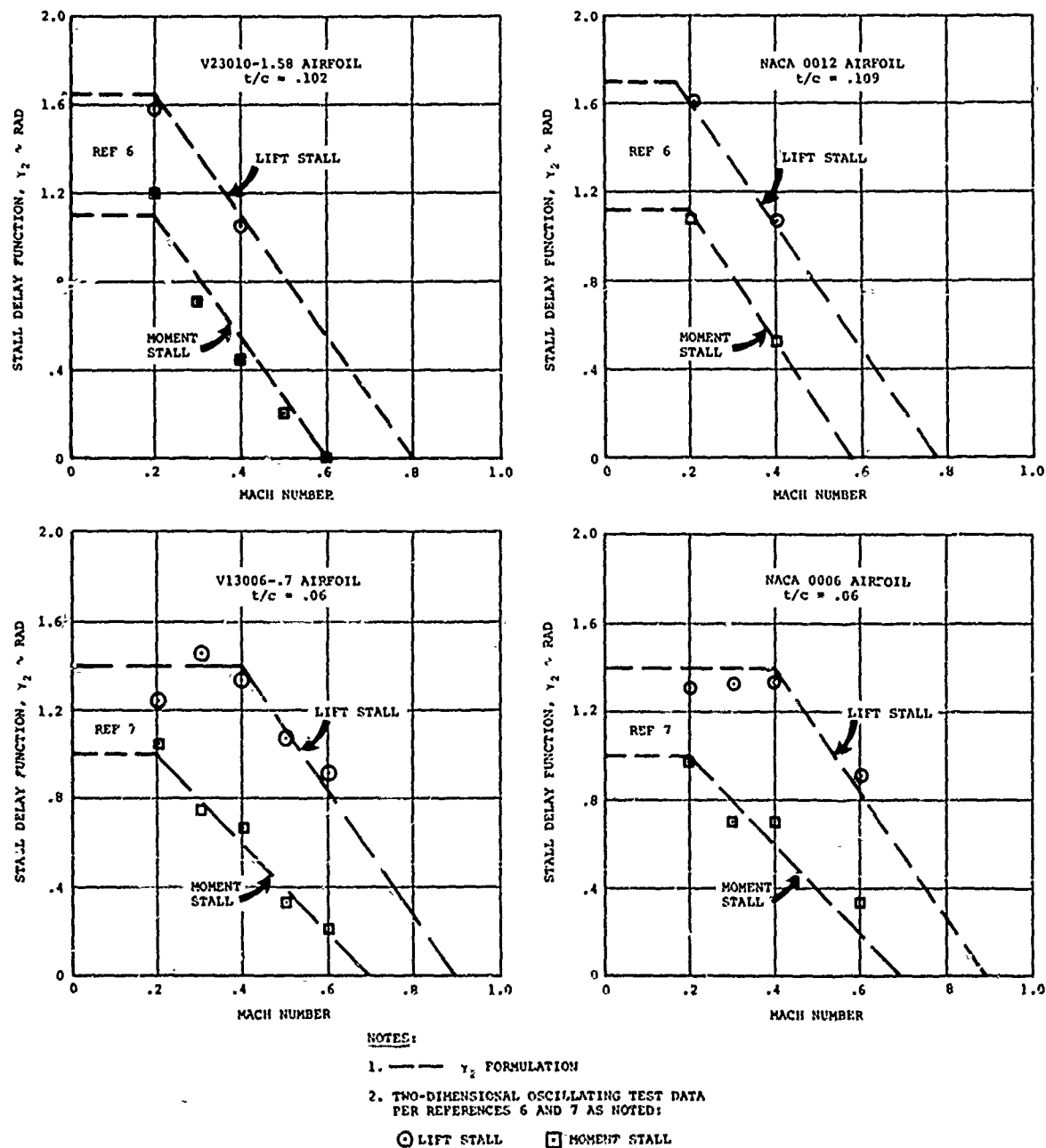


Figure 13. Stall Delay Functions.

had the same sensitivity for both positive and negative $\dot{\alpha}$. Subsequent correlation with two-dimensional test results indicated that this approach predicted premature stall for negative $\dot{\alpha}$ conditions. As a result, an empirical factor K_1 was introduced to adjust the sensitivity for $\dot{\alpha} < 0$. Values of $K_1 = 1$. for $\dot{\alpha} > 0$ and $K_1 = .5$ for $\dot{\alpha} < 0$ give improved correlation with available two-dimensional oscillating test data. Figure 14 shows the effect on stall correlation due to the application of the K_1 factor. $K_1 = 1$. for both positive and negative $\dot{\alpha}$ gives a premature stall prediction. $K_1 = 1$. for $\dot{\alpha} > 0$ and $K_1 = .5$ for $\dot{\alpha} < 0$ minimizes the premature stall prediction. Airfoil force coefficients obtained at α_{Ref} are identified as $C_{l_{Ref}}$, $C_{m_{Ref}}$, and $C_{d_{Ref}}$.

α_{Ref} for drag calculations is equal to α_{Ref} used in moment calculations. Drag rise is assumed to have the same delay as moment stall, since moment stall indicates a center of lift shift due to separated flow, which is coincident with drag rise. This assumption is necessary since measured dynamic drag data are not available.

The final force coefficients are computed as

$$\left. \begin{aligned} C_l &= \left(\frac{C_{l_{Ref}}}{\alpha_{Ref_L} - \alpha_{c_l=0}} \right) \alpha_{BE} = f(\alpha_{BE}, \alpha_{Ref_L}, M_N) \\ C_m &= C_{m_{Ref}} = f(\alpha_{Ref_M}, M_N) \\ C_d &= C_{d_{Ref}} = f(\alpha_{Ref_M}, M_N) \end{aligned} \right\} \quad (46)$$

where the impact of stall hysteresis on lift adjusts the effective lift curve slope for α_{BE} above stall. Note that when α_{BE} and α_{Ref} are both below stall, the effective lift slope and C_l are identical to the linear value which would be obtained without the stall hysteresis representation. Only when α_{BE} and/or α_{Ref} are above static stall angles does the representation affect C_l values. Similar comments apply to the C_m and C_d values computed.

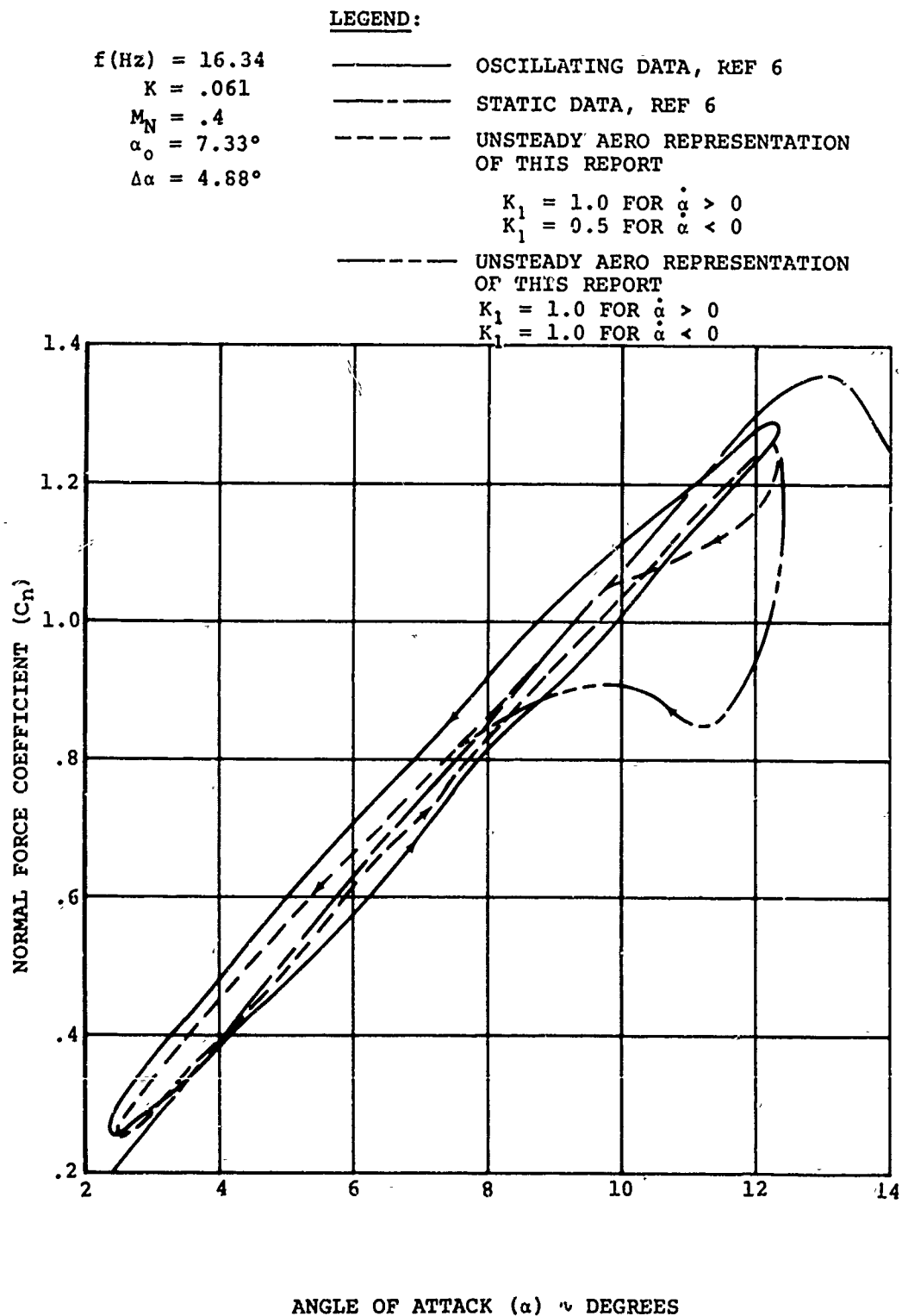


Figure 14. Influence of Empirical K_1 Factor on Correlation at Negative α .

The final formulation is derived by incorporating the stall hysteresis effects (Equation 46) and the radial flow effects (Equations 35, 36, and 37) into the unsteady aerodynamics representation (Equation 34). From Equation (46), the term $C_{l_{Ref}} / (\alpha_{Ref_L} - \alpha_{c_l=0})$ represents an effective, or dynamic, lift curve slope and replaces the lift slope, 2π , derived from potential flow theory.

Letting

$$\alpha_{EQU} = \left\{ \text{see Equation (31)} \right\} \quad (47)$$

$$\bar{\alpha} = \frac{c}{4} \left(\frac{1}{V} (\dot{\theta}_v + \Omega \beta) + \frac{\ddot{h}_v}{V^2} - (PA - 1/2) (\ddot{\theta}_v + \Omega \dot{\beta}_v) \frac{c}{V^2} \right) \quad (48)$$

$$C_d = C_{d_{Ref}} + C_{d_{SF}} (\sec \Lambda - 1) \quad (49)$$

the complete formulation is

$$L = \frac{1}{2} \rho V^2 c \left(\frac{C_{l_{Ref}}}{\cos \Lambda (\alpha_{Ref_L} - \alpha_{c_l=0})} \right) \left\{ \alpha_{EQU} + \bar{\alpha} \right\} \quad (50)$$

$$D = \frac{1}{2} \rho V^2 c C_d \quad (51)$$

$$\begin{aligned} M_{PA} = & \frac{1}{2} \rho V^2 c^2 C_{m_{Ref}} + \frac{1}{2} \rho V^2 c^2 (PA - 1/4) C_d \sin \alpha_{BE} \\ & + \frac{1}{2} \rho V^2 c^2 \left(\frac{C_{l_{Ref}}}{\cos \Lambda (\alpha_{Ref_L} - \alpha_{c_l=0})} \right) \left\{ \left(\alpha_{EQU} (PA - 1/4) \right. \right. \\ & \left. \left. + \bar{\alpha} (PA - 3/4) \right) \cos \alpha_{BE} \right\} \\ & + \frac{\pi \rho c^3}{16} \left(\ddot{h}_v - (PA - 3/8) (\ddot{\theta}_v + \Omega \dot{\beta}_v) c \right) \end{aligned} \quad (52)$$

The unsteady aerodynamics methodology is correlated with two-dimensional oscillating airfoil data in Appendix I. Appendix II contains correlations of the revised C-81 (AGAJ71) analysis with test data for isolated rotors and complete rotorcraft configurations.

RADIAL FLOW REPRESENTATION

REVIEW OF RADIAL FLOW METHODS

Classical propeller and rotor analyses assumed that blade element airloads and performance could be computed utilizing the independence principle; i.e., aerodynamic forces on a yawed blade element occur only in a plane perpendicular to the span and are proportional to the square of the velocity component in that plane. In reality, total velocity can be substantially higher than the normal component, and can act at large sweep angles relative to the span axis. Recent publications on this subject indicate that accurate rotor performance and airload prediction are compromised when the radial component of velocity is ignored.

There are generally two approaches being pursued in an effort to estimate radial flow effects on rotary-wing aircraft: (1) a theoretical approach to solving the behavior of airfoil boundary layer in the presence of radial flow, and (2) empirical interpretations of available test data for yawed airfoil sections.

From the theoretical aspect, McCroskey and Dwyer¹³ have published a comprehensive method of analyzing boundary layer growth over airfoil sections in a yawed flow environment. This publication is the result of a continuing study, starting with basic theories and building a solid theoretical understanding, in an effort to understand the impact of radial flow on rotor lift and drag. The following is a summary of the significant features and limitations of their analysis:

- Features

- Perturbation Analysis

- Small crossflow and quasi-steady approximations

- Reduces independent variables from four to two

Not useful for separation characteristics

Suspect near separation

Gives relative significance of crossflow and unsteady effects

Linearized Analysis

More relevant to problems involving separation

Gives qualitative details of flow field

Numerical Analysis

No simplifying approximations

Treats flow field to point of separation

Evaluates significance of approximations of the perturbation and linearized analyses

● Limitations

Treats only laminar incompressible flow

Does not treat oscillating angle of attack

Neglects trailing vorticity

Treats separation results for 3-D steady and 2-D unsteady flows, not 3-D unsteady flows (real rotor environment)

Complete potential flow (serves as boundary condition at edge of boundary layer) not available. Uses infinite blade with constant circulation.

● Applications to Rotor Analyses

Real flows have transition to turbulent boundary layer and attendant delay in separation. Thus, realistic representation of airfoil characteristics would require a laminar-turbulent analysis.

Boundary-layer analysis internal to production computer program would be restrictive due to time requirements. Simplified representation (probably empirical) would be more desirable.

Although the work of McCroskey and Dwyer represents a significant advancement in understanding the mechanism of radial flow effects on rotary-wing boundary layers, the present limitations of the analysis preclude use in a rotor analysis such as the Government's Rotorcraft Flight Simulation Program C-81 (AGAJ71). In particular, the requirements for three-dimensional unsteady flows and a laminar-turbulent analysis need to be satisfied in order to make such an analysis practical and justifiable. For rotor analysis applications, a more simplified or empirical method is desirable.

The impact of empirical approximations to radial flow effects has been summarized by Harris^{3, 14}. Utilizing simplified approximations for representing radial flow effects, Harris has been able to demonstrate marked improvements in rotor performance and airloads predictions compared to results predicted by quasi-static, normal flow (independence principle) rotor theories. Conventional flow theories assume that only the velocity component normal to the blade span axis need to be considered when computing airloads. The significant features of Harris' method are that it accounts for increased lift capability, when stall is delayed due to radial flow on a yawed airfoil, and for increased skin friction drag (above values computed by normal flow theories), which is calculated using the resultant velocity acting at the blade element. Harris' method is an empirical approximation based on observed experimental data and is summarized in the discussion on THE EFFECTS OF RADIAL FLOW which follows. Due to the simplified numerical procedures, incorporation of an analysis of the type developed by Harris can provide a significant improvement in predictive capability with little increase in required computer time.

Harris' empirical formulation for treating radial flow effects has been selected as the most practical method available. The radial flow analysis which has been included in the flight simulation program of this contract has been described earlier in this report in MODIFICATION TO COMPRESSIBLE FLOW AND ROTATING ENVIRONMENT.

THE EFFECTS OF RADIAL FLOW

The effect of radial flow on blade element forces takes the form of two distinct phenomena. Radial flow affects section drag level (in particular, skin friction drag) and the orientation of the drag vector, and it affects maximum C_l capability. The following paragraphs detail these results.

EFFECT OF RADIAL FLOW ON DRAG

Figure 15 illustrates the velocity diagram for a general blade element of a rotor blade. For simplification, only velocity components in the disc plane are shown.

Classical rotor analyses assumed that the blade element force vectors could be assumed to act normal to the plane span axis (i. e., in the direction of U_T) and were proportional to U_T^2 . However, Harris¹⁴ concluded that this approach was optimistic when calculating drag since the airfoil actually experienced a much higher velocity acting at an oblique angle. He also found that the skin friction drag coefficient ($C_{d_{SF}}$) did not decrease in the yawed plane. This is contrary to intuitive feel since in the yawed plane the airfoil section appears to have a lower thickness ratio t/c , and it has a higher Reynolds number due to its increased chord and velocity. Both of these phenomena tend to reduce the skin friction drag coefficient of conventional two-dimensional sections. In fact, some evidence indicated the $C_{d_{SF}}$ actually increased for yawed flow. As a first approximation, the conclusion was drawn that $C_{d_{SF}}$ is independent of yaw angle and should be evaluated on the basis of chord, velocity, t/c , and R_c normal to the span axis. Therefore,

$$\frac{C_{d_{SF \Lambda}}}{C_{d_{SF \Lambda = 0}}} = 1.0 \quad (53)$$

where

$$\Lambda = \tan^{-1} \left(\frac{U_R}{U_T} \right)$$

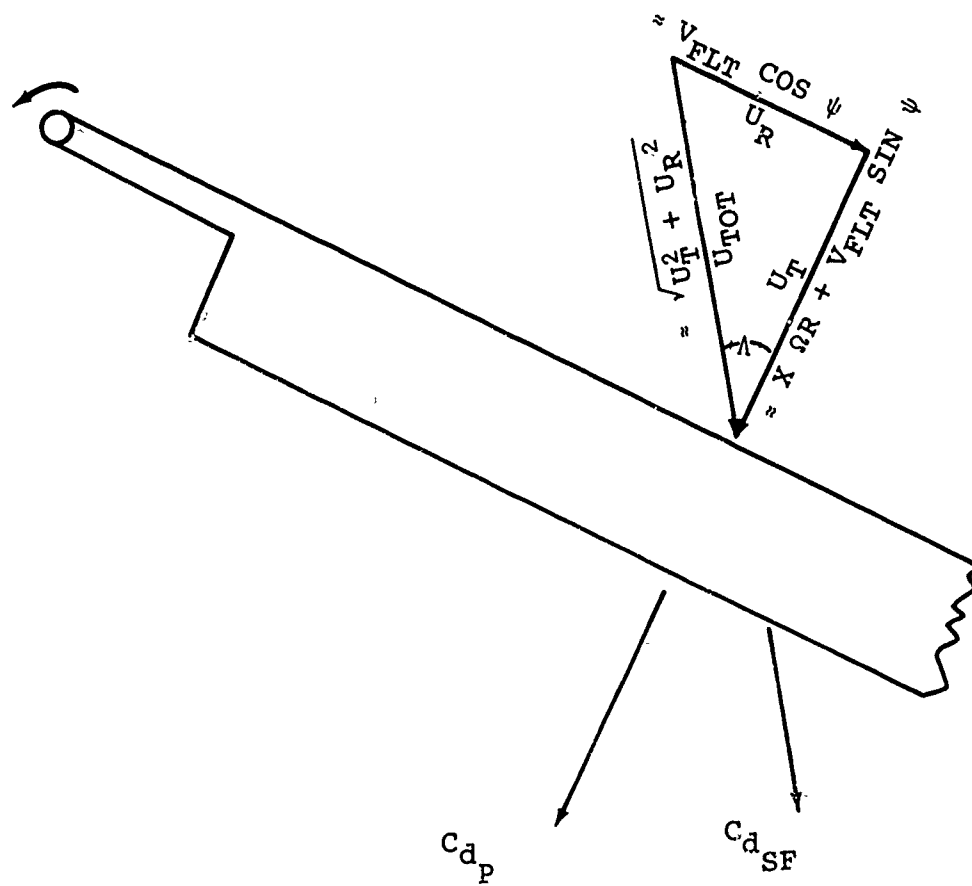


Figure 15. Blade Velocity Diagram.

The pressure drag component (C_{dp}) is unaffected by the assumption that it acts in the blade-normal plane. Lippisch and Beuschausen¹⁵ documented pressure distributions for sections in yawed flows up to $\Lambda = 40$ degrees and concluded that the chordwise pressure distributions were essentially unaltered. Figure 16 illustrates typical chordwise pressure distributions for a 9-percent-thick symmetric hyperbolic section. Its angle-of-attack range is limited, but its Mach-number range is extensive. Both show good agreement when the pressure distributions for various yaw angles are normalized by the dynamic pressure normal to the span. The pressure coefficient corresponding to a local Mach number of 0 or 1 for the given free stream conditions is shown when it falls within the range of the ordinate scale.

The drag vectors for a blade element can therefore be derived as follows.

Skin Friction Drag Components

$$\Delta D_{SF_RESULT} = \frac{\rho}{2} C_{d_SF} c U_{TOT}^2 \quad (54)$$

In the blade-normal plane:

$$\Delta D_{SF_NORMAL} = \frac{\rho}{2} C_{d_SF} c U_{TOT}^2 \cos \Lambda \quad (55)$$

but

$$U_{TOT} = U_T / \cos \Lambda \text{ and} \quad (56)$$

$$\Delta D_{SF} = \frac{\rho}{2} C_{d_SF} c U_T^2 \sec \Lambda \quad (57)$$

In the blade radial direction:

$$\Delta D_{SF_RADIAL} = \frac{\rho}{2} C_{d_SF} c U_{TOT}^2 \sin \Lambda \quad (58)$$

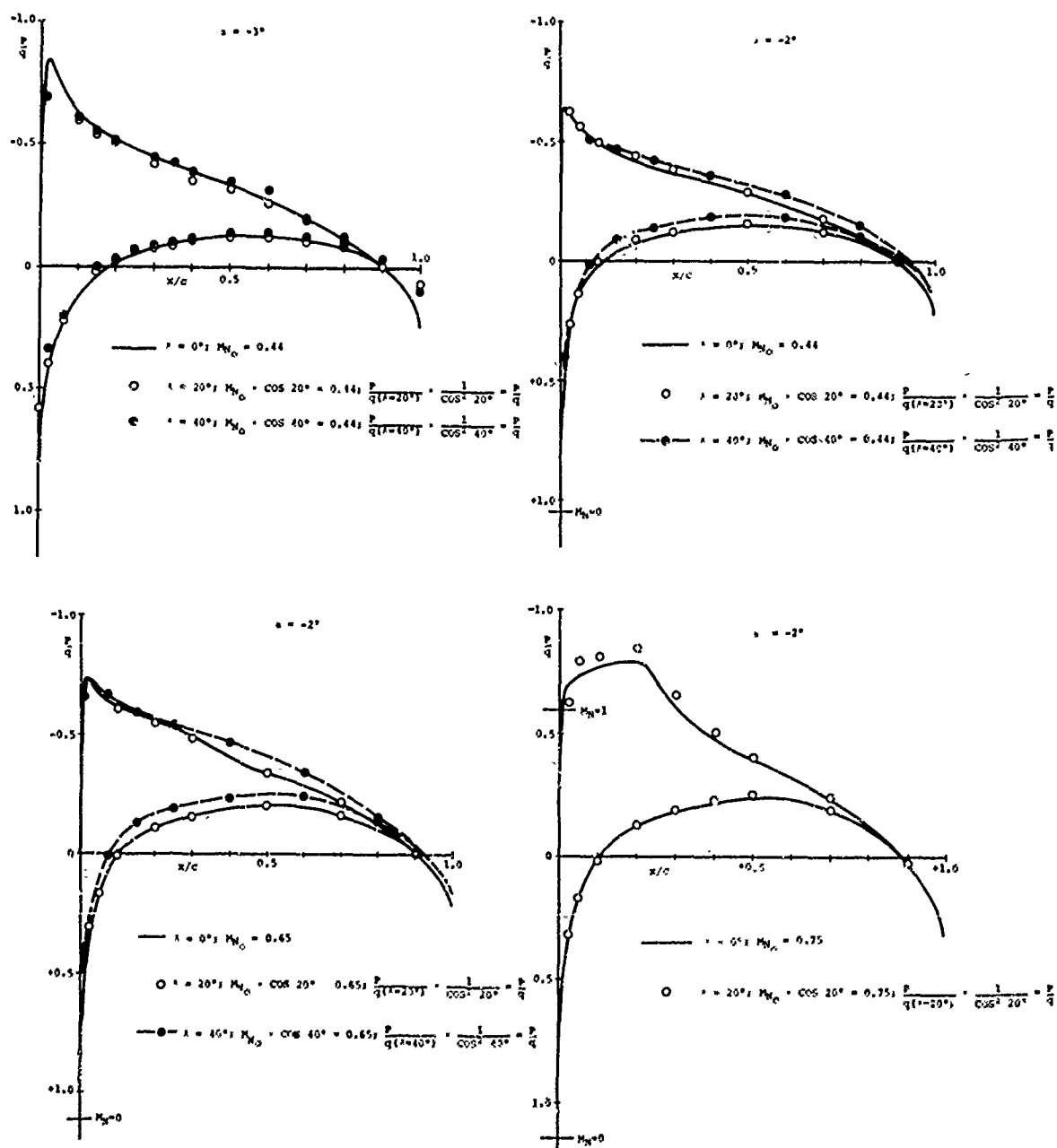


Figure 16. Chordwise Pressure Distributions of a 9-Percent-Thick Symmetric Hyperbolic Profile Having a t/c_{\max} at 40- Percent Chord (Reference 15).

where $\sin \Lambda = U_R/U_{TOT}$

$$\Delta D_{SF\text{RADIAL}} = \frac{\rho}{2} C_{dSF} c U_{TOT} U_R \quad (59)$$

Pressure Drag Components

$$\Delta D_{P\text{NORMAL}} = \frac{\rho}{2} C_{dp} c U_T^2 \quad (60)$$

$$\Delta D_{P\text{RADIAL}} = 0 \quad (61)$$

Drag Summary Equations

Combining the drag components normal to the span axis:

$$D_{\text{NORMAL}} = \frac{\rho}{2} c U_T^2 \left(C_{dSF} \sec \Lambda + C_{dp} \right) \quad (62)$$

$$= \frac{\rho}{2} c U_T^2 \left(C_{dSF} + C_{dp} + C_{dSF} (\sec \Lambda - 1) \right) \quad (63)$$

where

$$C_{dSF} + C_{dp} \equiv C_{d_{2-D}}$$

The combined terms $C_{dSF} + C_{dp}$ correspond to the total C_d value contained in conventional two-dimensional table look-up data.

$$D_{\text{NORMAL}} = \frac{\rho}{2} C U_T^2 \left(C_{d_{2-D}} + C_{dSF} (\sec \Lambda - 1) \right) \quad (64)$$

In the radial direction:

$$D_{\text{RADIAL}} = \frac{\rho}{2} c U_{TOT} U_R C_{dSF} \quad (65)$$

Skin Friction Drag Coefficient

Since skin friction drag components are normally not known for specific airfoils, a general formulation (shown to agree with a variety of section data) is presented in

the following paragraph. This formulation may be used on an incremental basis in the drag equations just presented.

For thin airfoils, skin friction drag may be initially assumed as a function of skin friction on a flat plate:

$$C_{d_{SF}} = 2 C_f \quad (66)$$

where C_f is the skin friction coefficient for one side of a flat plate. Hoerner¹⁶ determined that the increase in skin friction due to flow acceleration over an airfoil of finite thickness is

$$\frac{\Delta C_{d_{SF}}}{2 C_f} = 2 \frac{t}{c} \quad (67)$$

The skin friction coefficient is obtained by adding equations (66) and (67)

$$C_{d_{SF}} = 2 C_f \left(1 + 2 \frac{t}{c} \right) \quad (68)$$

Adding a pressure (or separation) drag component, $C_{d_{PR}}$, equal to $2 C_f \left[60 \left(\frac{t}{c} \right)^4 \right]$ makes up the total viscous profile drag:

$$C_{d_{\text{Viscous Profile}}} = 2 C_f \left(1 + 2 \frac{t}{c} + 100 \left(\frac{t}{c} \right)^4 \right) \quad (69)$$

The separation term is not significant below t/c_{\max} values of about 20 percent. The above equation is valid for airfoils with t/c_{\max} located near 30-percent chord position. For sections with t/c_{\max} near 40- to 50-percent chord (laminar flow airfoils), Hoerner obtained a similar expression.

Results given by

$$C_{d_{\text{Viscous Profile}}} = 2 C_f \left(1 + 1.2 \frac{t}{c} + 60 \left(\frac{t}{c} \right)^4 \right) \quad (70)$$

However, for airfoil sections used in typical helicopter applications, maximum thickness ratio is generally less than 20 percent, and it is located near 30-percent

chord. Therefore, the profile drag is dominated by the skin friction drag coefficient, and it reduces to

$$C_{d_{SF}} = 2 C_f \left(1 + 2 \frac{t}{c} \right) \quad (71)$$

Hoerner defines the flat plate turbulent skin friction as

$$C_f = \frac{.044}{R_c^{1/6}} \text{ for } 10^6 < R_c < 10^8 \quad (72)$$

which gives

$$C_{d_{SF}} = \frac{.088}{R_c^{1/6}} \left(1 + 2 \frac{t}{c} \right) \quad (73)$$

Figure 17 compares this expression ($t/c = .1$) with typical section data. The range of acceptable agreement has a lower limit of $R_c \approx 1.7 \times 10^5$, where laminar flow effects begin to dominate.

EFFECT OF RADIAL FLOW ON LIFT

The effect of radial flow on section C_l is manifested as an apparent increase in $C_{l_{max}}$ capability when referenced to velocities in the plane normal to the span axis. At angles below stall, there is no observable effect on the combinations of angle of attack and C_l ; therefore, the slope of the lift curve is unaltered.

However, at high angles of attack, where yawed static test data would indicate a stalled condition, the yawed section exhibits substantial increases in C_l capability. Figure 18 summarizes the findings of Carta et al², Purser and Spearman²¹, Critzos et al²², and Lizak²³ with respect to the effect of yawed flow on section C_l . The important effect is an improvement in the $C_{l_{max}}$ attainable at high angles of attack, where normal two-dimensional section data exhibits a stalled condition. The data of Figure 18 is referenced to the velocity component normal to the span axis and,

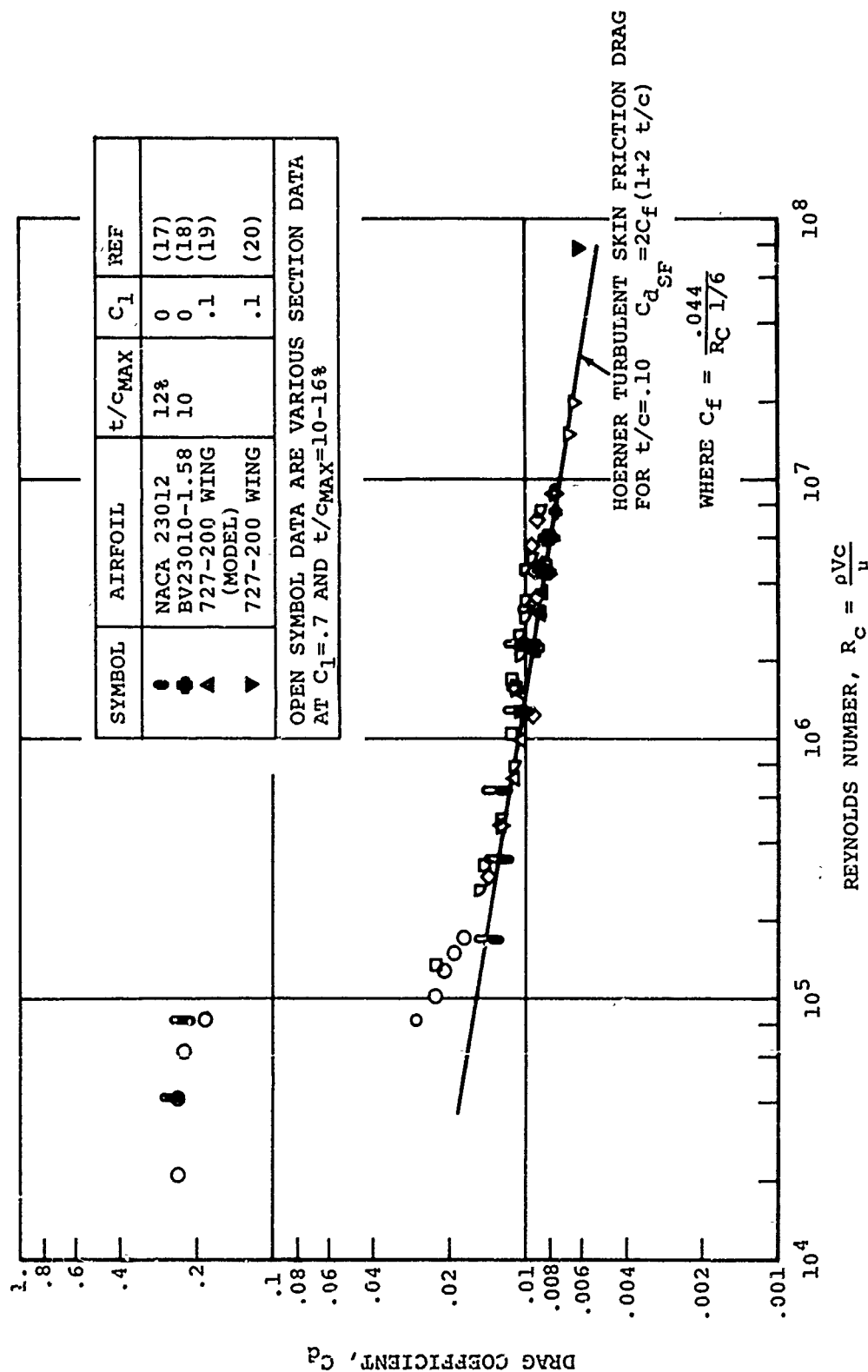


Figure 17. Effect of Reynolds Number on C_d .

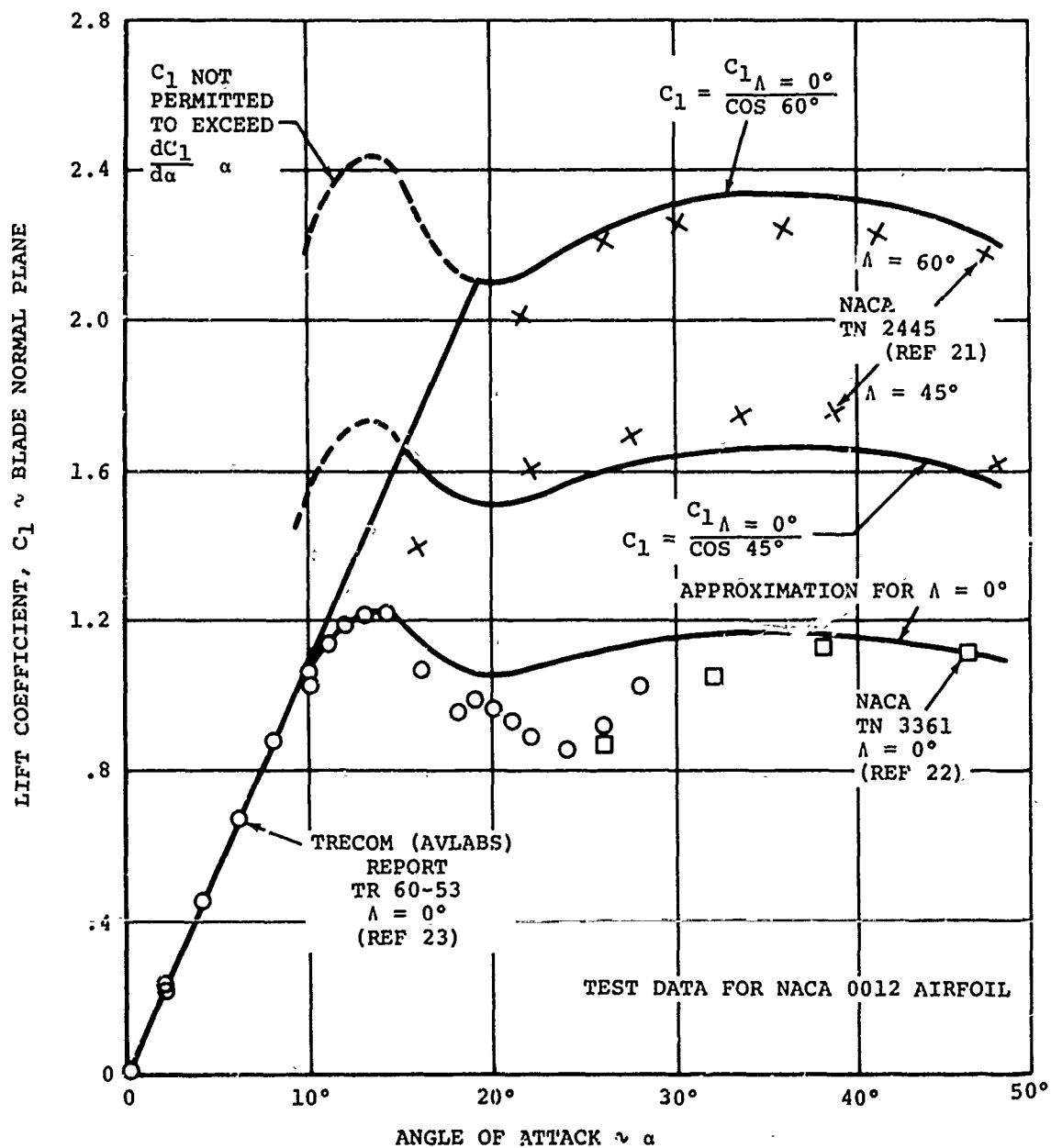


Figure 18. Yawed Flow Effects Delaying Stall.

therefore, is in the plane of conventional rotor force calculations. Harris et al³ found a reasonable approximation to these data to be

$$C_{l_{\max \Lambda}} = \frac{C_{l_{\max \Lambda = 0}}}{\cos \Lambda} \quad (74)$$

where Λ is the sweep angle defined by $\tan^{-1} (U_R / U_T)$

A useful formulation of this approximation is to adjust available two-dimensional $C_l - \alpha$ tables to the required yaw angle by

$$C_{l_{\Lambda}} = \frac{C_{l_{\Lambda = 0}}}{\cos \Lambda} \quad (75)$$

However, this equation would result in increased lift curve slopes for angles of attack in the nonstalled regime. Since the yawed flow test data do not indicate any increase in lift curve slope in the linear range, the formulation must be limited to

$$C_{l_{\Lambda}} \leq \left(\frac{dC_l}{d\alpha} \right)_{\substack{\text{Linear} \\ \Lambda = 0}} \alpha \quad (76)$$

USER'S MANUAL

REVISED INPUT REQUIREMENTS

The revisions incorporated in the Government's Rotorcraft Flight Simulation program as part of this contract require few changes in the input requirements of the program. (Reference 4 describes the basic input requirements of the program.) Additional inputs are required only for the unsteady aerodynamics and yawed flow versions of the program.

The unsteady aerodynamics on/off switch has been retained from the previous version of this program. It is controlled by input location XMR (26) for the main/forward/right rotor and by location XTR(26) for the tail/aft/left rotor. For both rotors, a value of location 26 ≤ 0 , turns the unsteady aerodynamics representation off, and location 26 > 0 , turns the representation on. Any group of on/off combinations may be used: unsteady aerodynamics may be used on no rotors, both rotors, forward rotor only, or aft rotor only.

The yawed flow representation requires an additional control input and is designated YAWFLO (N). N takes the value 1 for the main/forward/right rotor and the value 2 for the tail/aft/left rotor. YAWFLO(N) may take four values of significance:

- YAWFLO (N) = 0. no yaw flow effects
- = 1. yaw flow effects on skin friction drag only
- = 2. yaw flow effects on lift coefficient only
- = 3. yaw flow effects on lift and drag coefficient

Again, any combination of control inputs may be used for the two rotors.

In the unsteady aerodynamics formulation, values are required for angle of attack at zero lift coefficient. In order to avoid time-consuming table look-up, these values have been represented by a third-order curve fit as a function of Mach number. The representation is of the form

$$\alpha_{C_1=0} = \text{ALFIN1 (N)} + \text{ALFIN2 (N)} * M_N$$

$$+ \text{ALFIN3 (N)} * M_N^2 + \text{ALFIN4} * M_N^3 \quad (77)$$

where N = 1 for main/forward/right rotor

N = 2 for tail/aft/left rotor.

Input units are in degrees and are converted internally to radians.

For skin friction drag coefficients in the yawed flow representation and stall hysteresis effects in the unsteady aerodynamics representation, airfoil maximum thickness t/c ratio is required. This parameter is designated TDIVC (N) and is input as a decimal fraction (e.g., for a 12-percent-thick airfoil, TDIVC = 0.12).

All these additional inputs are contained on one input data card per rotor. The card is located after the cards allocated to blade twist distribution and prior to cards allocated for rotor elastic mode shapes. For example, for the main/forward/right rotor the additional input follows XMT (1-21) and precedes XMRMS (1-66), and for the tail/aft/left rotor the additional input follows XTT (1-21) and precedes XTRMS (1-66). The data card format is consistent with other input and is 6F10.0. The data input order for this card is: YAWFLØ ALFIN1 ALFIN2 ALFIN3 ALFIN4 TDIVC. Reference 24 gives the precise location of these data in the input deck setup.

PROGRAM FLOW FOR REVISED AREAS

The sequence of calculations performed in the rotor analysis section has been revised slightly. Figure 19 shows both the original and revised flow paths of the program. Minor revisions are required to introduce the unsteady aerodynamics and yawed flow subroutine (UNSTED) into the computations when these effects are desired. For cases where unsteady zero and yawed-flow are not used, the flow is unchanged, except that subroutine CMCALC has been deleted. Unsteady aero effects on pitching moment have been included in the UNSTED subroutine developed under this contract. Therefore, CMCALC is no longer needed.

NUMERICAL STABILITY AND EFFECT OF UNSTEADY AERODYNAMICS ON C-81 CONVERGENCE

Throughout the correlation phase of this contract, no numerical instabilities were encountered. The combined rotor aeroelastic solution and the unsteady aerodynamics formulation obtained numerically stable solutions to the various rotor flight conditions shown in Appendix II of this report. However, to reduce run time, care should be exercised in selecting initial estimates of flight constants used for inputs. Good estimates will result in more rapid convergence of the program solution and a corresponding reduction in computer run time.

The use of the unsteady aerodynamics option does result in increased computer running time for some cases. This is due to the complex interrelationship of the nonlinear unsteady aerodynamics forcing functions and rotor blade dynamic responses. During correlation efforts, it was found that the use of the unsteady aerodynamic option resulted in computer running times which ranged from negligible increase above the basic C-81 running time to as much as a 100% increase in running time. Below dynamic stall, the use of unsteady aerodynamics does not significantly improve the prediction capability, but it does increase running time. Thus it is recommended that the unsteady aerodynamics option be used only when operating at lift and speed conditions which produce rotor stall.

Use of the radial flow option results in negligible additional computer running time, and provides a more realistic representation of airfoil lift and skin friction drag coefficients than was available in the previous C-81 formulation. It is recommended that the radial flow option be used for all computer cases.

LITERATURE CITED

- (1) Ericsson, L.E., and J.P. Reding, UNSTEADY AIRFOIL STALL, Lockheed Missiles and Space Company, NASA CR-66787, National Aeronautics and Space Administration, Washington, D.C., July 1969.
- (2) Carta, F.O., L.M. Casellini, P.J. Arcidiacono, and H.L. Elman, ANALYTICAL STUDY OF HELICOPTER ROTOR STALL FLUTTER, Presented at the 26th Annual National Forum of the American Helicopter Society, Washington, D.C., June 1970.
- (3) Harris, F.D., F.J. Tarzanin, Jr. and R.K. Fisher, Jr., ROTOR HIGH SPEED PERFORMANCE, THEORY vs TEST (paper presented to the V/STOL Technology and Planning Conference at the Air Force Flight Dynamics Laboratory), Journal of the American Helicopter Society, Vol. 15, No. 3, July 1970.
- (4) Ericsson, L.E., and J.P. Reding, UNSTEADY AIRFOIL STALL AND STALL FLUTTER, Lockheed Missiles and Space Company, NASA CR-111906, National Aeronautics and Space Administration, Washington, D.C., June 1971.
- (5) Theodorsen, T., GENERAL THEORY OF AERODYNAMIC INSTABILITY AND THE MECHANISM OF FLUTTER, NACA Report 496, National Advisory Committee for Aeronautics, Washington, D.C., 1935.
- (6) Liiva, J., F.J. Davenport, L. Gray, and I.C. Walton, TWO-DIMENSIONAL TESTS OF AIRFOILS OSCILLATING NEAR STALL, The Boeing Company, Vertol Division; USAAVLABS Technical Report 68-13, Volumes I and II, U.S. Army Aviation Materiel Laboratories, Fort Eustis, Virginia, April 1968, AD 676957 and AD 670958.
- (7) Gray, L., J. Liiva, and F.J. Davenport, WIND TUNNEL TESTS OF THIN AIRFOILS OSCILLATING NEAR STALL, The Boeing Company, Vertol Division, USAAVLABS Technical Report 68-89, Volumes I and II, U.S. Army Aviation Materiel Laboratories, Fort Eustis, Virginia, January 1969, AD 684323 and AD 684324.

- (8) Tompkins, J. , L. Mirandy, and A. Freeman, MODEL ROTOR BLADE LOADS, BLADE MOTIONS AND PERFORMANCE STUDY (8 FT. DIAMETER CH-47B AND AGB ROTORS - UMWT 516), The Boeing Company, Vertol Division, Boeing Document D8-2338-1, April 1969.
- (9) McCloud, J.L. , III, J.C. Biggers, and R.H. Straub, AN INVESTIGATION OF FULL-SCALE HELICOPTER ROTORS AT HIGH ADVANCE RATIOS AND ADVANCING TIP MACH NUMBERS, NASA TN D-4632, National Aeronautics and Space Administration, Washington, D.C. , July 1968.
- (10) Bisplinghoff, R.L. , H. Ashley, and R.L. Halfman, AERO-ELASTICITY, Cambridge, Massachusetts, Addison-Wesley Publishing Company, Inc. , 1955, pp. 251-281.
- (11) Carta, F.O., EXPERIMENTAL INVESTIGATION OF THE UNSTEADY AERODYNAMIC CHARACTERISTICS OF AN NACA 0012 AIRFOIL, United Aircraft Research Laboratories Report M-1283-1, August 1960.
- (12) Gross, D.W. , and F.D. Harris, PREDICTION OF INFLIGHT STALLED AIRLOADS FROM OSCILLATING AIRFOIL DATA, Presented at the 25th Annual National Forum of the American Helicopter Society, Washington, D.C. , May 1969.
- (13) McCroskey, W.J. , and H.A. Dwyer, METHODS OF ANALYZING PROPELLER AND ROTOR BOUNDARY LAYERS WITH CROSSFLOW, NASA SP-228, National Aeronautics and Space Administration, Washington, D.C. , 1971.
- (14) Harris, F.D. , PRELIMINARY STUDY OF RADIAL FLOW EFFECTS ON ROTOR BLADES, Journal of the American Helicopter Society, Vol. 11, No. 3, July 1966.
- (15) Lippisch, A. , and W. Beuschausen, PRESSURE DISTRIBUTION MEASUREMENTS AT HIGH SPEED AND OBLIQUE INCIDENCE OF FLOW, NACA TM 1115, National Advisory Committee for Aeronautics, Washington, D.C. , March 1947.
- (16) Hoerner, Dr. S.F. , FLUID-DYNAMIC DRAG, Second Edition, Midland Park, New Jersey, Published by the Author, 1965, pp. 6.5-6.6.

- (17) Jacobs, E.N., and A. Sherman, AIRFOIL SECTION CHARACTERISTICS AS AFFECTED BY VARIATIONS OF THE REYNOLDS NUMBER, NACA R-586, National Advisory Committee for Aeronautics, Washington, D.C., 1937.
- (18) La Prete, R., BOEING WIND TUNNEL TEST NO. 927 - HIGH SPEED FORCE TESTS TO DETERMINE SECTION CHARACTERISTICS OF VR-910M-1, FULL SCALE AIRFOIL SECTION, FOR PRODUCT IMPROVEMENT OF VERTOL DIVISIONS CH-47, The Boeing Company, Airplane Division, Boeing Report D2-24066-1, February 1966.
- (19) MODEL 727 CRUISE PERFORMANCE SUBSTANTIATION AS OF MAY 1, 1964, The Boeing Company, Commercial Airplane Group, Boeing Report D6-4781, 1965.
- (20) Hergert, F.P., WAKE SURVEY MEASUREMENTS ON THE 727 WING AND CALIBRATION OF AN IN-FLIGHT WAKE AND BOUNDARY LAYER PROBE (BTWT 1166), The Boeing Company, Commercial Airplane Group, Boeing Report D6-22318, 1969.
- (21) Purser, P.E., and M.L. Spearman, WIND-TUNNEL TESTS AT LOW SPEED OF SWEEPED AND YAWED WINGS HAVING VARIOUS PLAN FORMS, NACA TN 2445, National Advisory Committee for Aeronautics, Washington, D.C., December 1951.
- (22) Critzos, C.C., H.H. Heyson and R.W. Boswinkle, Jr., AERODYNAMIC CHARACTERISTICS OF NACA 0012 AIRFOIL SECTION AT ANGLES OF ATTACK FROM 0° TO 180°, NACA TN 3361, National Advisory Committee for Aeronautics, Washington, D.C., January 1955.
- (23) Lizak, A.A., TWO-DIMENSIONAL WIND TUNNEL TESTS OF AN H-34 MAIN ROTOR AIRFOIL SECTION, TREC TR 60-53, U.S. Army Transportation Research Command, Fort Eustis, Virginia, September 1960.
- (24) Bennett, Dr. R.L., ROTORCRAFT FLIGHT SIMULATION WITH AERO-ELASTIC ROTOR REPRESENTATION (C-81AGAJ71), Bell Helicopter Company, USAAMRDL Technical Reports 71-68A and 71-68B, U.S. Army Air Mobility Research and Development Laboratory (Eustis Directorate), Fort Eustis, Virginia, to be published.

- (25) Fisher, R.K., Jr., C.J. Bobo, J.E. Tompkins, and R.F. Child, AN EXPERIMENTAL INVESTIGATION OF THE HELICOPTER ROTOR BLADE ELEMENT AIRLOADS ON A MODEL ROTOR IN THE BLADE STALL REGIME, The Boeing Company, Vertol Division, NASA CR-114424, National Aeronautics and Space Administration, Washington, D.C., September 1971.
- (26) Dominick, F., and ITC E.E. Nelson, ENGINEERING FLIGHT TEST YUH-1H HELICOPTER PHASE D (LIMITED), USAASTA Project No. 66-04, U.S. Army Aviation Systems Test Activity, Edwards Air Force Base, California, November 1970.
- (27) Gormont, R.E., ANALYSIS OF CH-47C PERFORMANCE FLIGHT TEST, The Boeing Company, Vertol Division, Boeing Document 114-FT-712, January 1969.
- (28) Hartman, L.J., CH-47C HELICOPTER STRUCTURAL DEMONSTRATION AND POWERED LANDINGS, The Boeing Company, Vertol Division, Boeing Document 114-F-710, June 1969.

APPENDIX I
CORRELATION OF THEORY AND TWO-DIMENSIONAL
OSCILLATING AIRFOIL TEST DATA

Appendix I contains a detailed correlation of available oscillating airfoil test data and the theory developed in this report. The test data were extracted from References 6 and 7 and include forced pitch oscillation test data for four airfoil sections: V23010-1.58, NACA 0012 MOD, V13006-.7, and NACA 0006. In addition some limited data are available for forced translational (heaving) oscillation of the V23010-1.58 and are included in this section.

Airfoils utilized in the correlation are typical of sections currently used for helicopter rotor applications. The V23010-1.58 and NACA 0012 type have been used as constant sections for the entire span of rotor blades as well as for inboard working sections on variable geometry configurations (e.g., tapered chord rotor blades). The V13006-.7 and NACA 0006 have been used as blade tip sections to alleviate compressibility effects. The tests of References 6 and 7 were conducted at Mach number, Reynolds number, reduced frequency and mean angles of attack which correspond to the conditions prevailing on the retreating blades of full-scale helicopters. Although the test models had chords of 8 and 6.38 inches, full-scale similarity was achieved by using a variable density test facility. Testing was conducted in an effort to compile a comprehensive set of data with which theories for dynamic stall could be developed. Normal force C_n and pitching moment C_m coefficients in two-dimensional flow were determined by integrating measured differential pressures on upper and lower surfaces of the sections. Oscillatory values of lift coefficient C_l and drag coefficient C_d are not available for the tests.

The theory in SURVEY OF UNSTEADY AERODYNAMICS METHODS (earlier in this report) has been developed for the more common used lift, moment, and drag coefficients. In order to compare theory with test C_n , the following transformation is used:

$$C_n = C_l \cos \alpha + C_d \sin \alpha \quad (78)$$

Computed and test values of C_m compare directly.

Figures 20 through 23 compare pitch oscillation test loops with predicted loops (derived using the theory presented in DESCRIPTION AND DEVELOPMENT OF SELECTED UNSTEADY AERODYNAMICS METHOD) for the four airfoils.

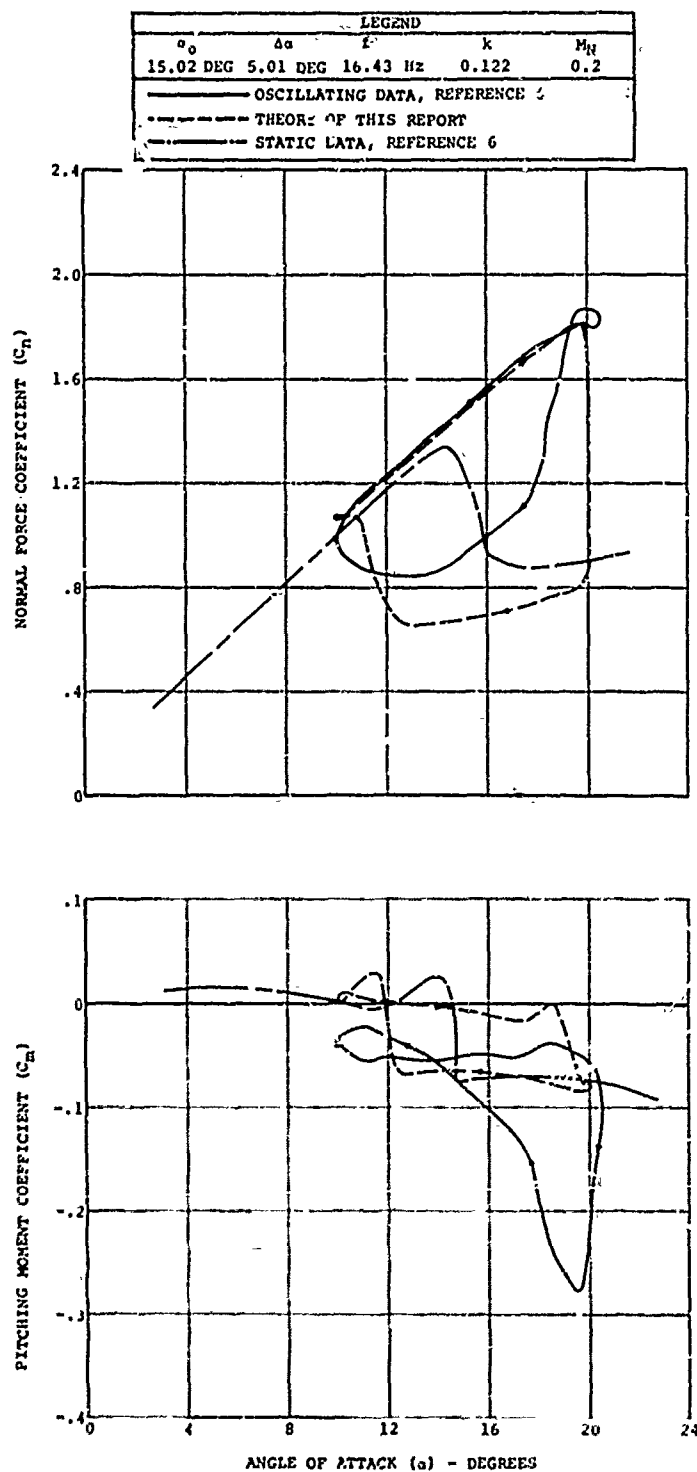


Figure 20. Dynamic Loops for the V23010-1.58 Airfoil in Forced Pitch Oscillation (Sheet 1 of 9).

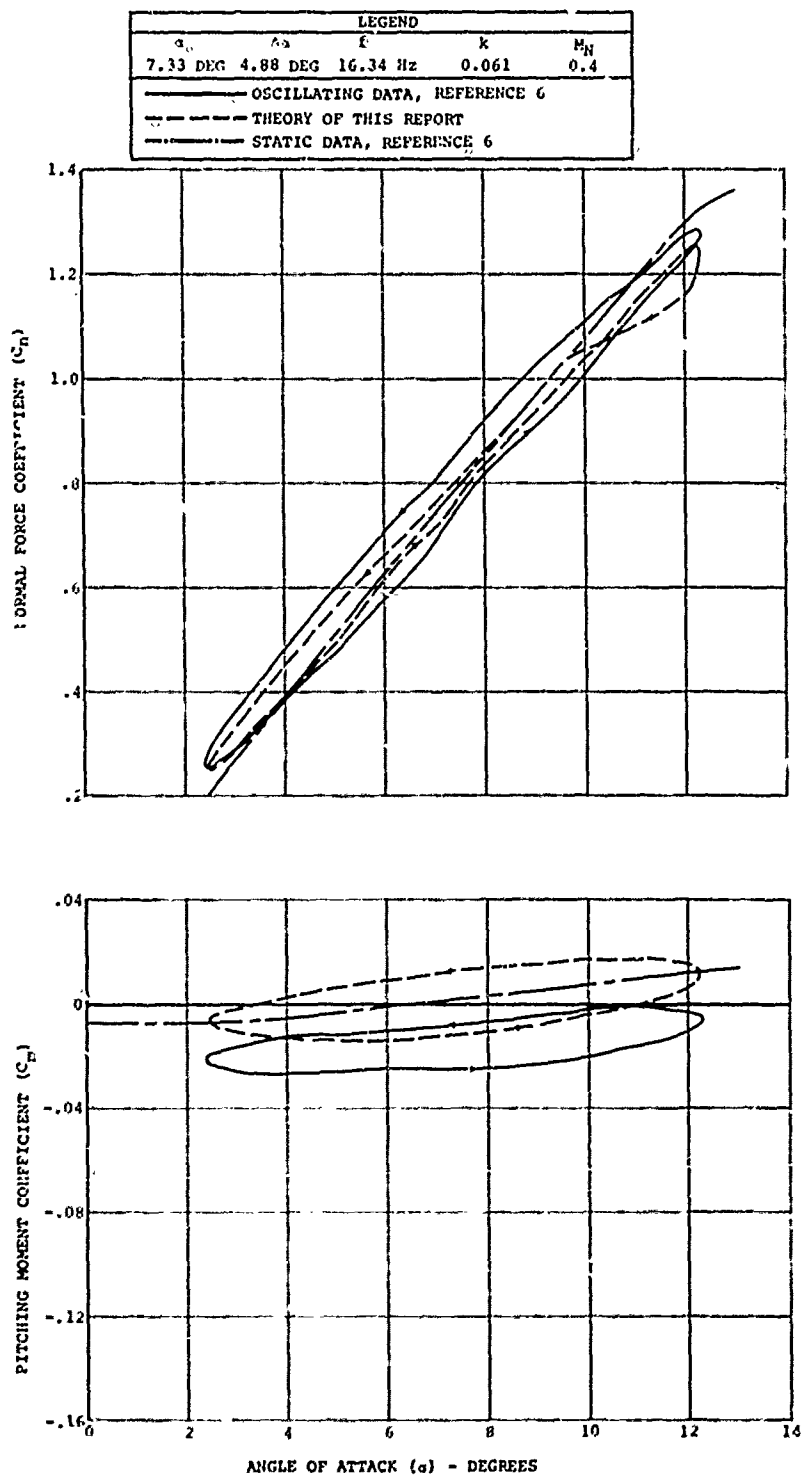


Figure 20. Continued (Sheet 2 of 9, .

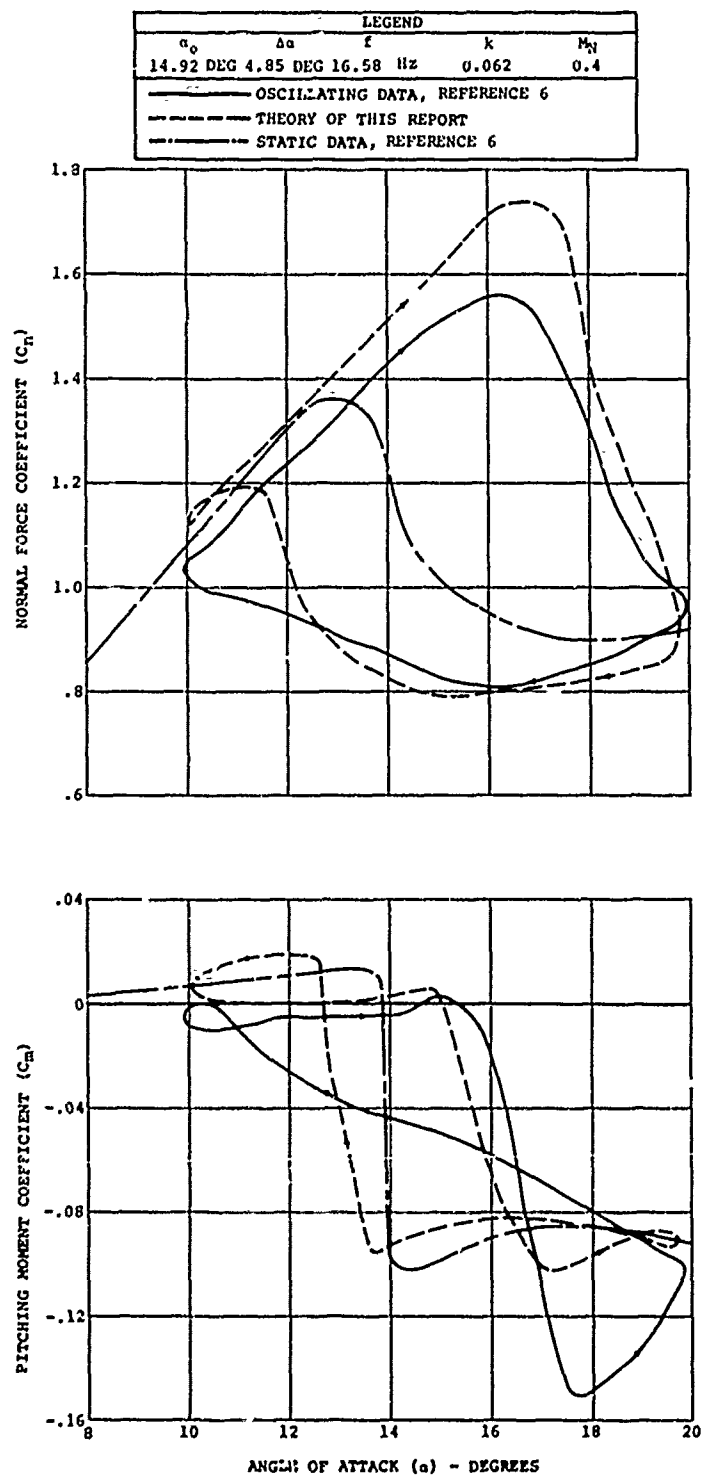


Figure 20. Continued (Sheet 3 of 9).

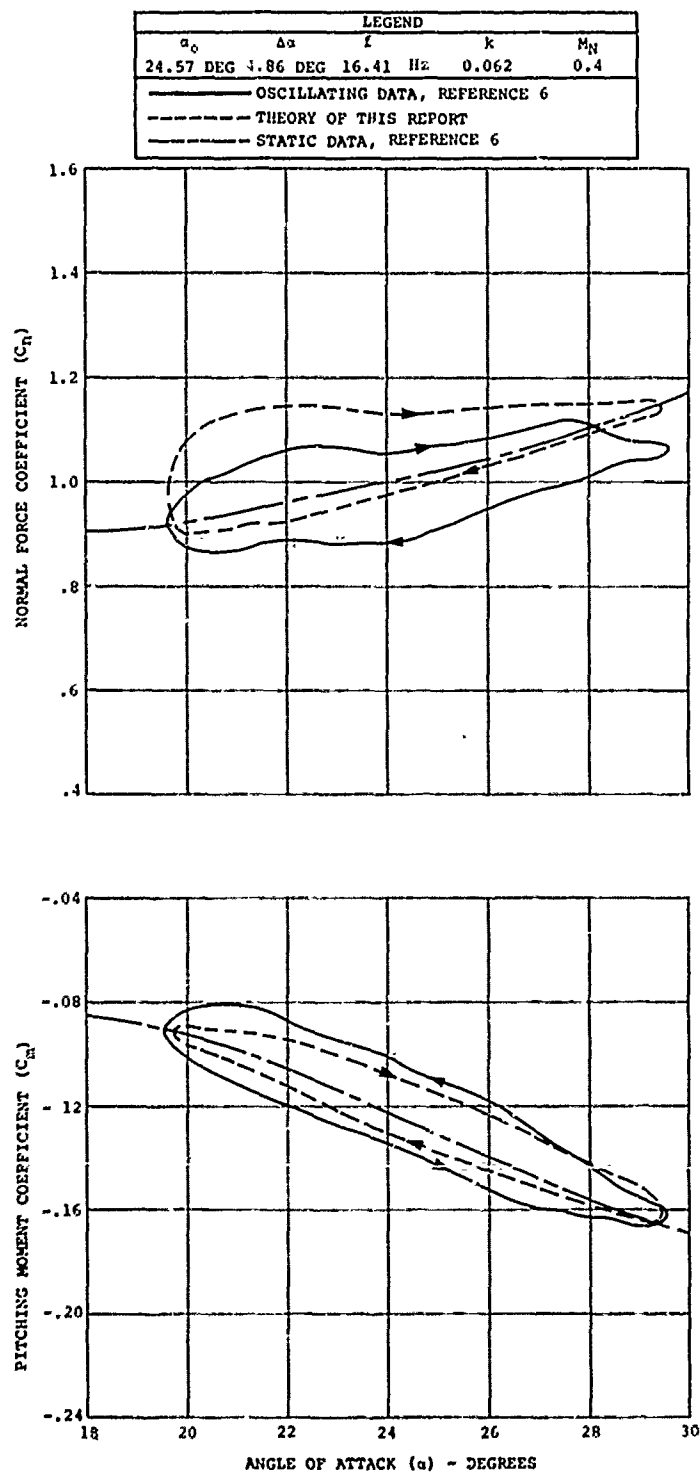


Figure 20. Continued (Sheet 4 of 9).

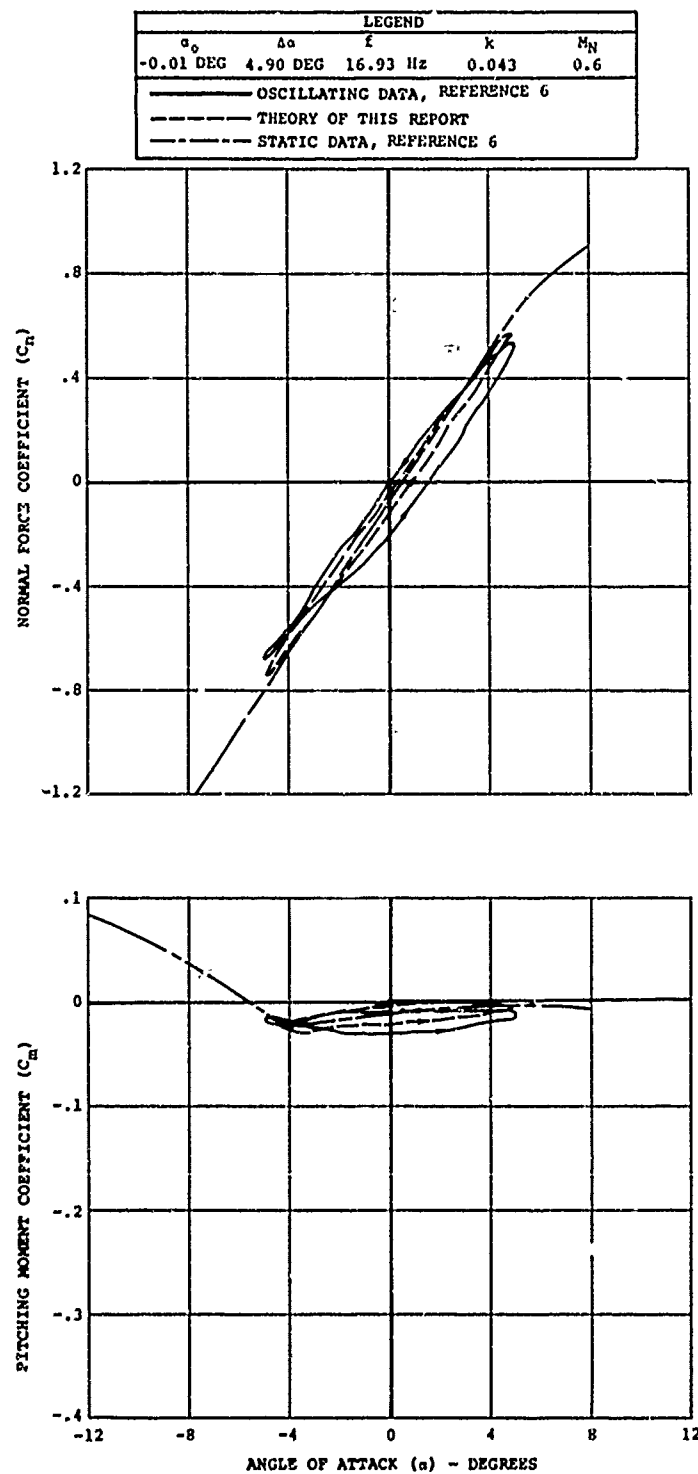


Figure 20. Continued (Sheet 5 of 9).

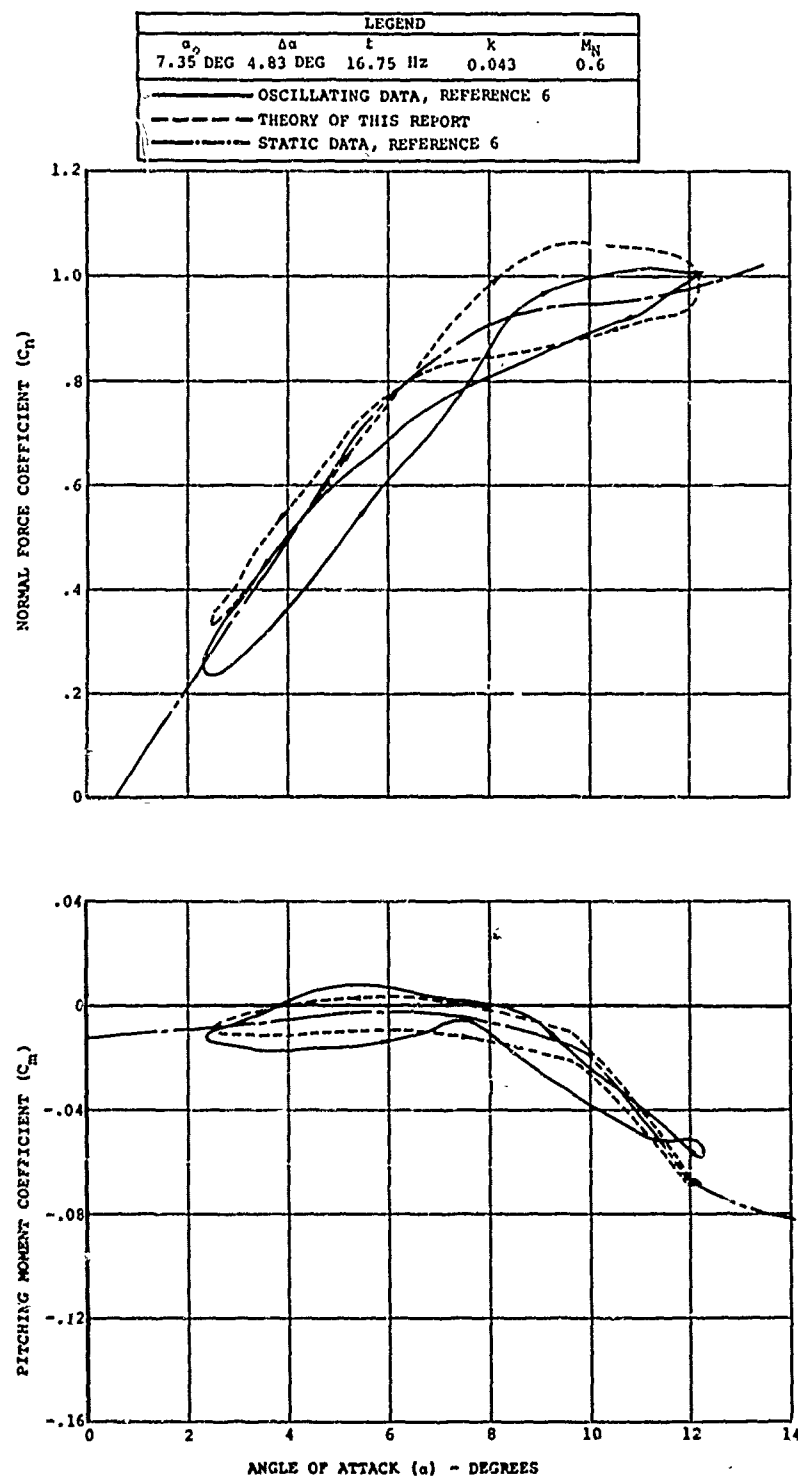


Figure 20. Continued (Sheet 6 of 9).

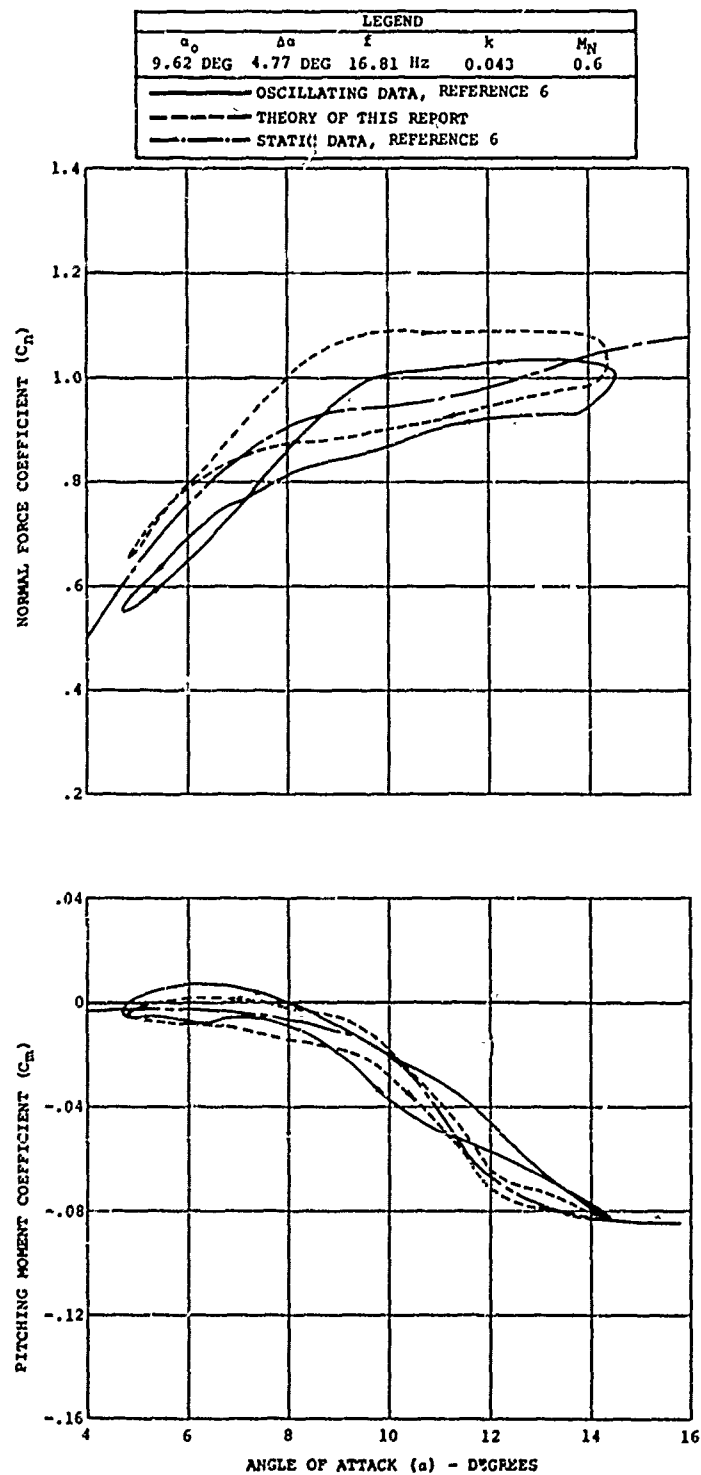


Figure 20. Continued (Sheet 7 of 9).

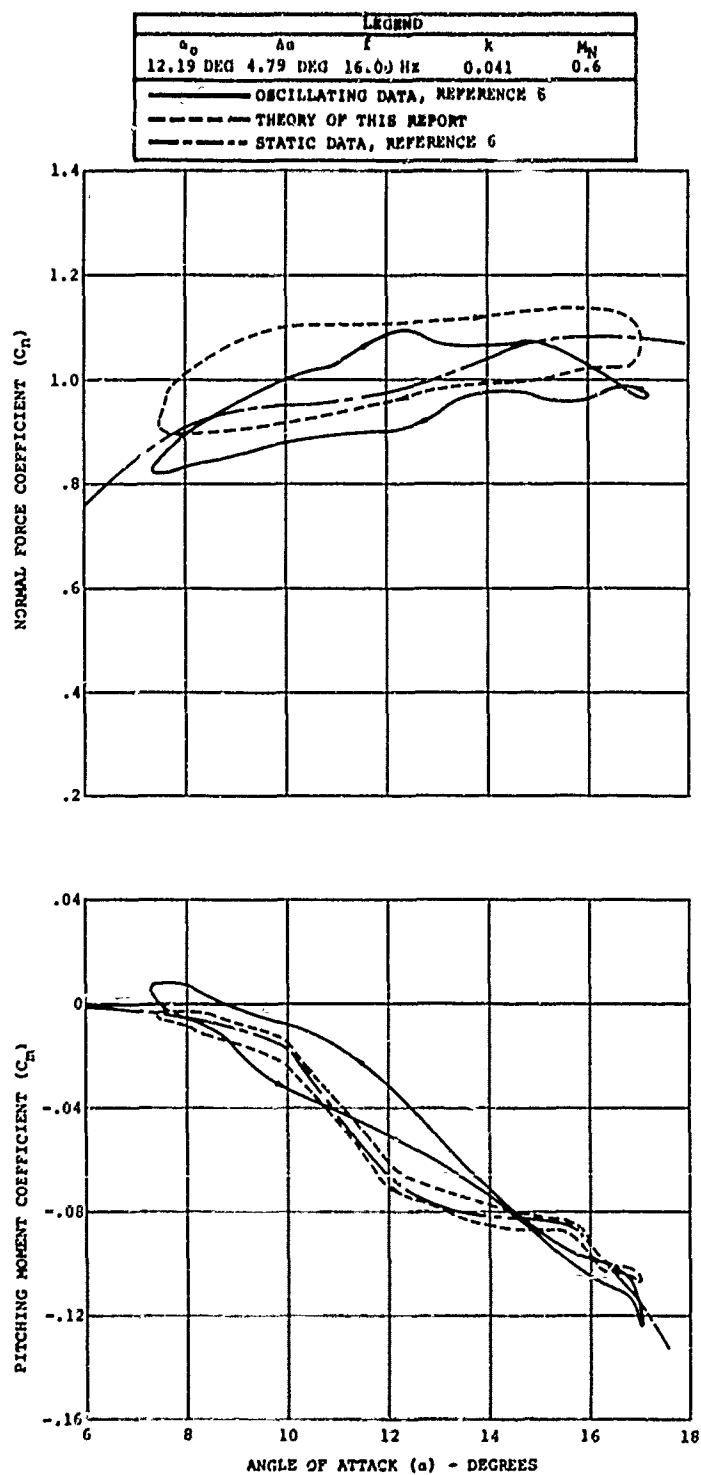


Figure 20. Continued (Sheet 8 of 9).

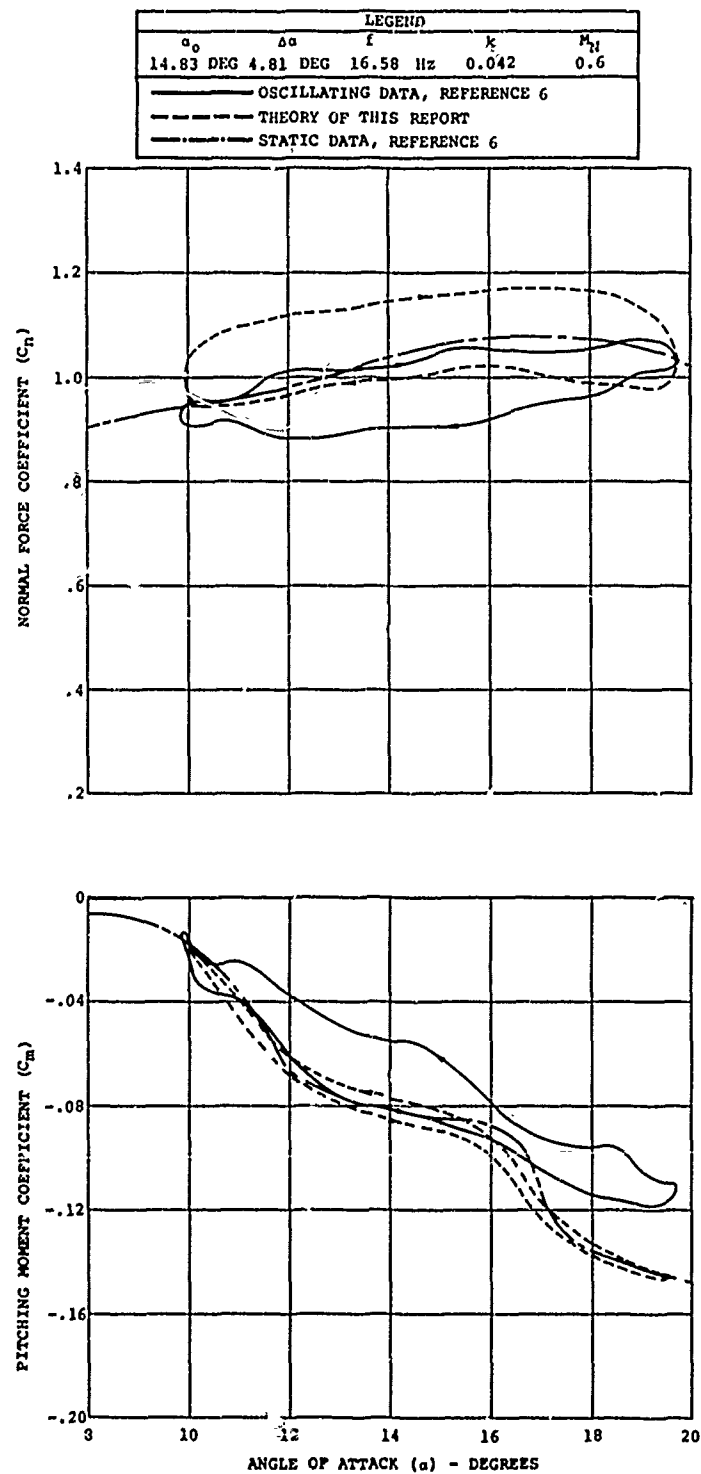


Figure 20. Continued (Sheet 9 of 9).

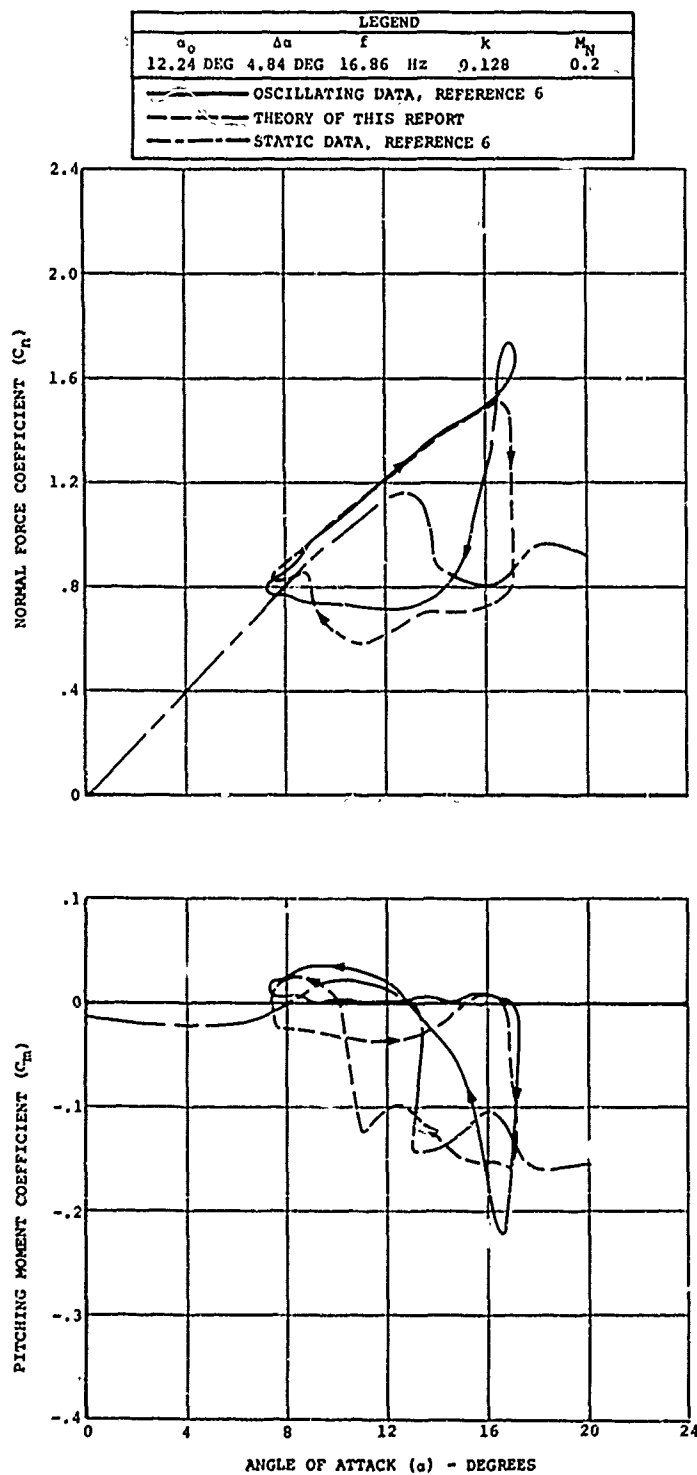


Figure 21. Dynamic Loops for the NACA 0012 MOD Airfoil in Forced Pitch Oscillation (Sheet 1 of 6).

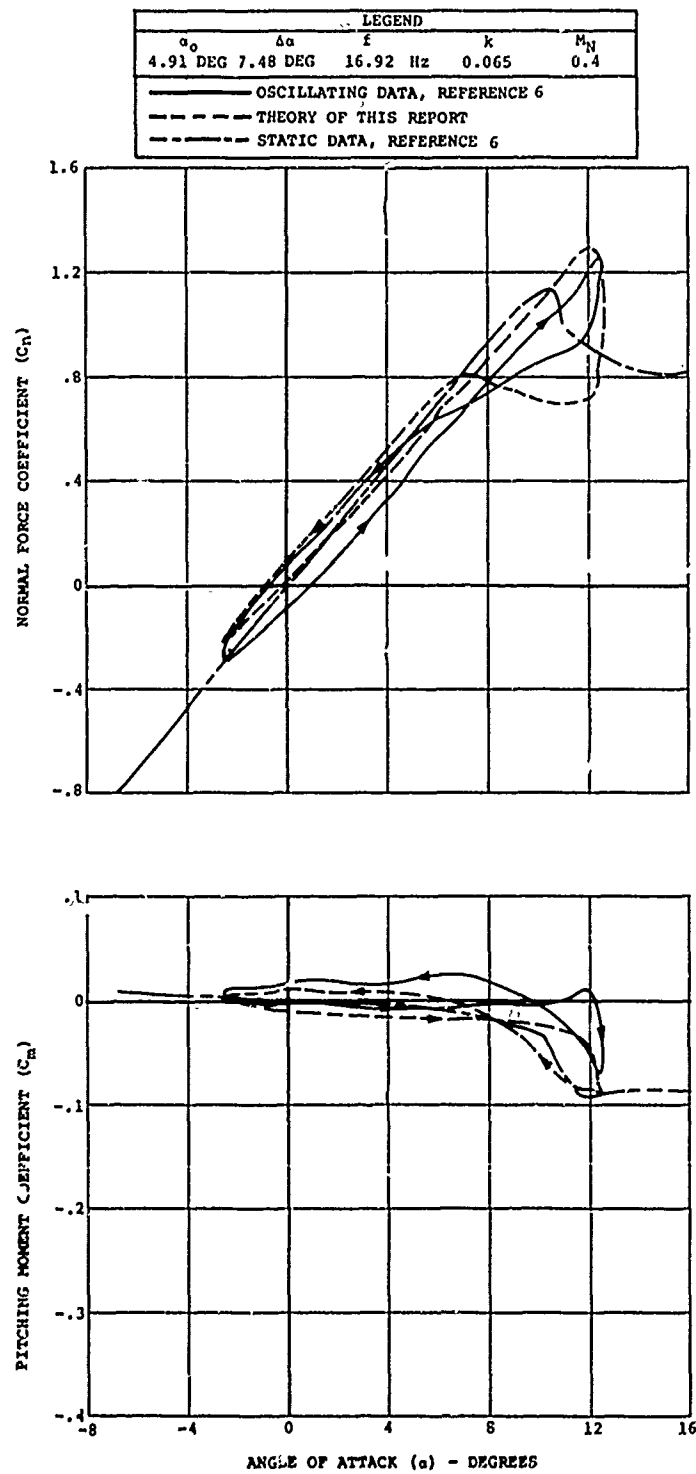


Figure 21. Continued (Sheet 2 of 6).

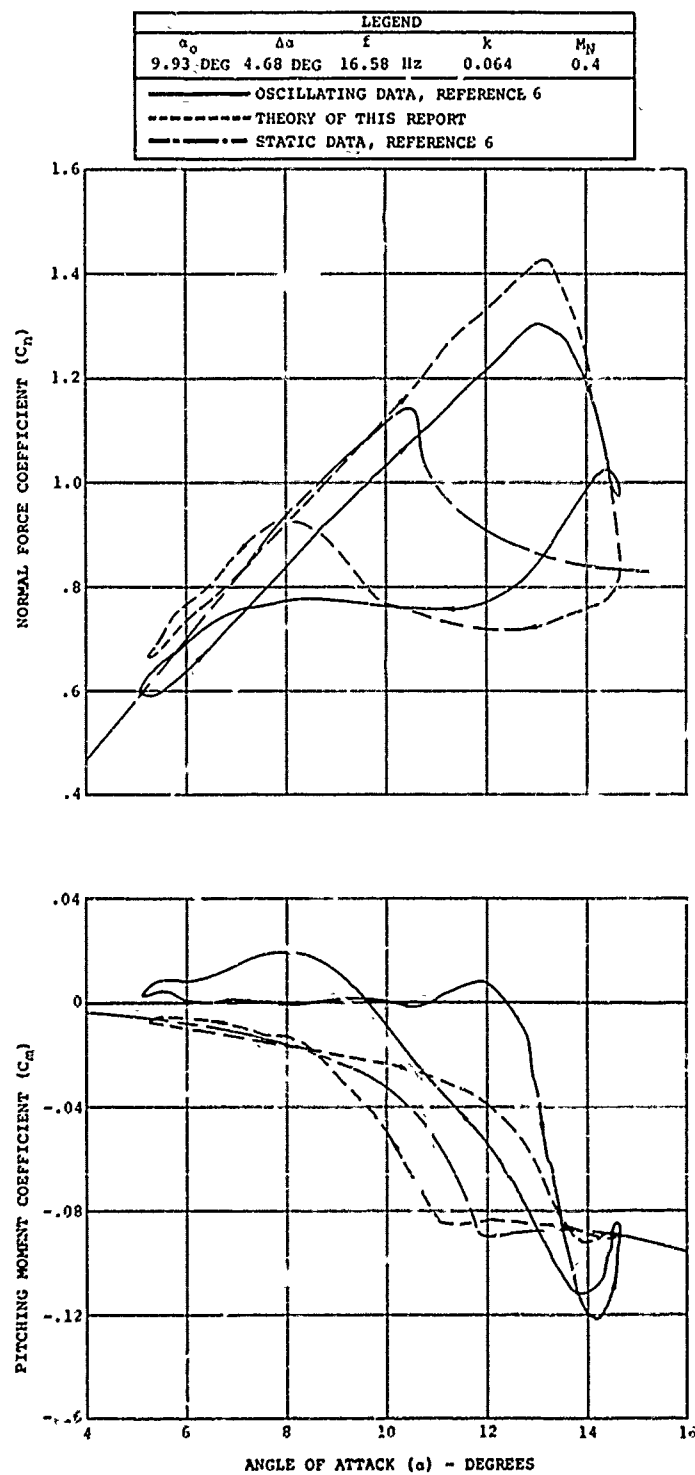


Figure 21. Continued (Sheet 3 of 6).

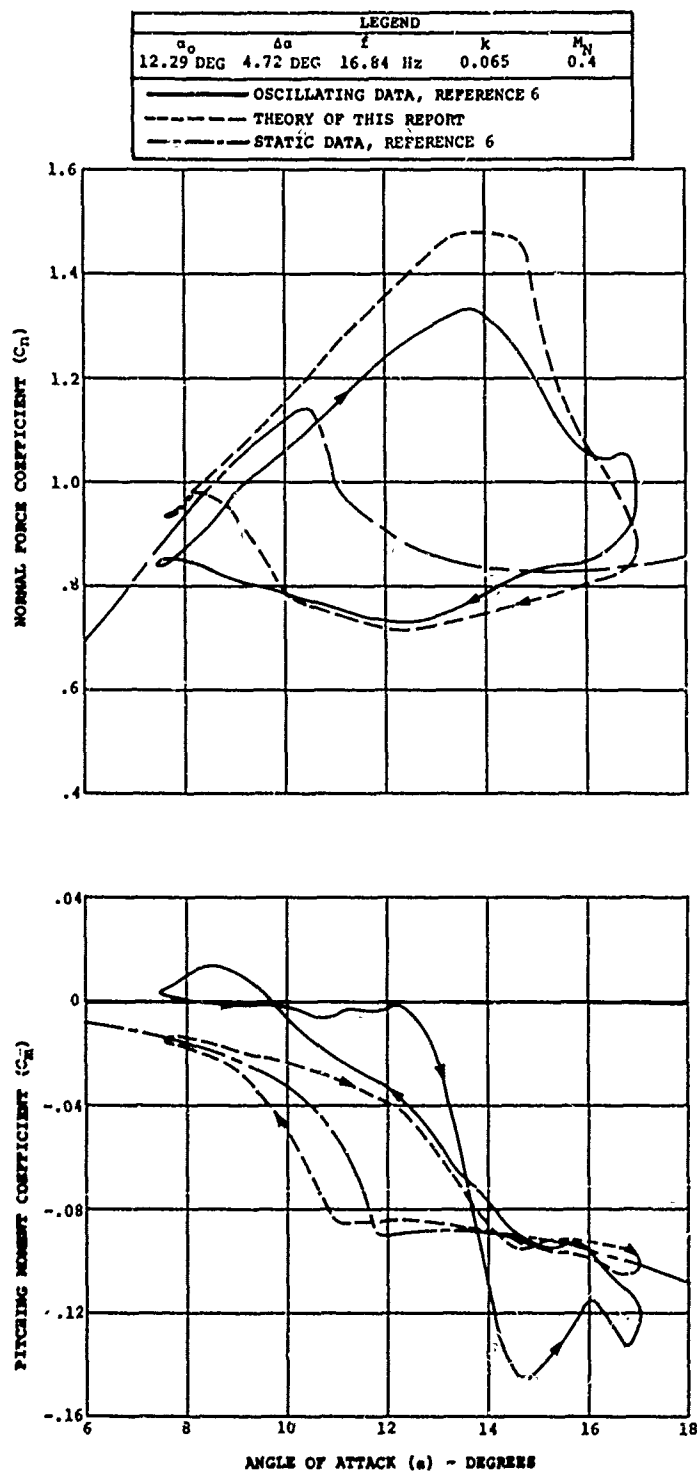


Figure 21. Continued (Sheet 4 of 6).

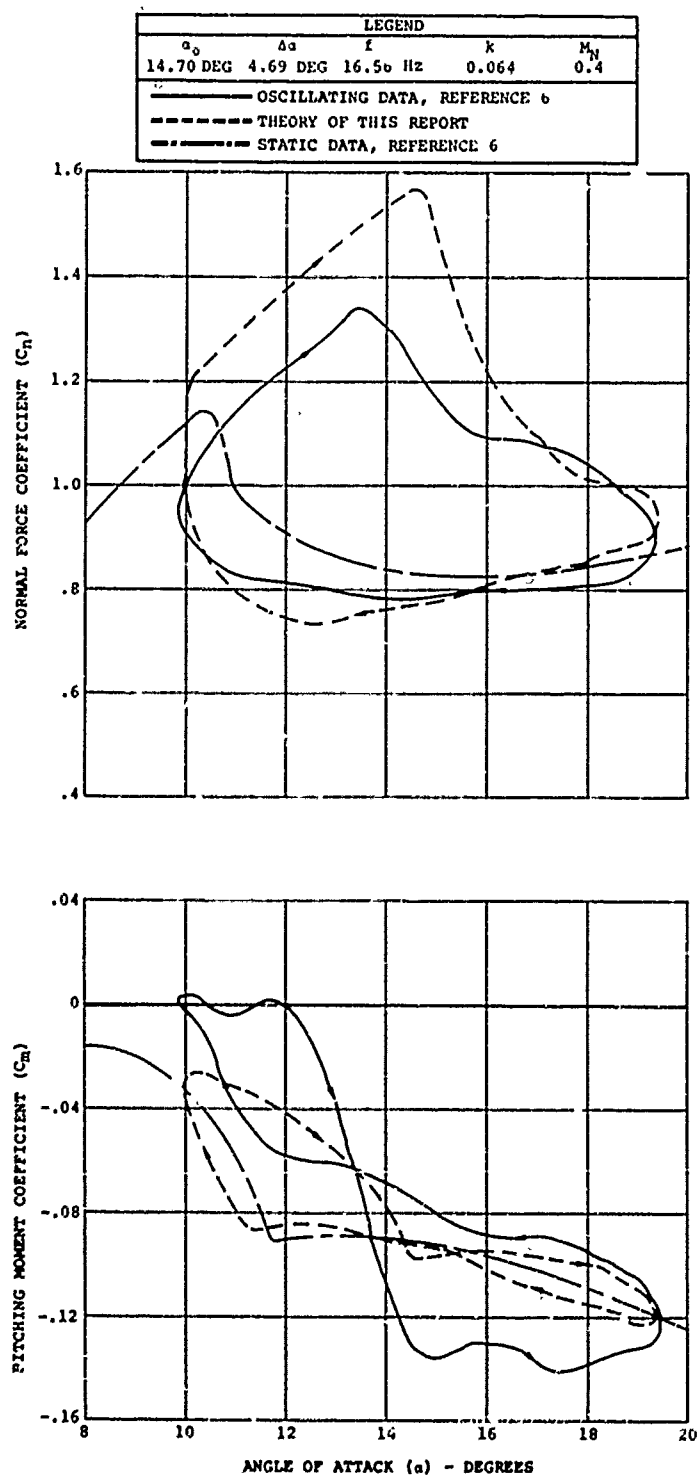


Figure 21. Continued (Sheet 5 of 6).

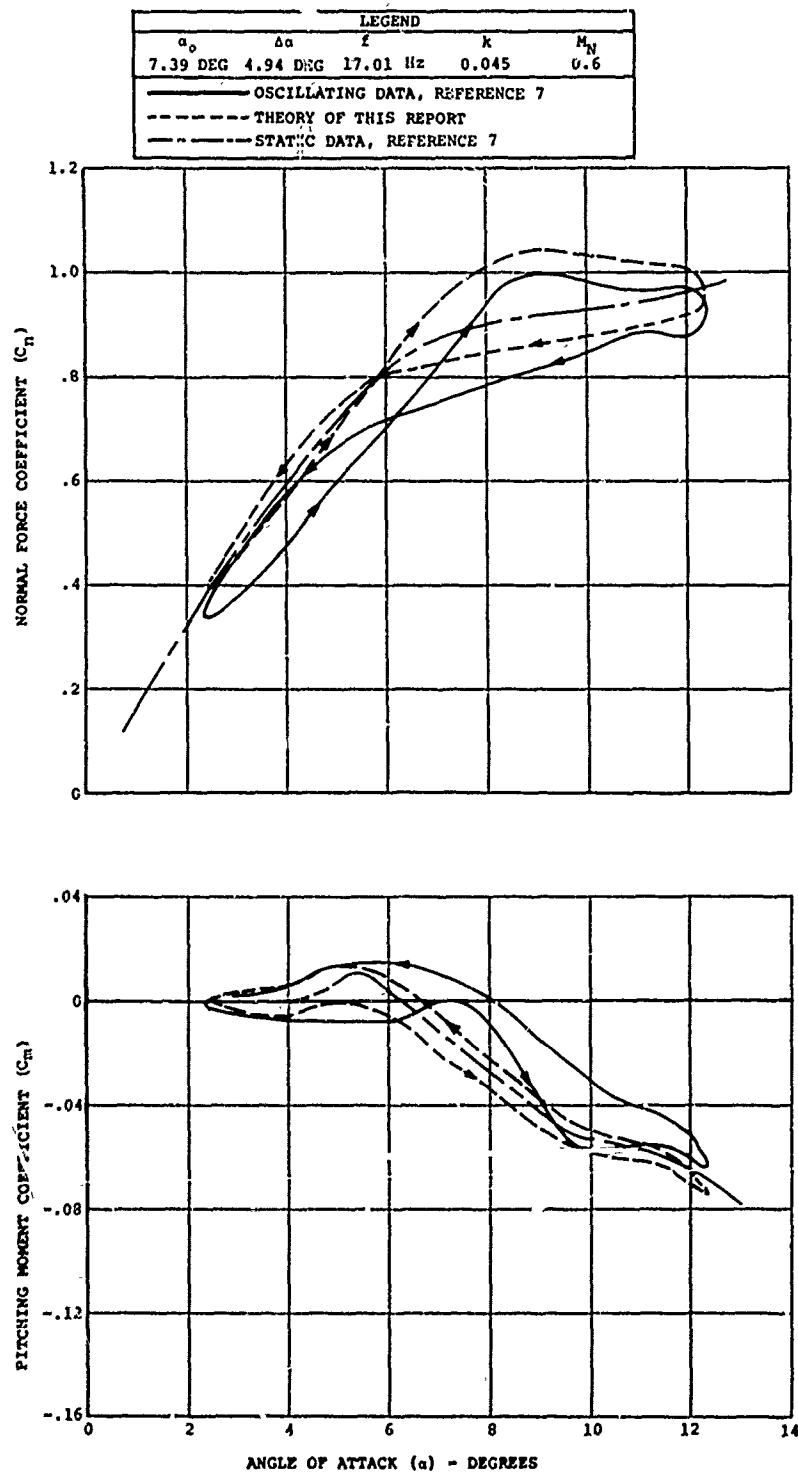


Figure 21. Continued (Sheet 6 of 6).

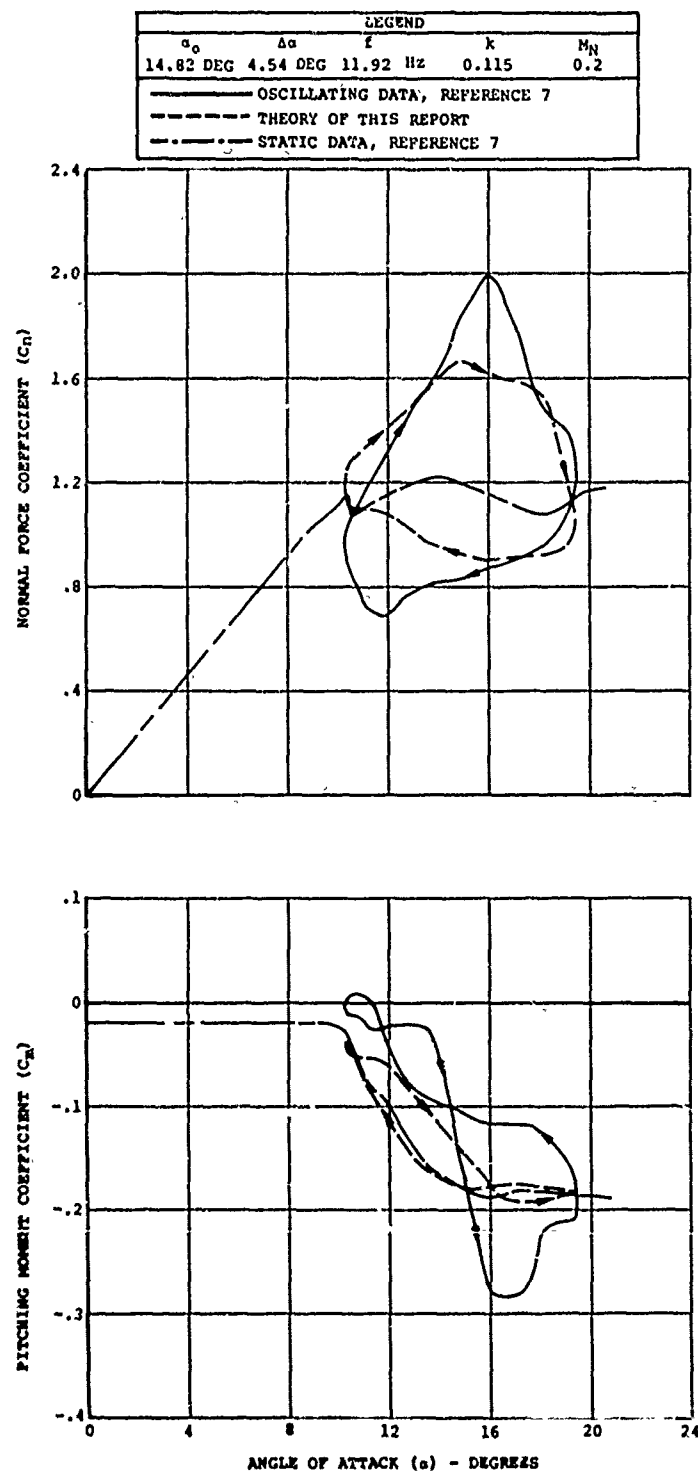


Figure 22. Dynamic Loops for the V13006-.7 Airfoil in Forced Pitch Oscillation (Sheet 1 of 5).

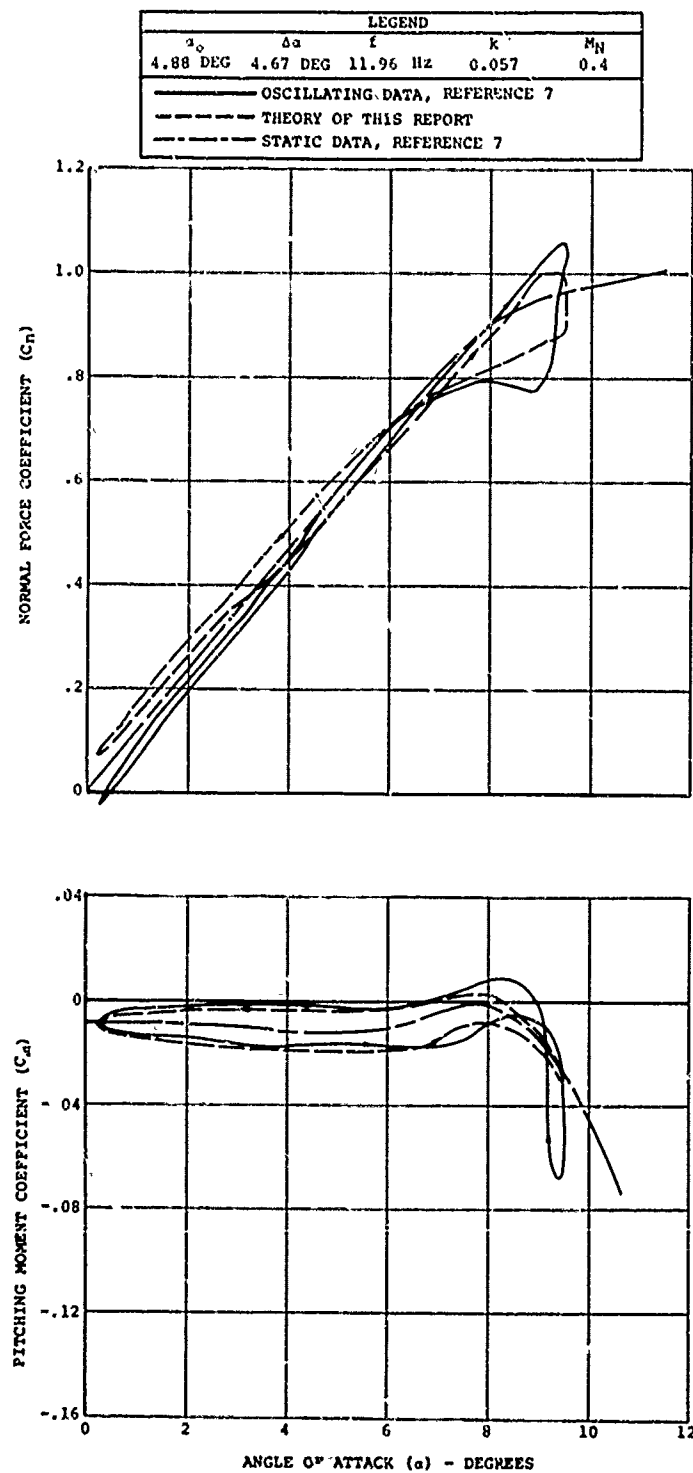


Figure 22. Continued (Sheet 2 of 5).

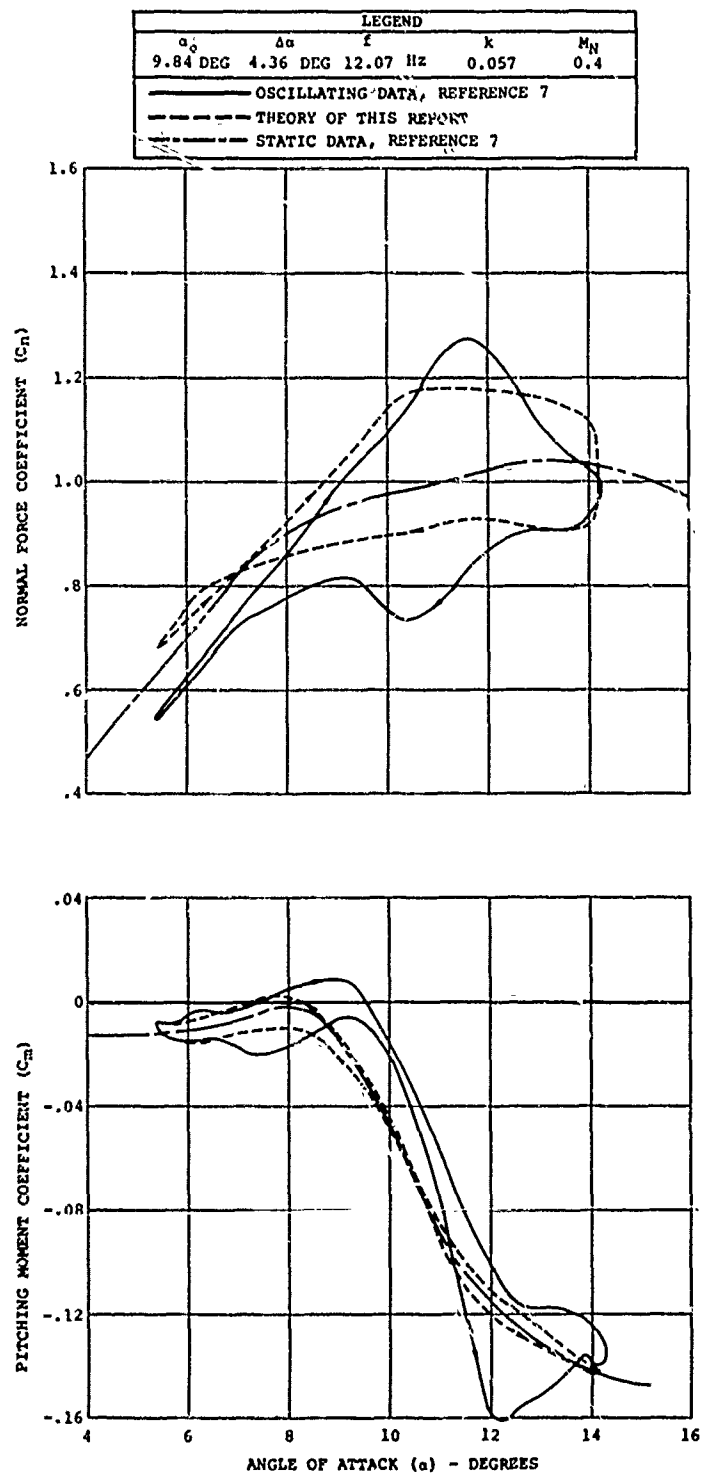


Figure 22. Continued (Sheet 3 of 5).

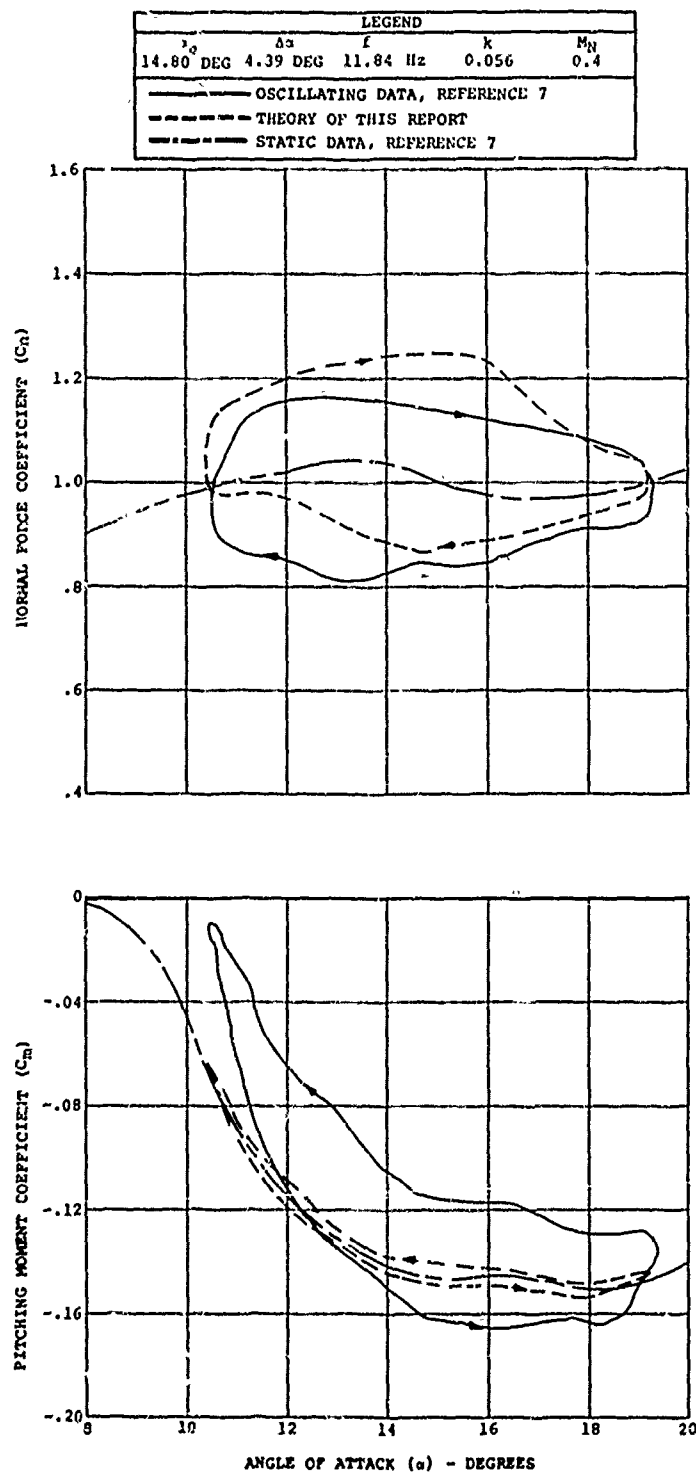


Figure 22. Continued (Sheet 4 of 5).

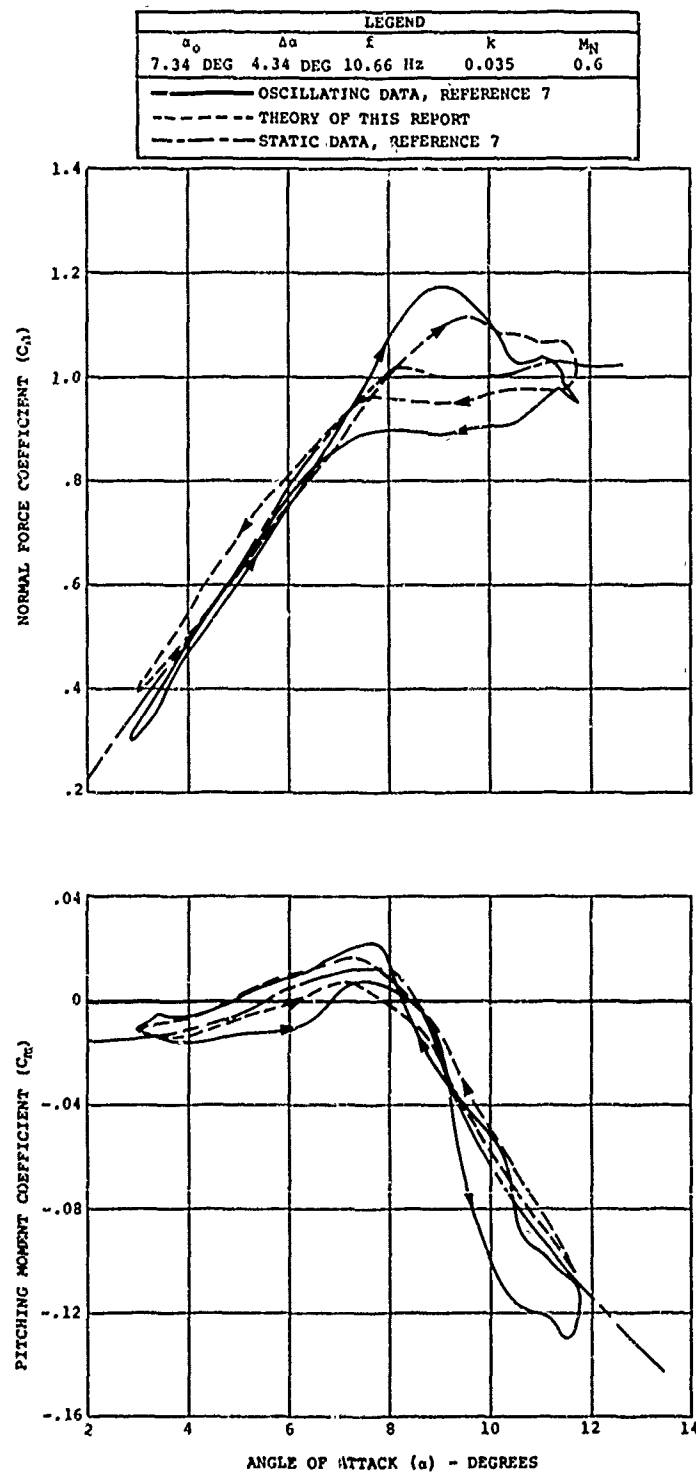


Figure 22. Continued (Sheet 5 of 5).

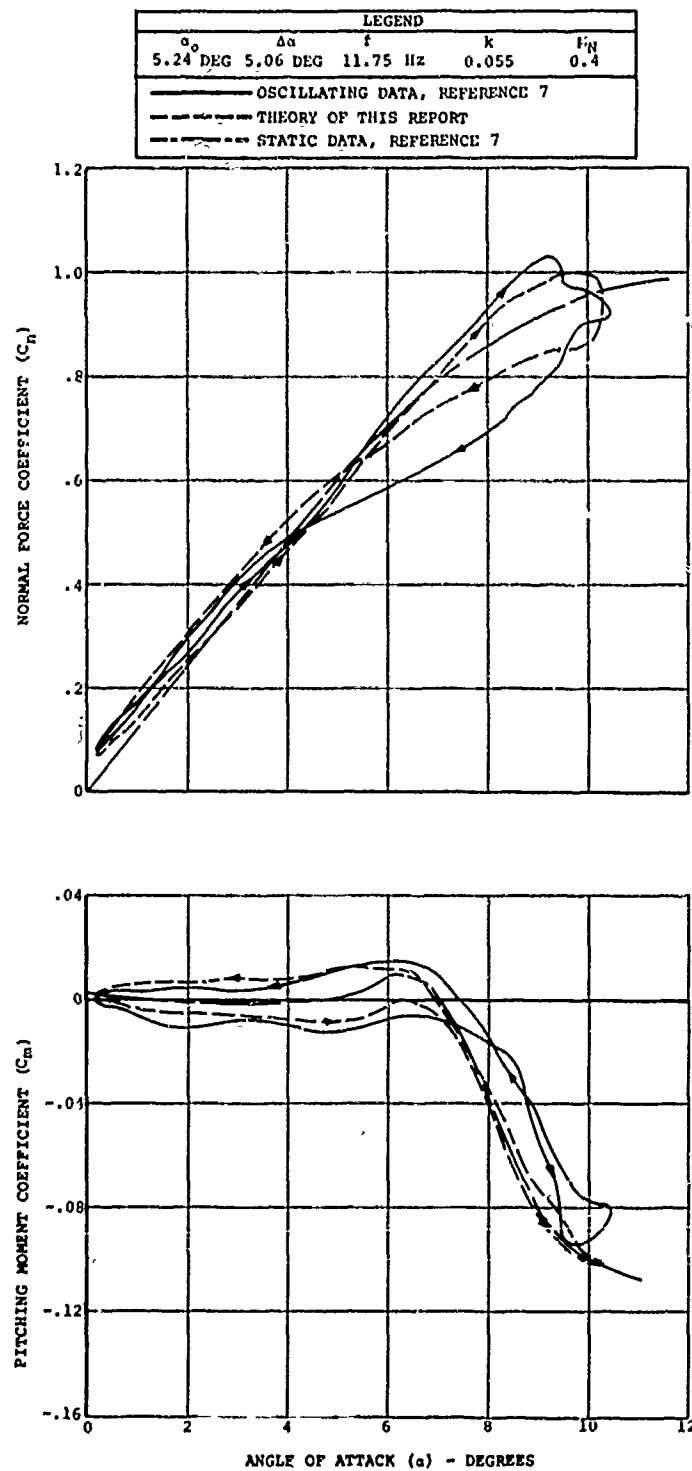


Figure 23. Dynamic Loops for the NACA 0006 Airfoil in Forced Pitch Oscillation (Sheet 1 of 6).

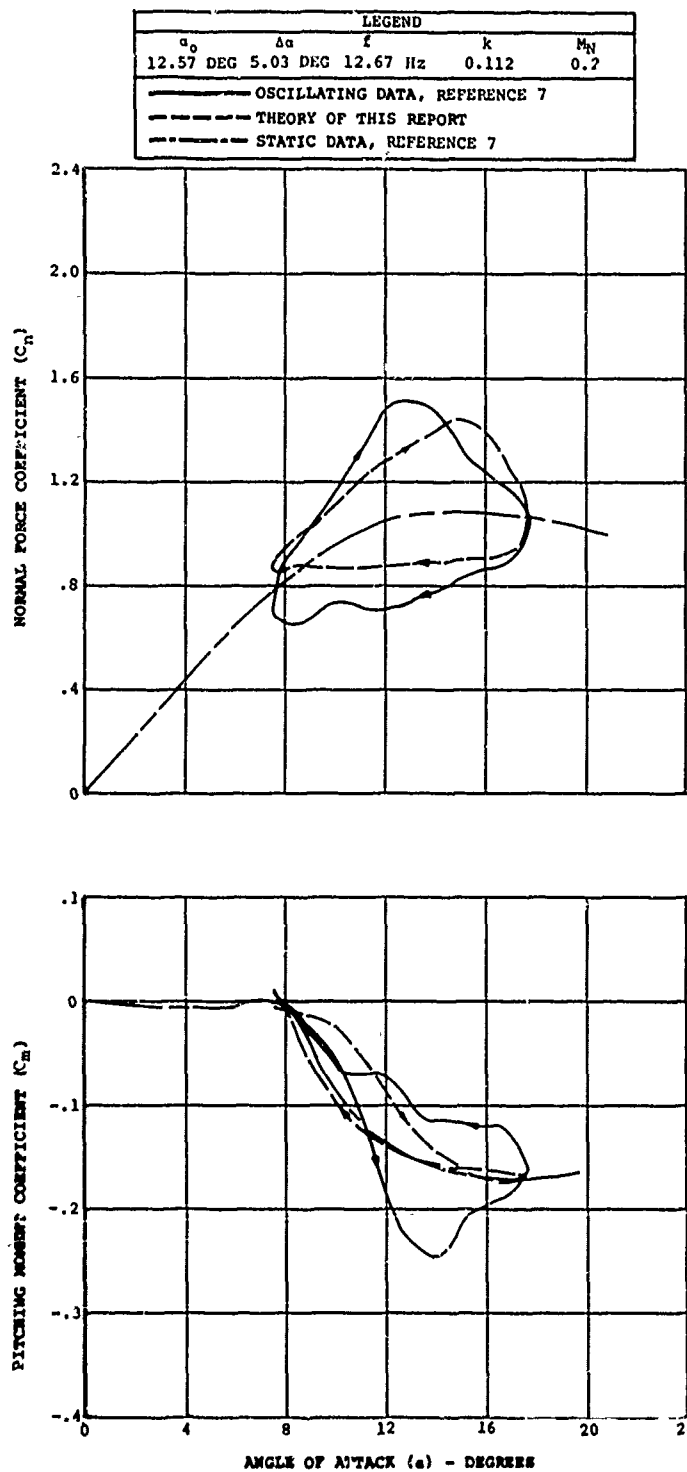


Figure 23. Continued (Sheet 2 of 6).

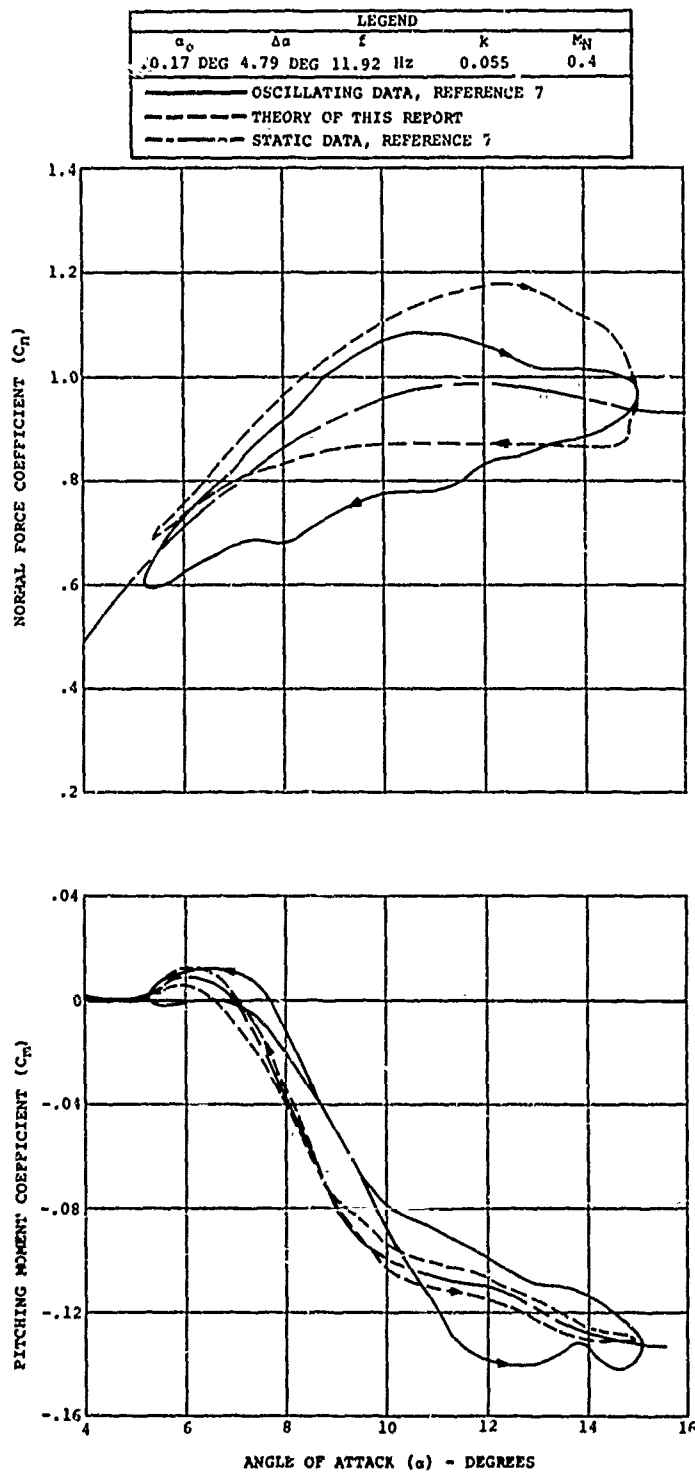


Figure 23. Continued (Sheet 3 of 6).

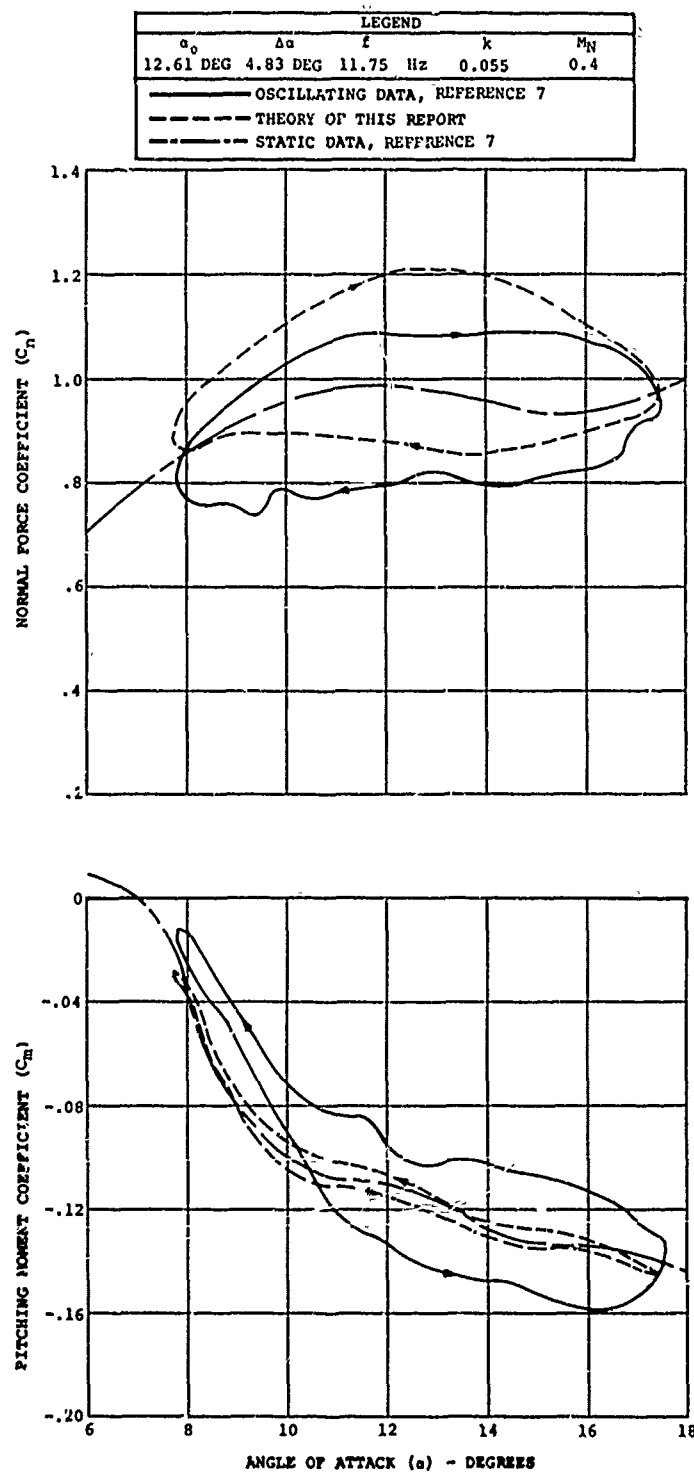


Figure 23. Continued (Sheet 4 of 6).

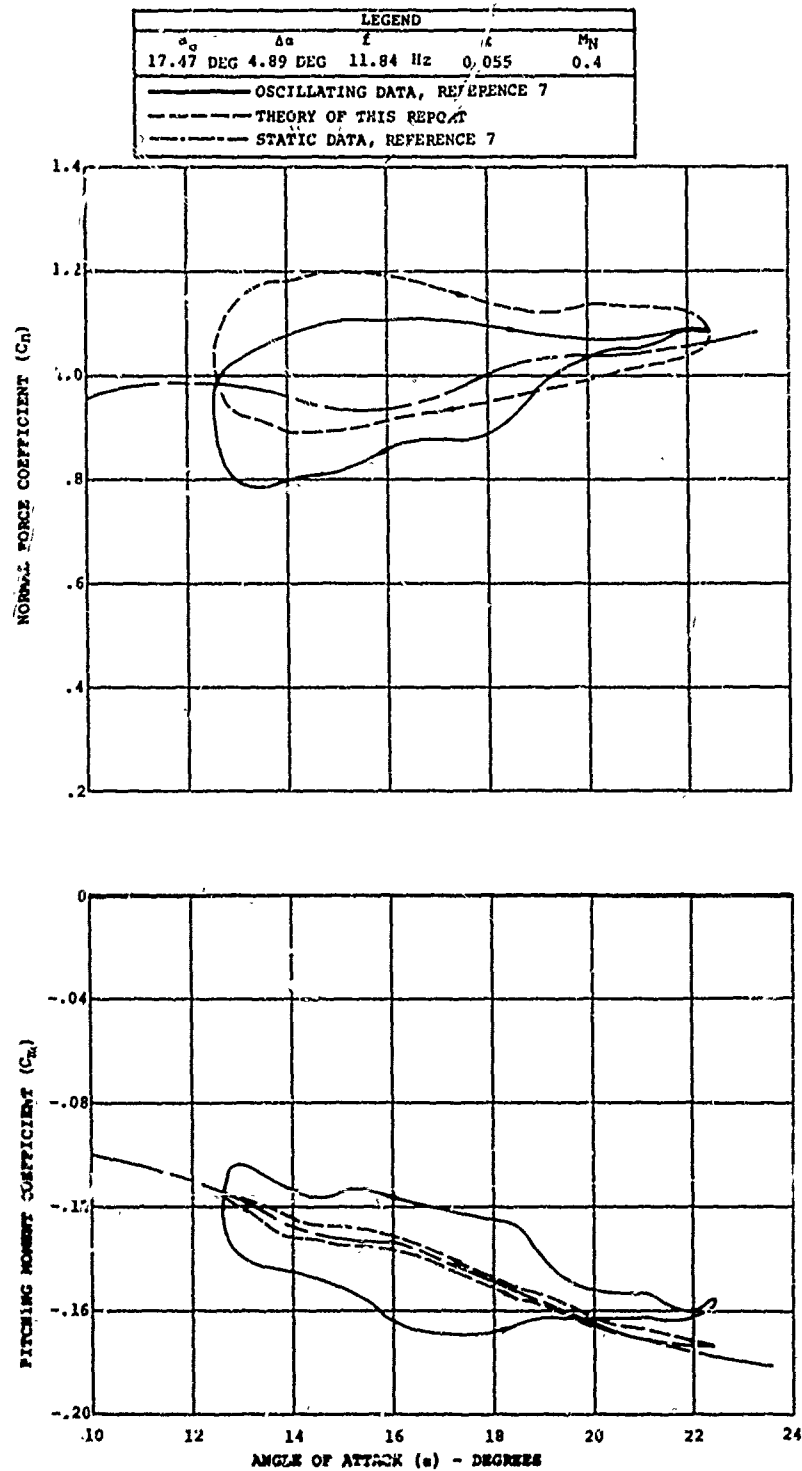


Figure 23. Continued (Sheet 5 of 6).

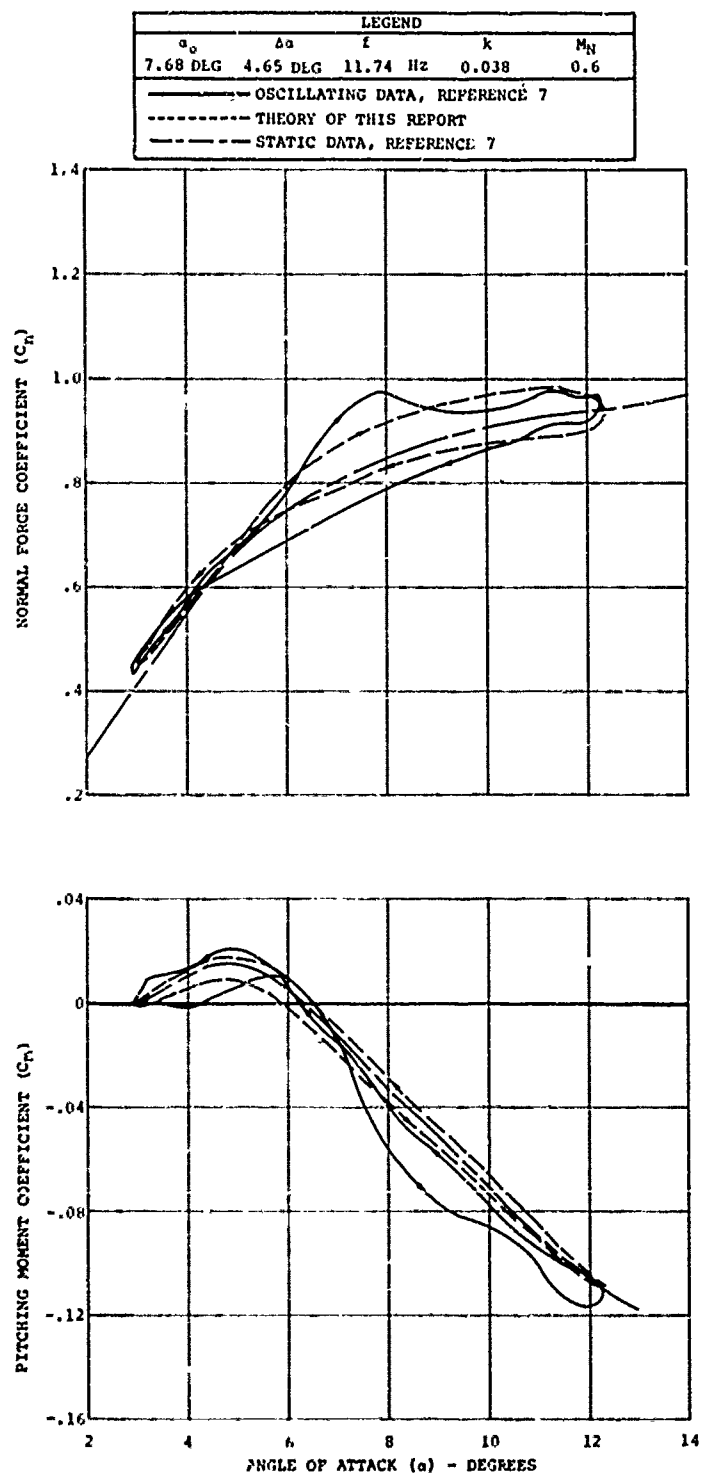


Figure 23. Continued (Sheet 6 of 6).

Dynamic data are superimposed over the static force coefficients for each particular airfoil. The identifying test conditions are:

$$\left. \begin{array}{ll} \text{Mean Pitch Angle,} & \alpha_0 \\ \text{Oscillatory Pitch Amplitude,} & \Delta\alpha \\ \text{Pitch Frequency,} & f = \frac{\omega}{2\pi} \\ \text{Reduced Frequency,} & k = \frac{c\omega}{2V} = \frac{c\pi f}{V} \\ \text{Mach Number,} & M_N = \frac{V}{V_{\text{SOUND}}} \end{array} \right\} \quad (79)$$

Pitch oscillations approximated a sinusoidal variation given by

$$\alpha = \alpha_0 + \Delta\alpha \sin \omega t \quad (80)$$

Figures 20 through 23 span a Mach number range of 0.2 to 0.6 which comprises the range tested. Mean angles of attack from below static stall to above dynamic stall are illustrated for each of the four airfoils mentioned previously at a Mach number of 0.4 and for the V23010-1.58 section at a Mach number of 0.6. For the remaining airfoils at Mach numbers of 0.2 and 0.6, a test point is included for forced pitch oscillation about static stall α which illustrates correlation at dynamic stall. The reduced frequencies are predicated on a full-scale 1/rev variation in pitch angle for a CH-47C helicopter rotor.

The overall correlation between test and theory in Figures 20 to 23 is good for normal force coefficient C_n and acceptable for pitching moment coefficient C_m . Key points of comparison are the $C_n - \alpha$ combinations at which C_m is a maximum with increasing α , and $C_m - \alpha$ combinations at which C_m decreases rapidly with increasing α . Such conditions are indicative of dynamic lift and dynamic moment stall for the condition tested. In addition, the area enclosed within the loops is a measure of how well the theoretical and test hysteresis effects compare. For certain cases the disparity in absolute levels for theory and test loops is unexplained. The theory applies incremental adjustments to static data and generates loops about the static coefficient lines. In general, the dynamic test loops behave similarly; however, numerous test conditions have loops shifted away from static levels. The shifts appear to occur randomly with positive or negative displacement and generate no perceivable trends. Since there is no theoretical reasoning to

justify such departures, it is believed that they probably reflect test measurement inaccuracy or zero shifts in test equipment. This discrepancy has been noted by other investigators. 1, 3, 6, 7

Figure 24 illustrates the effect of increasing the pitch oscillation frequency beyond 1/rev variations. The figures reflect frequencies which correspond to 2 through 6/rev for a CH-47B helicopter rotor. Up to frequencies of 4/rev the correlation is adequate; however, gradual narrowing of the test C_n loop and increasingly large negative C_m spikes are not predicted by theory. At the higher reduced frequencies, the correlation gradually deteriorates. The 6/rev frequency corresponds closely to the first natural torsion frequency of typical rotor blades, and the above correlation indicates that when a blade is fluttering at its natural frequency with large amplitude the airloads prediction using the developed theory would be less than ideal. However, of greater significance are the 1/rev variations which dominate the rotor during normal operation and which initially excite a stall flutter condition. It is this initial excitation which is of interest since it is the rotor condition to be avoided in design and analysis. Figures 20 through 23 previously demonstrated that the developed theory gives good correlation for the dominant 1/rev pitch oscillations. This aspect is explored further in Appendix II where complete rotor configurations are correlated with the C-81 theory.

Blade spanwise bending and flapping motion produce oscillating heaving velocities which act on rotor blade elements. Figure 25 is representative test data for translational oscillation. For these figures the identifying test condition, Δh , is the oscillating translation position and is measured in semichords. The translation oscillations approximate sinusoidal variations of the type

$$h = \Delta h \sin \omega t \quad (81)$$

The theory and test data compare favorably, indicating that the theory adequately treats velocity components due to translational motion.

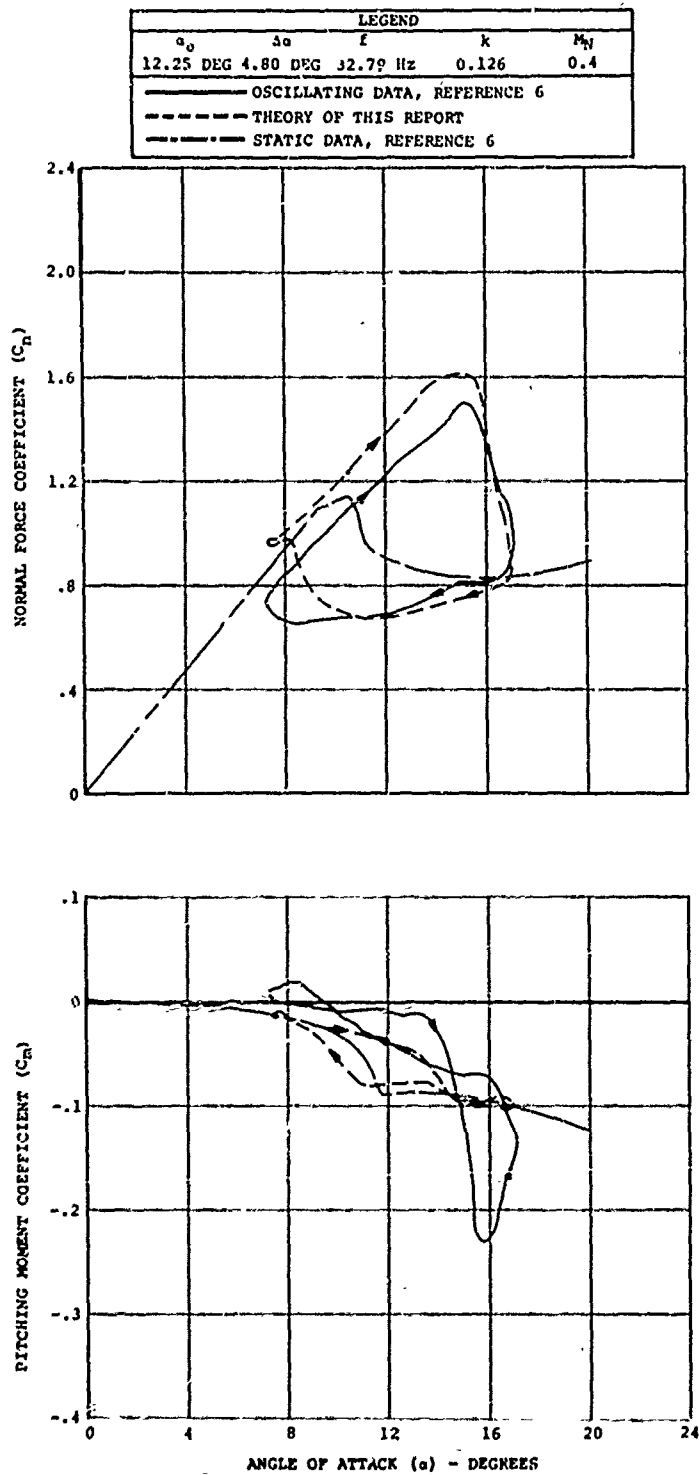


Figure 24. Dynamic Loops for the NACA 0012 MOD Airfoil in Forced Pitch Oscillation (Sheet 1 of 5).

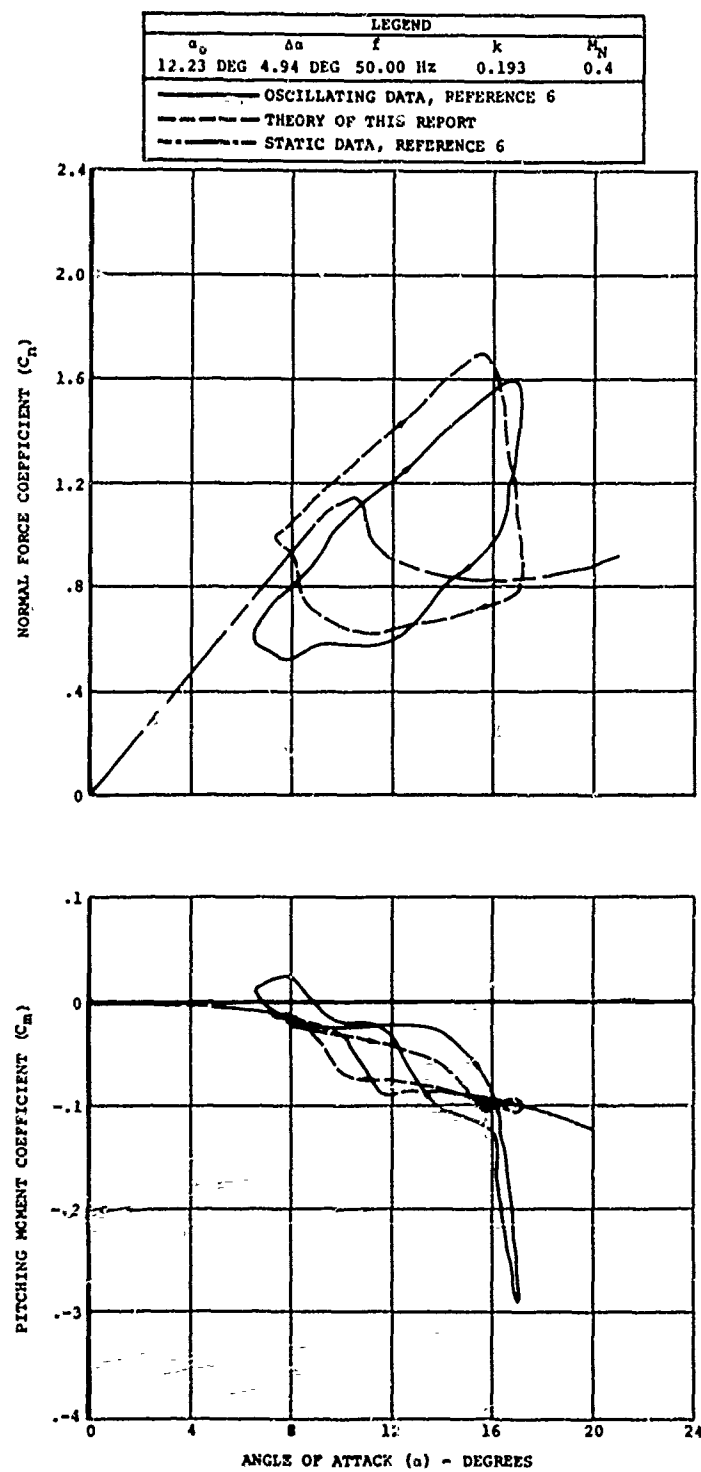


Figure 24. Continued (Sheet 2 of 5).

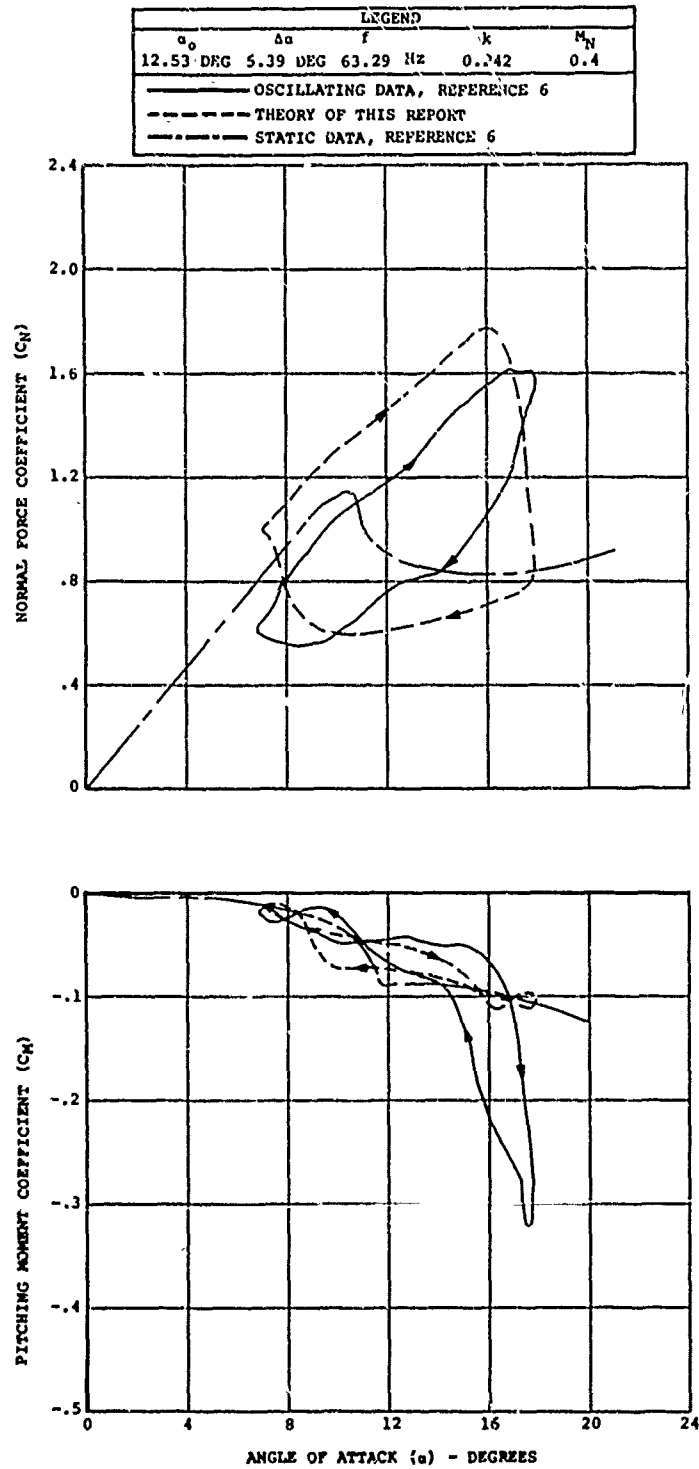


Figure 24. Continued (Sheet 3 of 5).

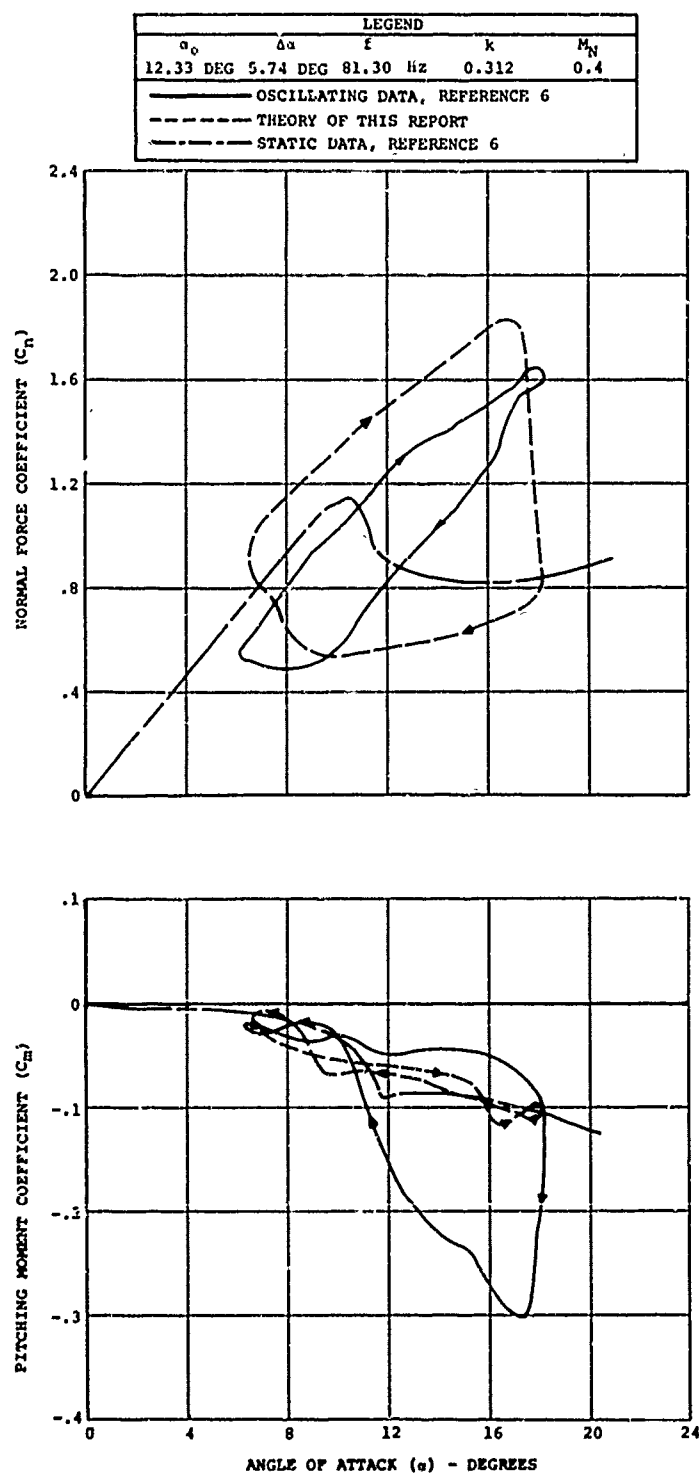


Figure 24. Continued (Sheet 4 of 5).

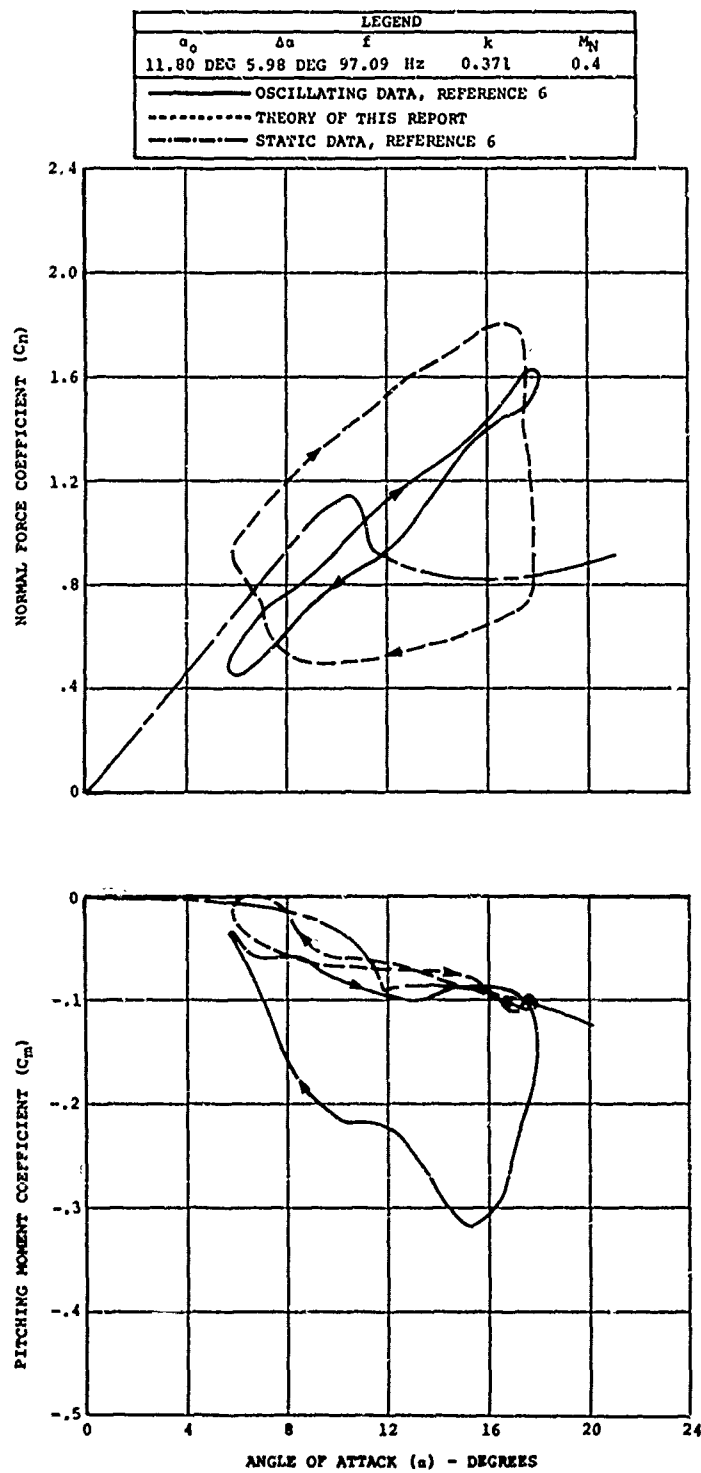


Figure 24. Continued (Sheet 5 of 5).

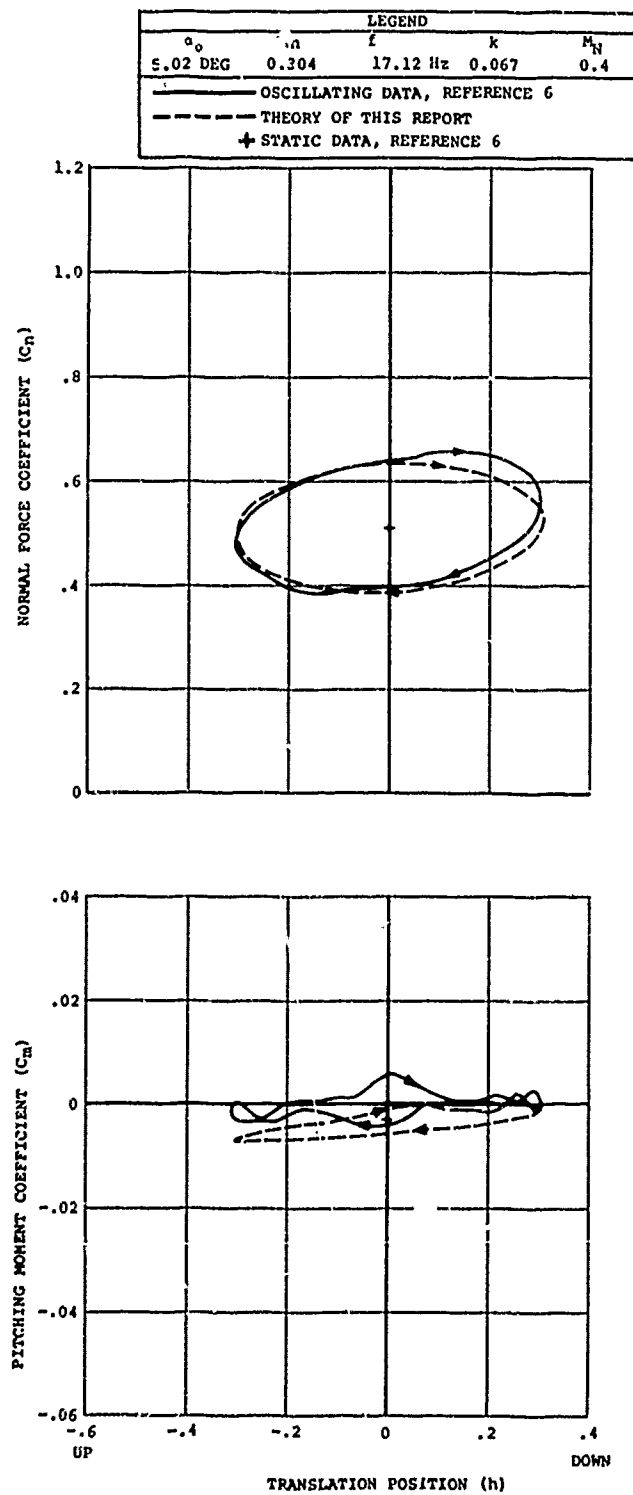


Figure 25. Dynamic Loops for the V23010-1.58 Airfoil in Translation (Sheet 1 of 4).

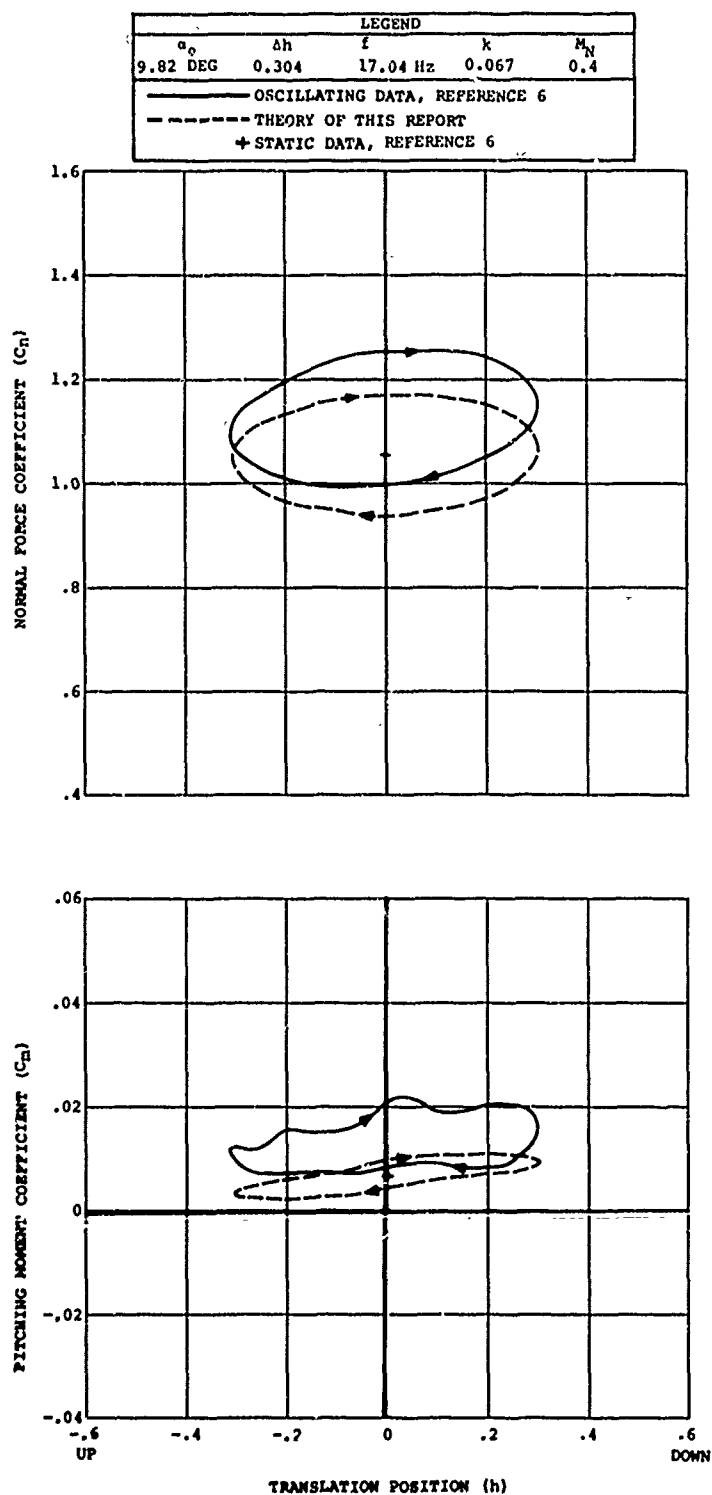


Figure 25. Continued (Sheet 2 of 4).

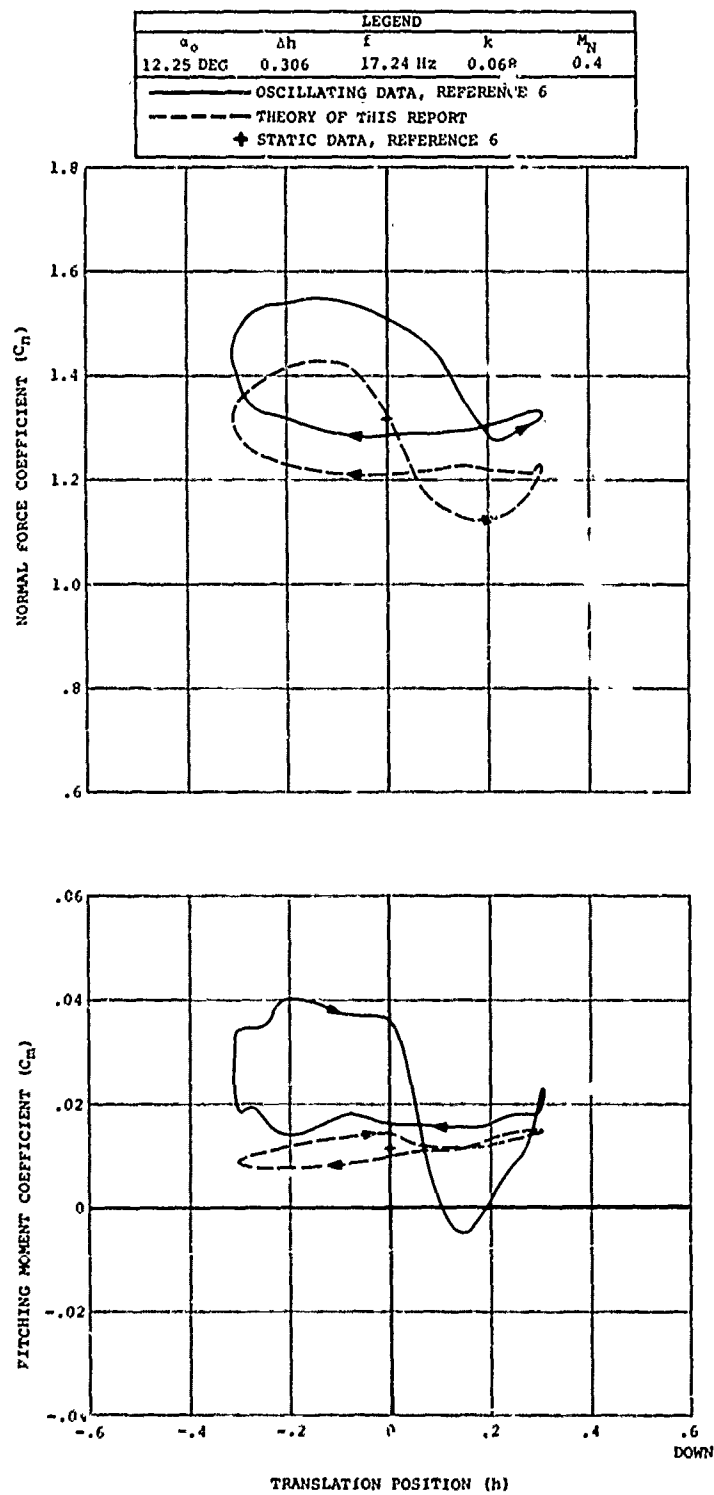


Figure 25. Continued (Sheet 3 of 4).

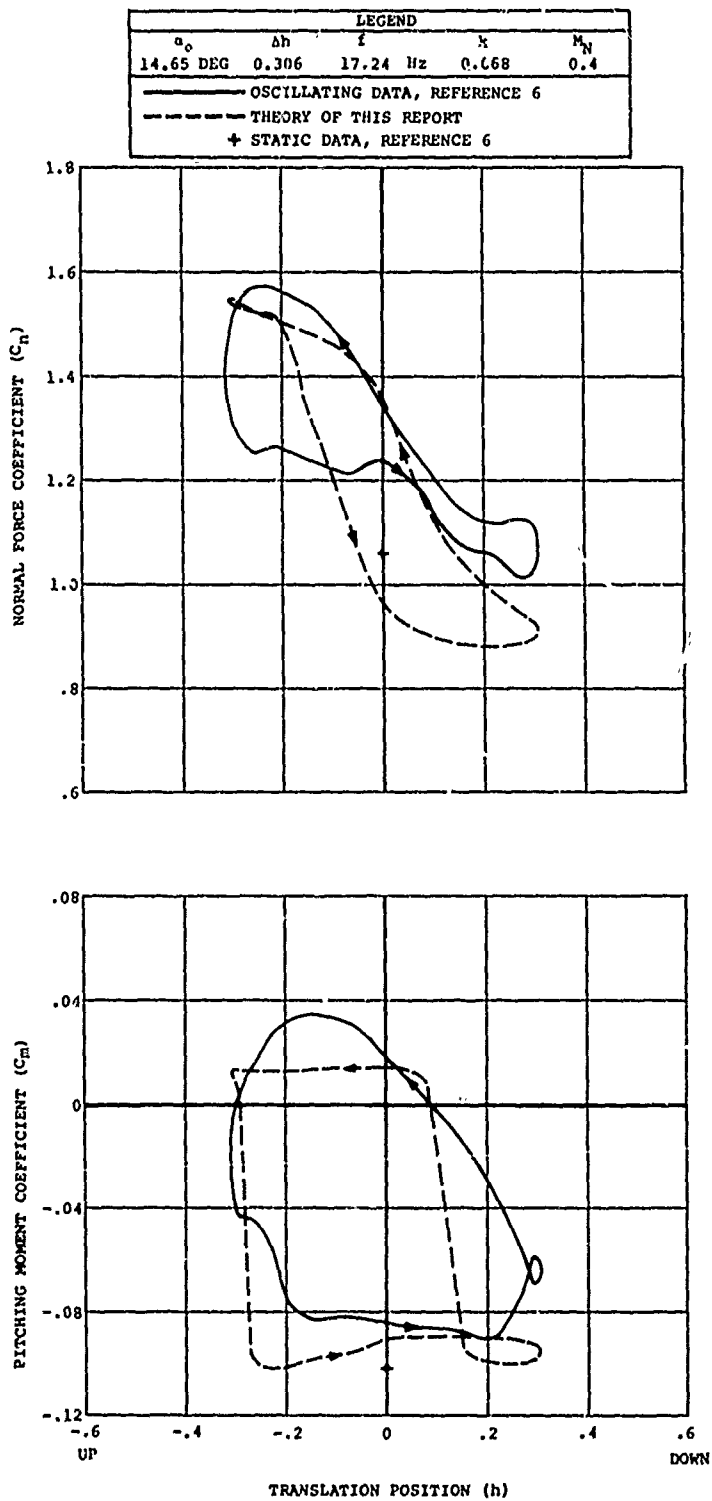


Figure 25. Continued (Sheet 4 of 4).

APPENDIX II

CORRELATION OF THEORY WITH ISOLATED ROTOR AND HELICOPTER TEST DATA

OBJECTIVE

The methods developed in this report are aimed at obtaining improved capability for predicting airfoil force coefficients, particularly at or above stall conditions. The unsteady aerodynamics and radial flow methodologies, presented herein, serve to improve the prediction of rotor force coefficients at high rotor lift levels and high forward speeds.

Rotor operation at high advance ratios produces considerable radial flow along the rotor blade span. The three-dimensional effects due to radial flow are important in relieving lift stall and in increasing skin friction drag over the airfoil sections. In addition, high rotor lift and high advance ratios necessitate high lift coefficients on the low velocity, retreating side of the rotor disk. The low velocities require retreating blades to be placed at high angles of attack well into the stall regime. Due to the dynamic nature of the stall penetration, static airfoil characteristics have been found inadequate in predicting force characteristics which are experienced by stalled rotor blades. To predict the rotor blade forces requires utilization of an unsteady aerodynamic theory such as developed in this report.

The following model and full-scale test data serve to demonstrate the degree to which the unsteady aerodynamics and yawed flow refinements improved overall rotor prediction capability of the Government's Rotorcraft Flight Simulation Program, C-81.

ISOLATED ROTOR CORRELATION

Figures 26 through 37 present correlation of the C-81 program with available test data for an 8-foot-diameter model wind tunnel rotor²⁵. The model rotor represented a 1/7.5 scale model of a CH-47C helicopter rotor. Data are shown for an advance ratio of 0.35 and an advancing tip Mach number of 0.6. The data were obtained during a rotor shaft angle variation at constant collective pitch.

Figure 26 presents thrust correlation for a shaft angle sweep at constant collective pitch. The theoretical estimates were made at a collective pitch angle which matched the test thrust levels of $C_T/\sigma = .074$ at the control axis angle of -19.8° . At low lift levels, this collective setting gives thrust predictions which are below

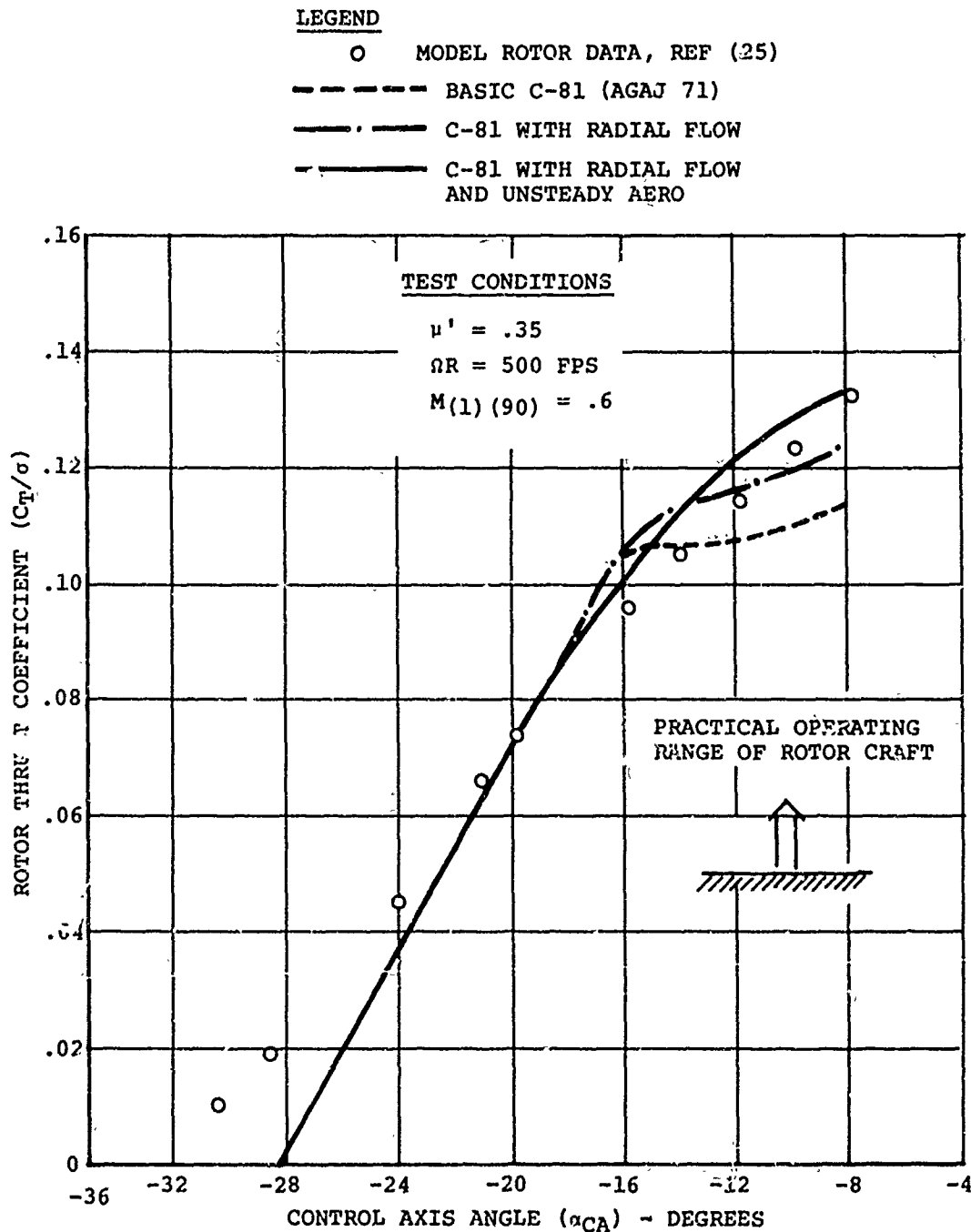


Figure 26. Model Rotor Correlation With Elastic Blade Rotor Theory: Rotor Thrust vs. Control Axis Angle.

LEGEND

- O MODEL ROTOR DATA, REF (25)
- BASIC C-81 (AGAJ 71)
- .- C-81 WITH RADIAL FLOW
- C-81 WITH RADIAL FLOW AND UNSTEADY AERO

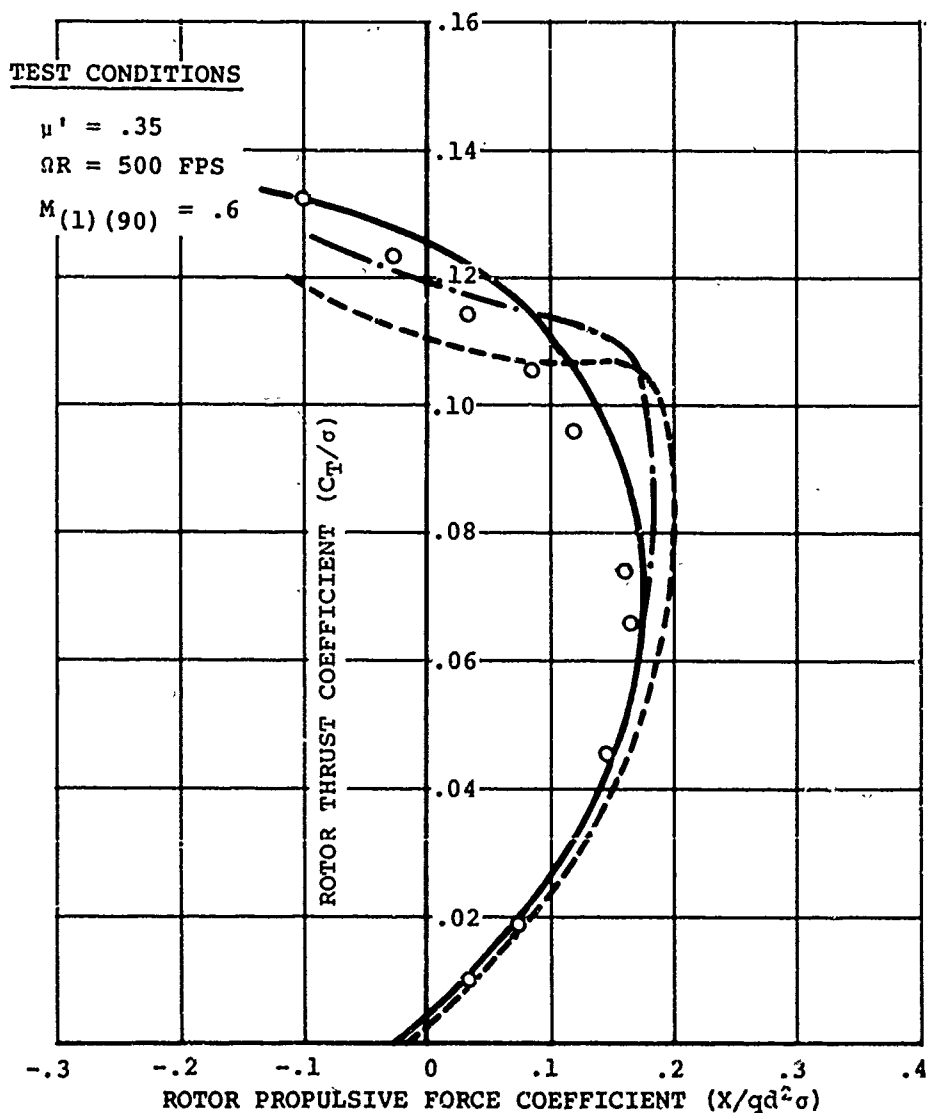


Figure 27. Model Rotor Correlation With Elastic Blade Rotor Theory: Rotor Thrust vs. Rotor Propulsive Force.

LEGEND

- MODEL ROTOR DATA, REF (25)
- BASIC C-81 (AGAJ 71)
- - - - C-81 WITH RADIAL FLOW
- C-81 WITH RADIAL FLOW
AND UNSTEADY AERO

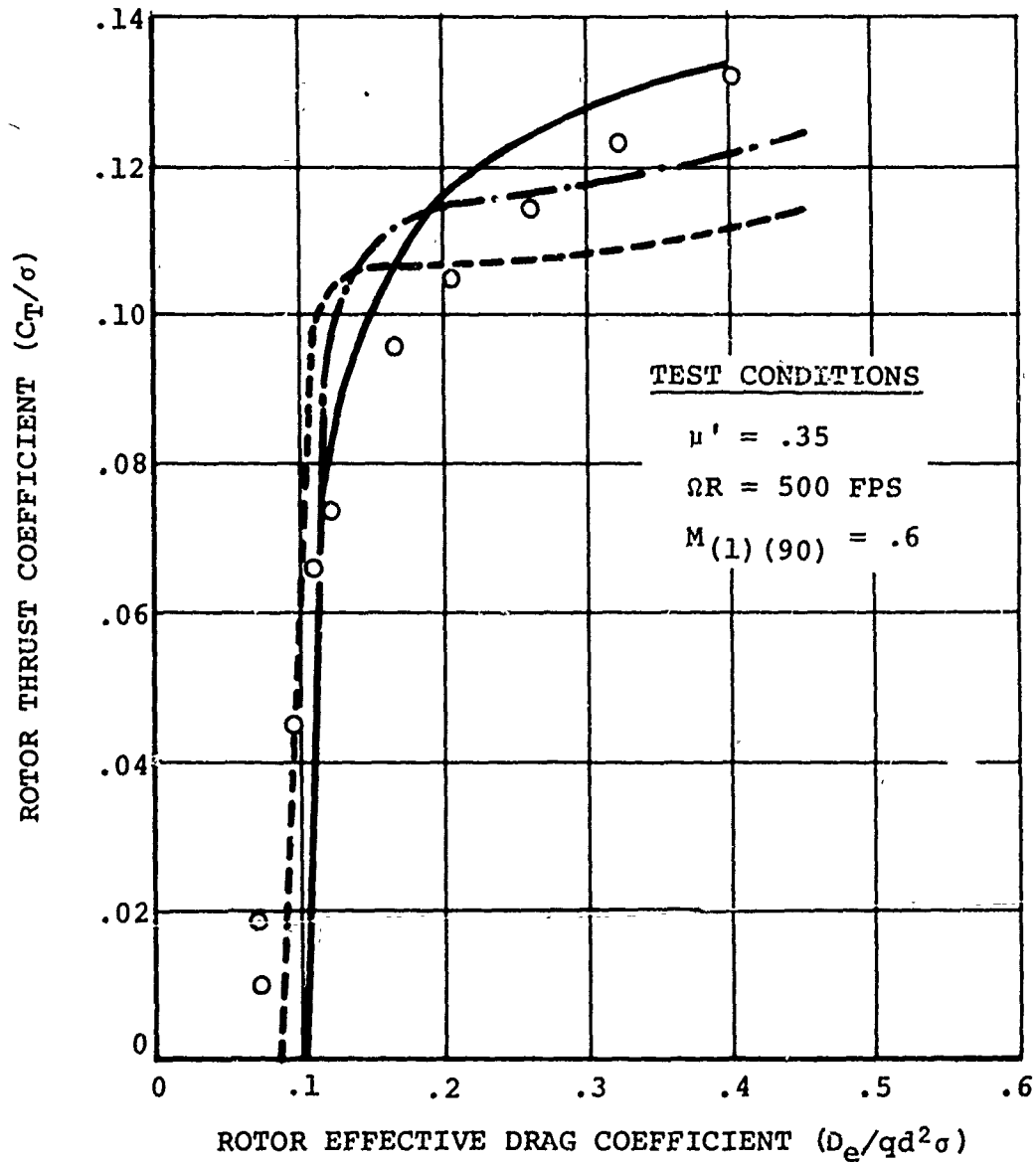


Figure 28. Model Rotor Correlation With Elastic Blade Rotor Theory: Rotor Thrust vs. Rotor Effective Drag.

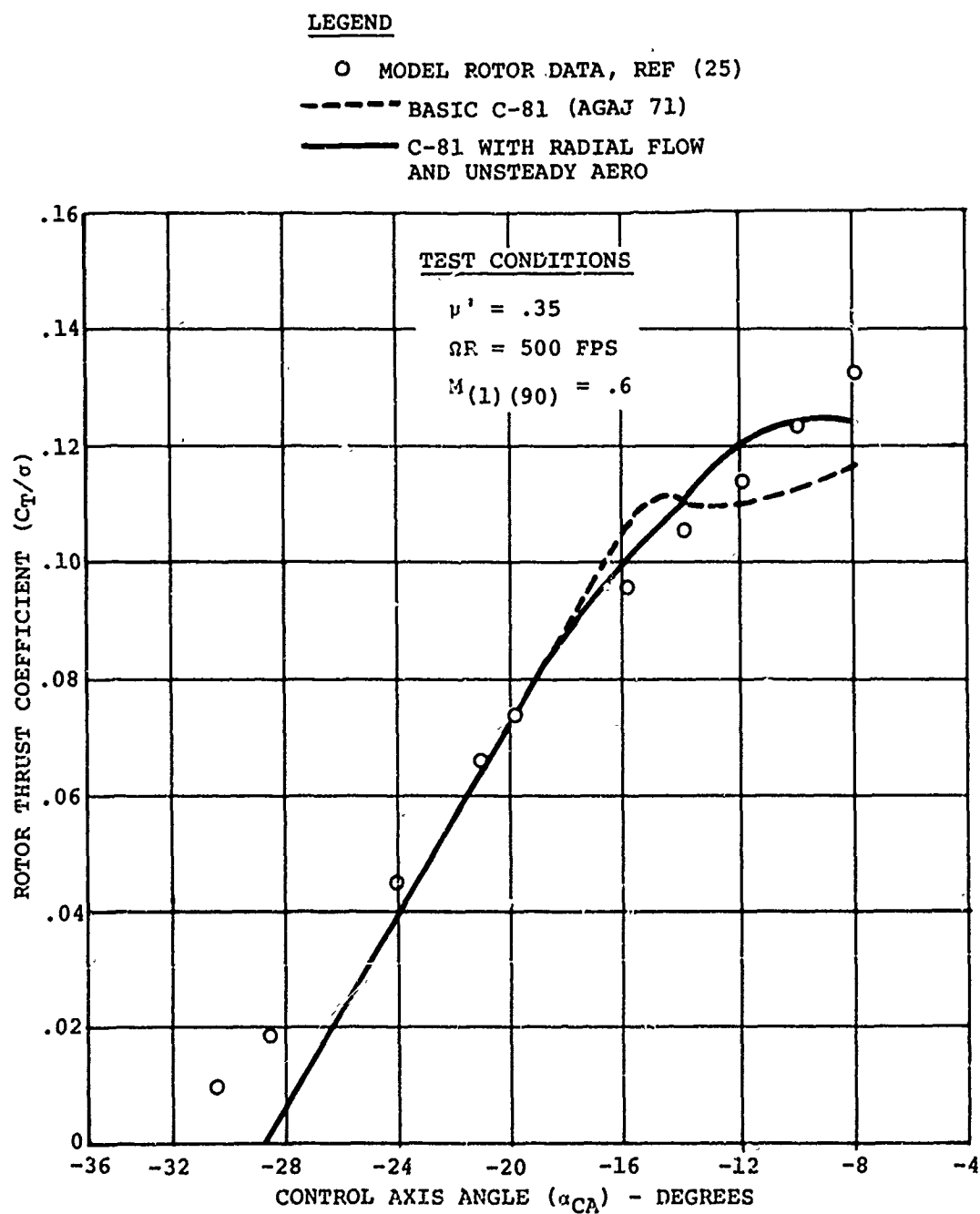


Figure 29. Model Rotor Correlation With Rigid Blade Rotor Theory: Rotor Thrust vs. Control Axis Angle.

LEGEND

- MODEL ROTOR DATA, REF (25)
- BASIC C-81 (AGAJ 71)
- C-81 WITH RADIAL FLOW
AND UNSTEADY AERO

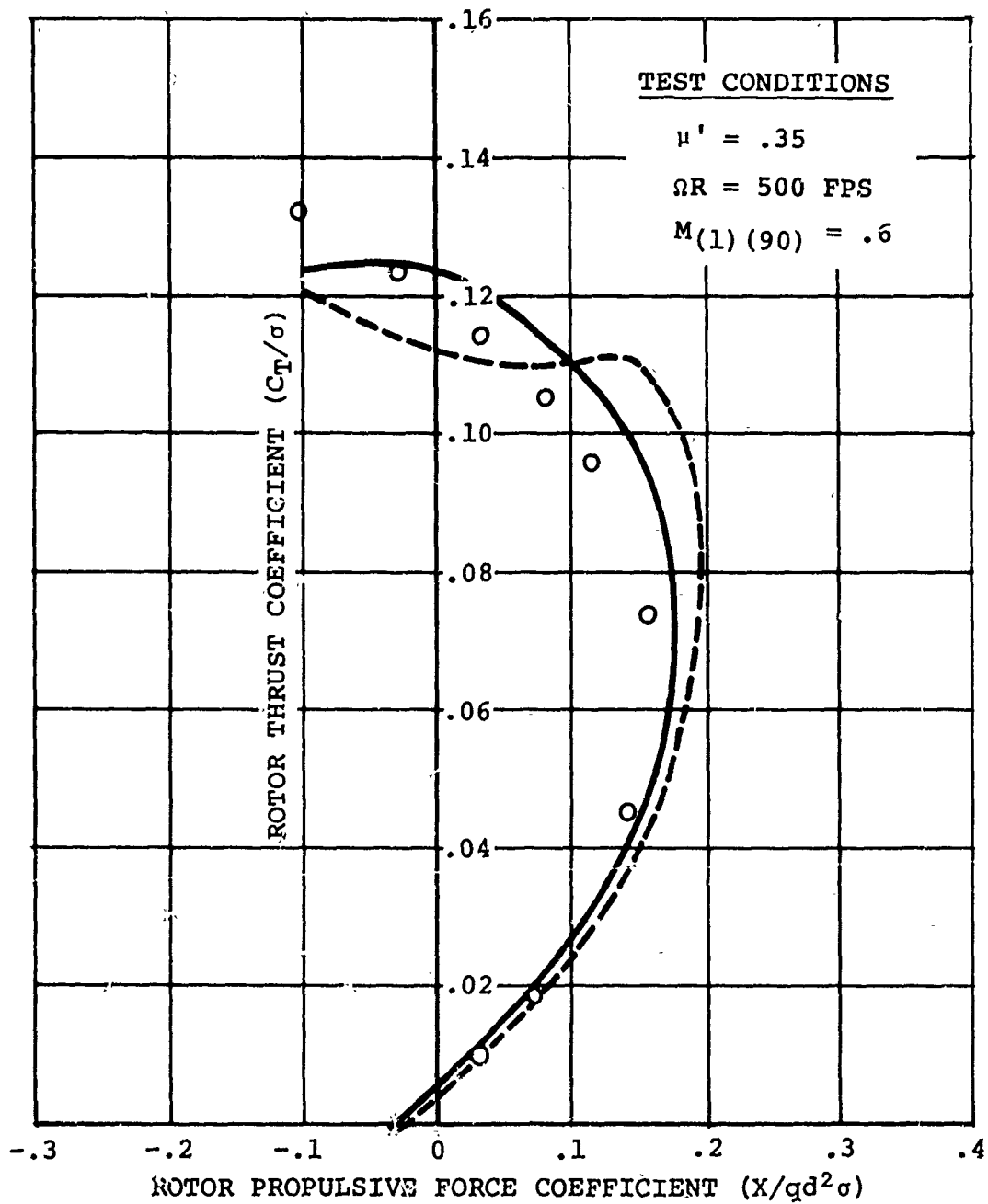


Figure 30. Model Rotor Correlation With Rigid Blade Rotor Theory: Rotor Thrust vs. Rotor Propulsive Force.

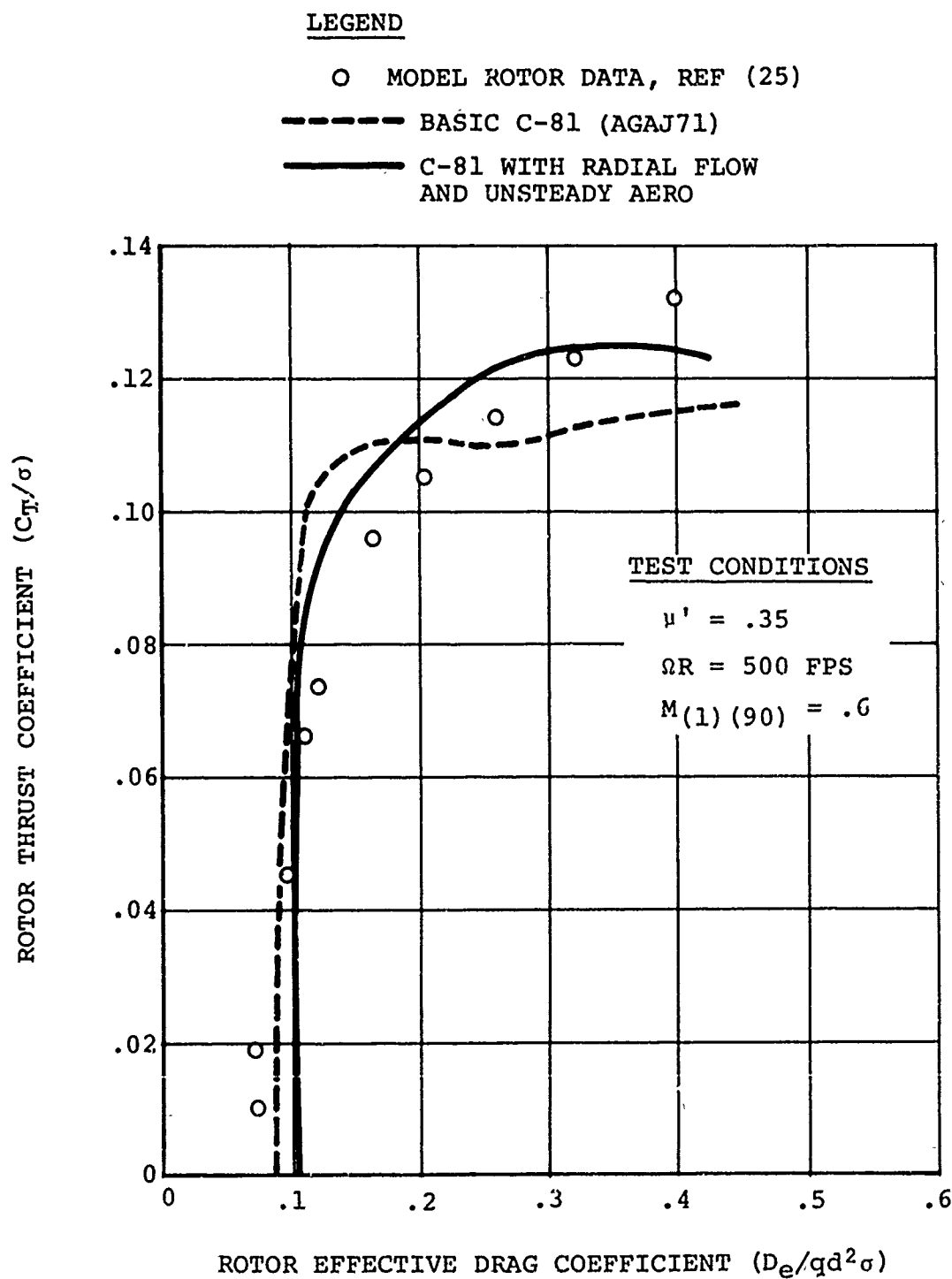


Figure 31. Model Rotor Correlation With Rigid Blade Rotor Theory: Rotor Thrust vs. Rotor Effective Drag.

LEGEND

○ MODEL ROTOR DATA, REF (25)

----- BASIC C-81 (AGAJ 71)

———— C-81 WITH RADIAL FLOW
AND UNSTEADY AERO

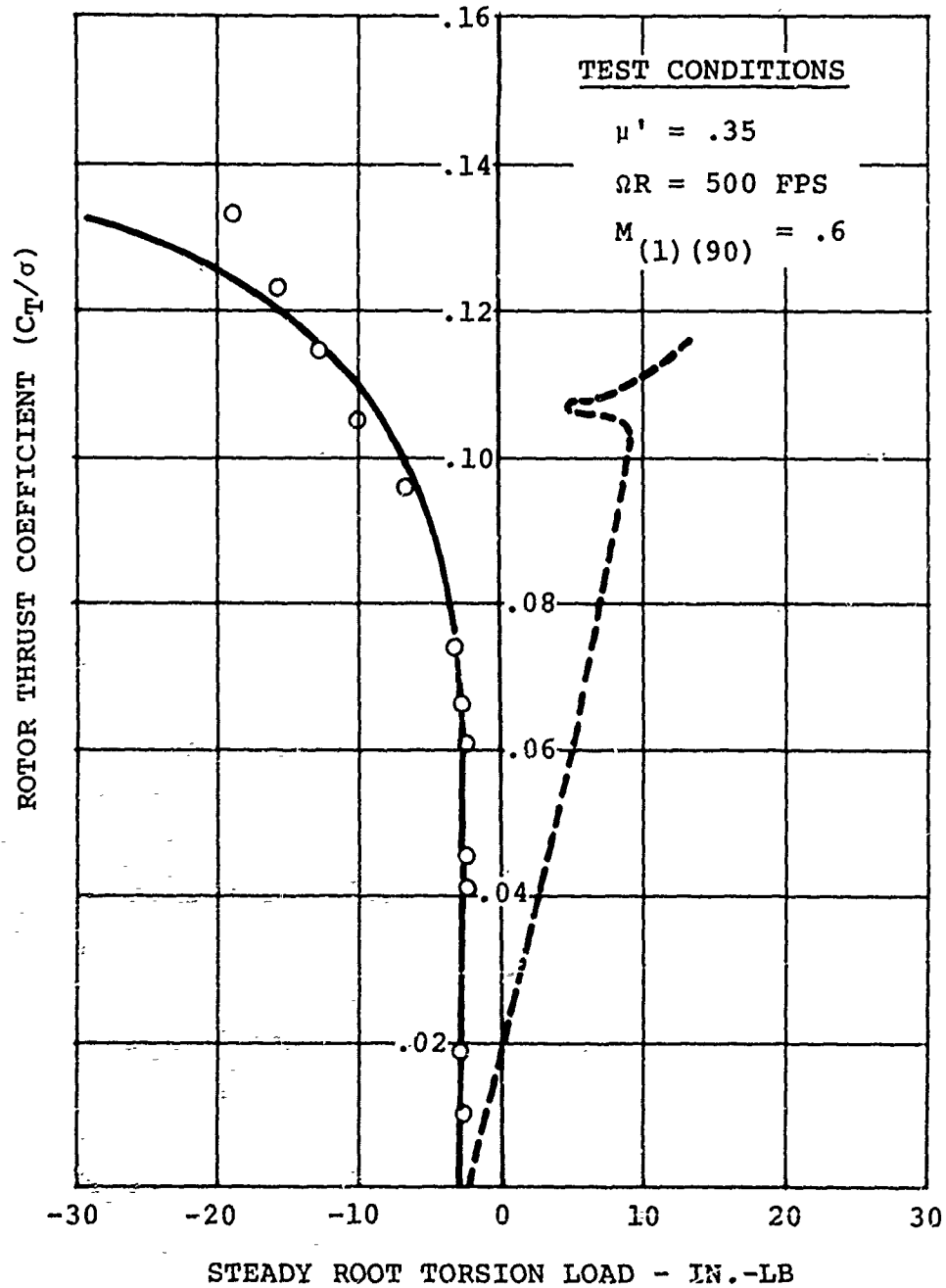


Figure 32. Model Rotor Correlation With Elastic Blade Rotor Theory: Rotor Thrust vs. Steady Root Torsion Load.

LEGEND

- MODEL ROTOR DATA, REF (25)
- BASIC C-81 (AGAJ 71)
- C-81 WITH RADIAL FLOW AND UNSTEADY AERO

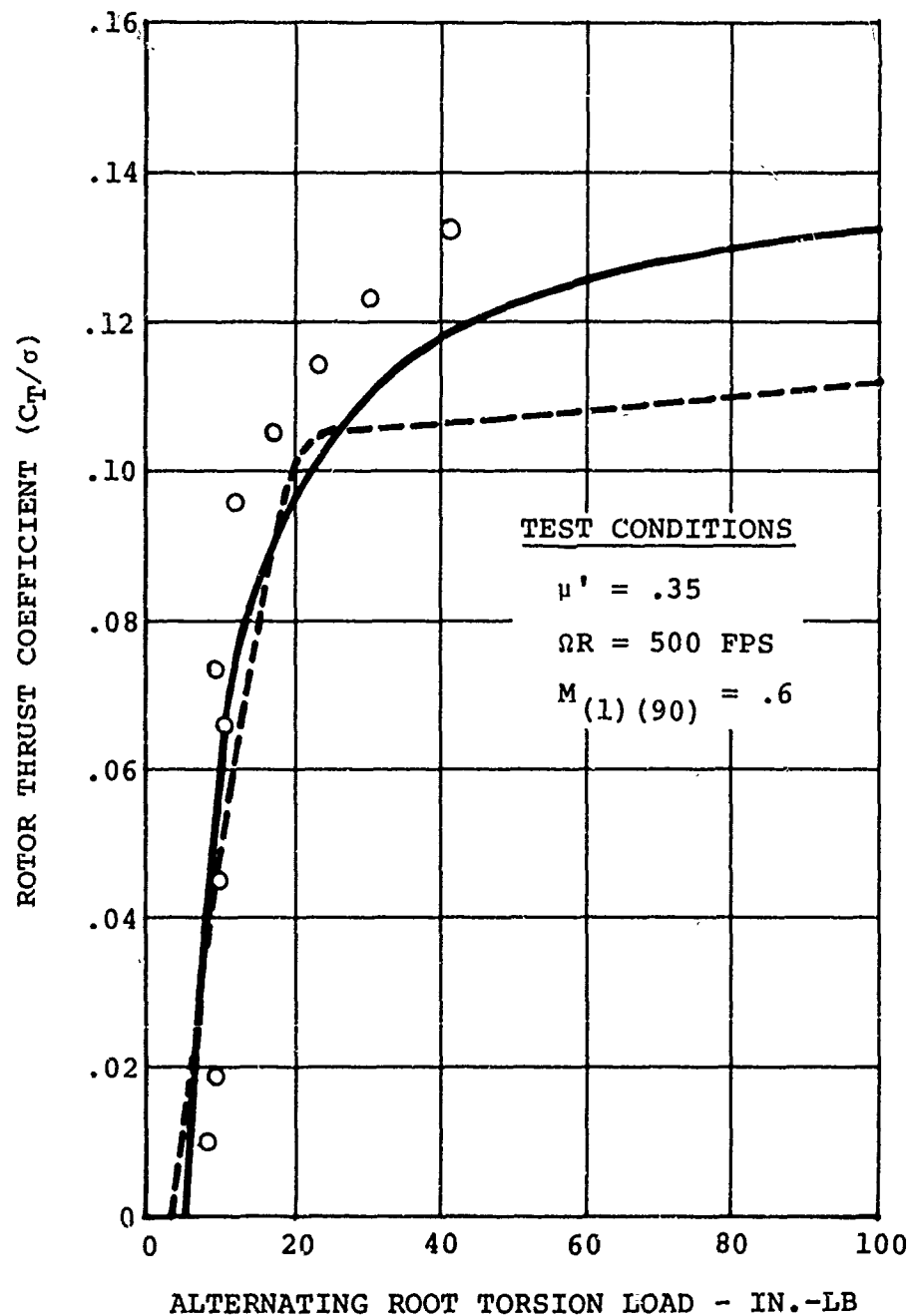


Figure 33. Model Rotor Correlation With Elastic Blade Rotor Theory: Rotor Thrust vs. Alternating Root Torsion Load.

LEGEND

- — — — — MODEL ROTOR WAVEFORM, REF (25)
- - - - - BASIC C-81 (AGAJ 71)
- C-81 WITH RADIAL FLOW AND UNSTEADY AERO

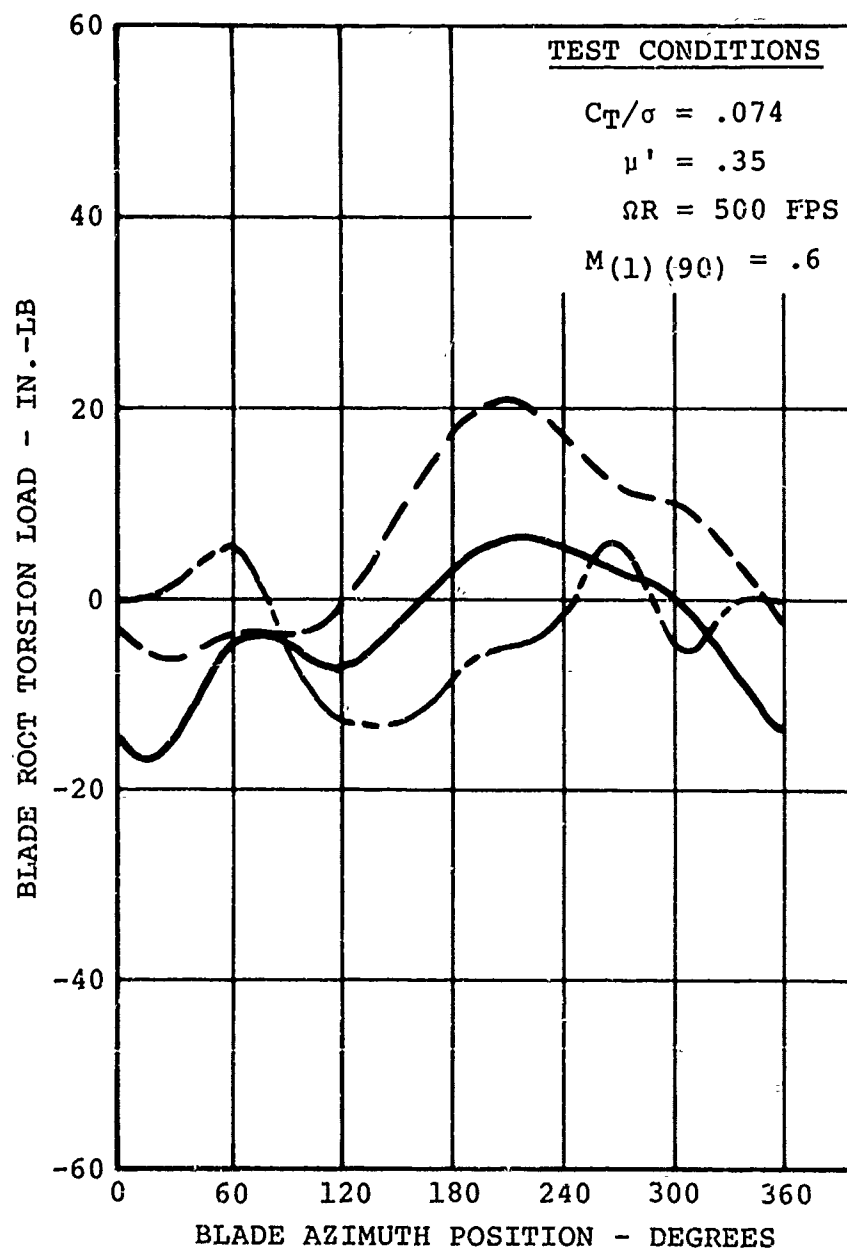


Figure 34. Correlation of Theory and Model Rotor Blade Root Torsion Loads: Blade Root Torsion Load vs. Blade Azimuth Position.

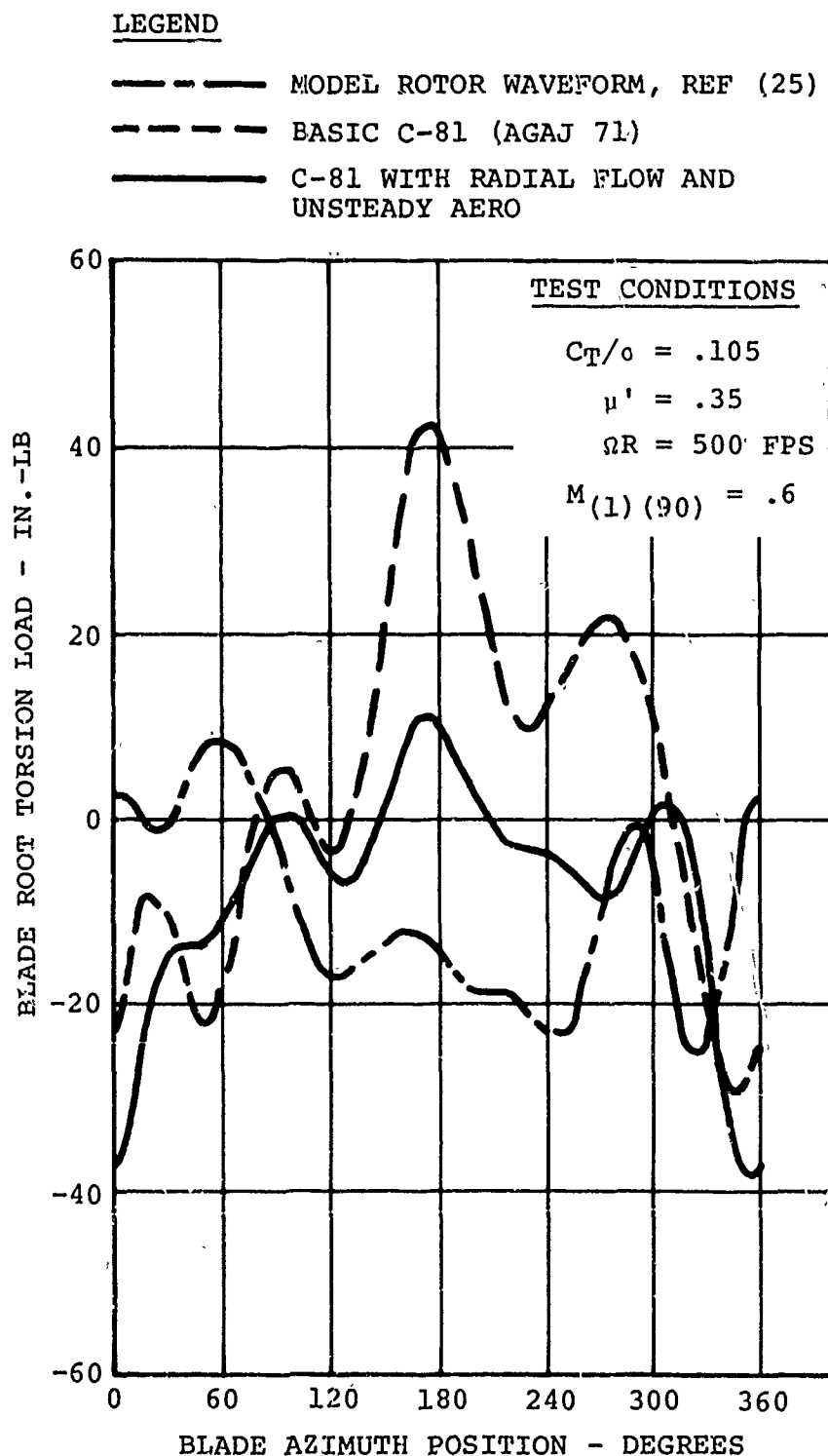


Figure 35. Correlation of Theory and Model Rotor Blade Root Torsion Loads: Blade Root Torsion Load vs. Blade Azimuth Position.

LEGEND

O MODEL ROTOR TEST DATA, REF (25)

--- BASIC C-81 (AGAJ 71)

— C-81 WITH RADIAL FLOW AND
UNSTEADY AERO

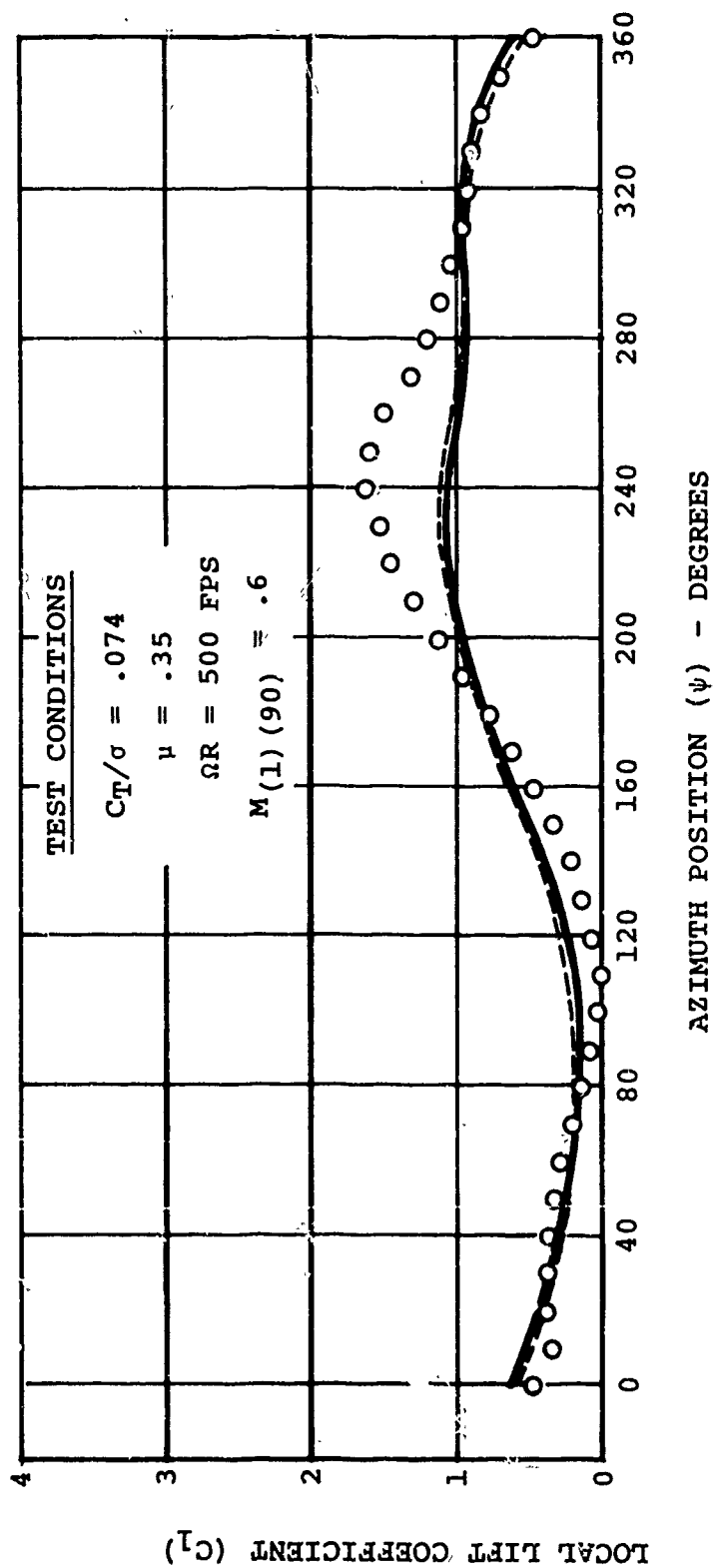


Figure 36. Model Rotor Correlation With Azimuthal Coefficient-of-Lift Variation at .75 Radius.

LEGEND

○ MODEL ROTOR TEST DATA, REF (25)

--- BASIC C-81 (AGAJ 71)

— C-81 WITH RADIAL FLOW AND UNSTEADY AERO

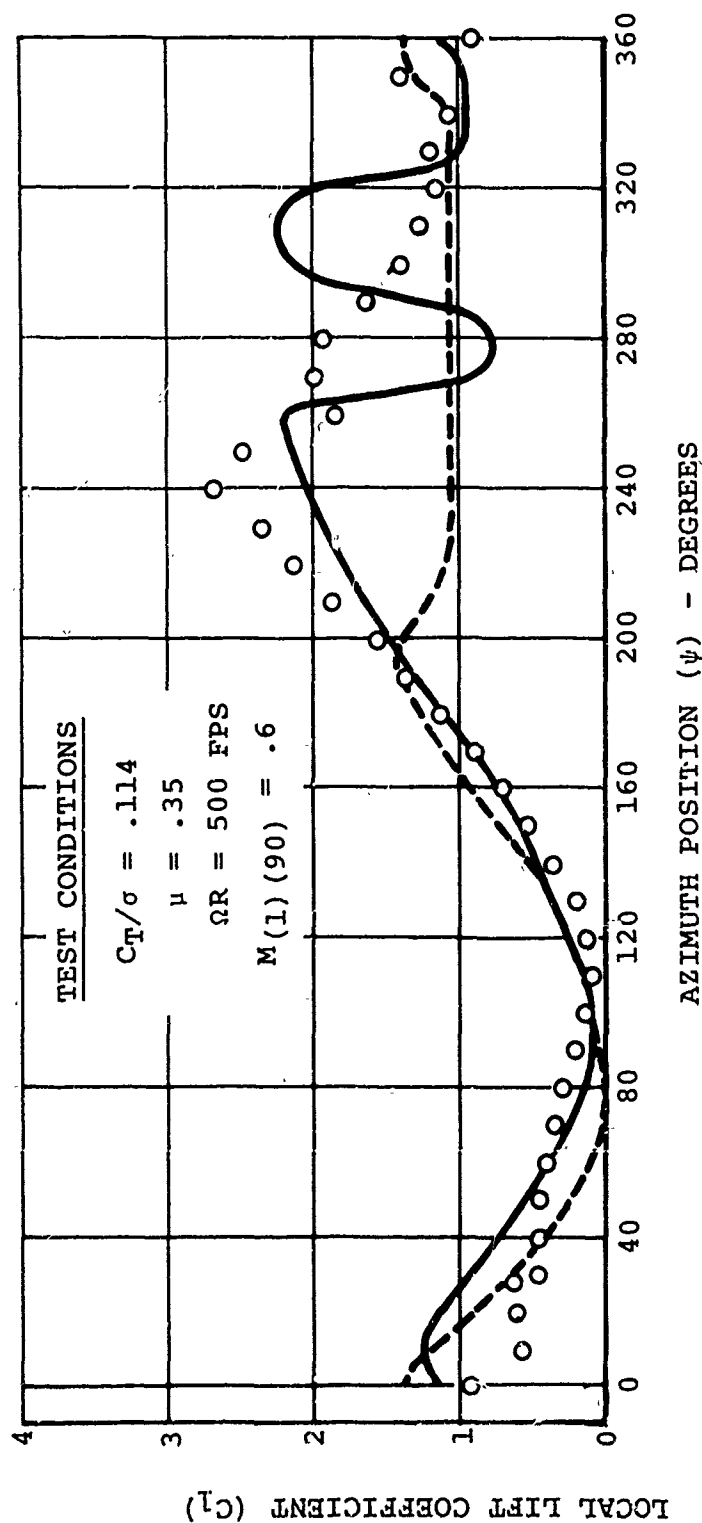


Figure 37. Model Rotor Correlation With Azimuthal Coefficient-of-Lift Variation at .75 Radius.

test levels. At high lift levels, the opposite condition exists: the theory overpredicts thrust levels. This condition basically results in a discrepancy in the ability of the C-81 program to predict accurate lift slope for the shaft sweep. This type of discrepancy between theory and test has been found by other investigators for other rotor analyses. (See for example correlations presented in Reference 3.) The only significant result of this circumstance is that the analysis cannot predict accurate collective estimates at extremely low thrust levels. However, later figures will illustrate that for low thrust levels, the performance estimates are fairly accurate.

The unsteady aerodynamics and radial flow methods developed under this contract produce no differences in the prediction of thrust versus control axis at low thrust levels. However, at high thrust levels, the effects of unsteady aero and radial flow provide improved prediction capability. The basic C-81 analysis is unable to predict the high thrust levels which are measured during rotor model tests. The addition of radial flow provides increased lift prediction at high thrust levels due to extended $C_{l_{max}}$ capability added by the radial flow theory. This theory is still deficient at the extreme high thrust levels of the test data. Adding the unsteady aerodynamics theory allows the theory to predict the test thrust levels and in addition provides improved correlation of the thrust levels and lift slope in the range of C_T/σ of .08 and above. Utilization of the combined unsteady aerodynamic and radial flow theories in C-81 provides the best correlation with test data above stall.

Rotor performance data corresponding to the data of Figure 26 are presented in Figures 27 and 28. Again, the combined unsteady aerodynamics and radial flow theories provide the most accurate prediction of the test results. At low lift levels, the effects of increased skin friction drag levels due to radial flow adjust the predicted rotor propulsive force coefficient, $X/qd^2\sigma$, and rotor effective drag coefficient, $D_e/qd^2\sigma$, to levels obtained during the rotor test. At lift levels where stall becomes significant, the combined unsteady aerodynamics and radial flow theories provide the most accurate estimate of the data trends. Again, the chief factor is the ability of the combined theory to predict more accurate thrust levels compared to the test data.

The correlations presented in Figures 26, 27, and 28 are based on C-81 estimates which were obtained using the elastic rotor option of the program. Figures 29, 30

and 31 present the same correlation with the exception that the elastic rotor capability was not utilized, i. e., the blades are represented as being rigid and are free to flap about the flapping hinge. The correlation results are similar to those obtained in the previous correlations with the elastic rotor representation. The only significant difference occurs at the highest thrust conditions where the correlation indicates that the rigid blade analysis is unable to predict the extreme high thrust levels of the test rotor. This indicates that elastic rotor representation is required to obtain accurate prediction of rotor thrust in deep stall.

Elastic blade torsion response of the 8-foot model rotor is shown in Figures 32 and 33. Steady components of the torsional loads are predicted well by the revised C-81 program. The improved correlation is attributed both to improving the dynamic representation of blade element pitching moment, and the ability of the combined unsteady aero and radial flow theories to predict high rotor thrust levels. Similar correlation results are obtained for the alternating torsion loads which are presented in Figure 33. Typical torsion waveforms are given in Figures 34 and 35 for a case below rotor stall and a case above rotor stall. The improved C-81 program provides better correlation in both examples.

Figures 36 and 37 compare measured and theoretical C_l distributions for a rotor blade element at .75 radius as a function of azimuth position. The 8-foot diameter model rotor²⁵ was equipped with an instrumented blade, capable of measuring chordwise normal pressure distributions. The pressure distributions were then integrated over the chord to obtain section C_n and C_c . Section C_l was obtained by combining C_m and C_c in the following equation:

$$C_l = C_n \cos \alpha + C_c \sin \alpha \quad (82)$$

For an unstalled thrust coefficient of .074, Figure 36 illustrates little influence due to radial flow and unsteady aerodynamics. For a thrust coefficient of .114, Figure 37, where the rotor is operating in a stalled condition, the correlation is considerably improved with the use of the radial flow and unsteady aerodynamics option of the computer program. The primary influence is obtained between azimuth positions of 200° and 260° where the improved analysis more closely predicts the high C_l levels achieved during the rotor test. The excessive C_l variation between azimuth positions of 260° and 330° is due to excessive torsional response of the predicted blade moment at high thrust levels, which was previously shown in Figure 33.

CORRELATION OF THEORY AND HELICOPTER TEST DATA

UH-1H Single-Rotor Helicopter

Figure 38 compares the C-81 analysis with the UH-1H test data. This correlation was performed using fully coupled elastic mode shapes for the UH-1H rotor representation. As the figure indicates, the correlation is excellent for both the basic C-81 and the revised program. Even though a 9500-lb gross weight is near the maximum weight of the UH-1H, this case has a thrust coefficient (C_T/σ) of only 0.08. For the maximum test advance ratio of .25, this thrust level does not represent a case in which rotor stall is significant. Therefore, the use of unsteady aerodynamics and radial flow methods at low lift levels does not have a significant effect on the rotor performance of a UH-1H configuration.

CH-47C Tandem Helicopter

The CH-47C helicopter is capable of attaining advance ratios and gross weights where the effects of rotor stall become significant. Figure 39 illustrates typical correlation at gross weights of 30,000 lb ($C_T/\sigma = .056$) and 50,000 lb ($C_T/\sigma = .094$). These correlations were performed without using the elastic rotor option of the C-81 program. This was done since the basic Government-supplied C-81 analysis was found to be numerically unstable when attempting to analyze a fully articulated rotor configuration with elastic mode shapes. The instability precluded performing the correlation with the use of elastic rotor characteristics. For the 30,000-lb gross weight case, the use of the combined unsteady aerodynamics and radial flow theories gives good correlation with the test data. At 50,000 lb the revised theory provides improved correlation; however, at speeds above 120 knots the test values are still higher than the estimated results. For this case (C_T/σ of .094), the rotor would experience significant stall effects and the elastic response would cause additional losses at high speeds. It is anticipated that including an elastic rotor representation would provide a better rotor estimate for the 50,000-lb condition at high speeds.

Data shown in Figure 39 are for the forward rotor performance only. The correlations shown here are indicative of single-rotor configuration or of a forward-rotor on a tandem-rotor configuration, since it is essentially an isolated rotor. Figure 40 illustrates that the C-81 analysis does not consider the rotor-rotor interference effects which are encountered by the aft rotor of a tandem configuration.

LEGEND

○ UH-1H TEST DATA, REF (26)

----- BASIC C-81 (AGAJ 71)

———— C-81 WITH RADIAL FLOW
AND UNSTEADY AERO

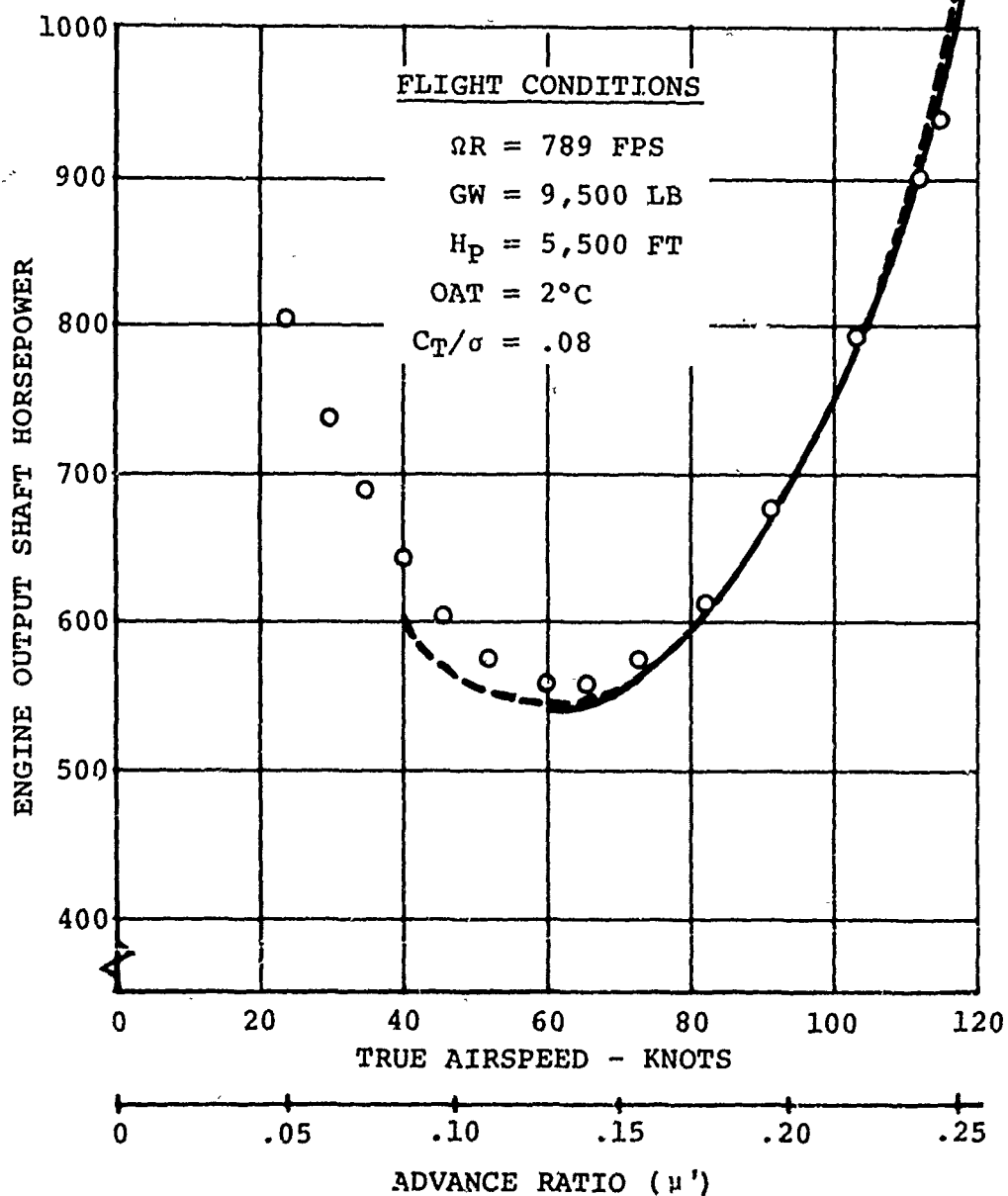


Figure 38. Correlation of Elastic Blade Rotor Theory With UH-1H Test Data.

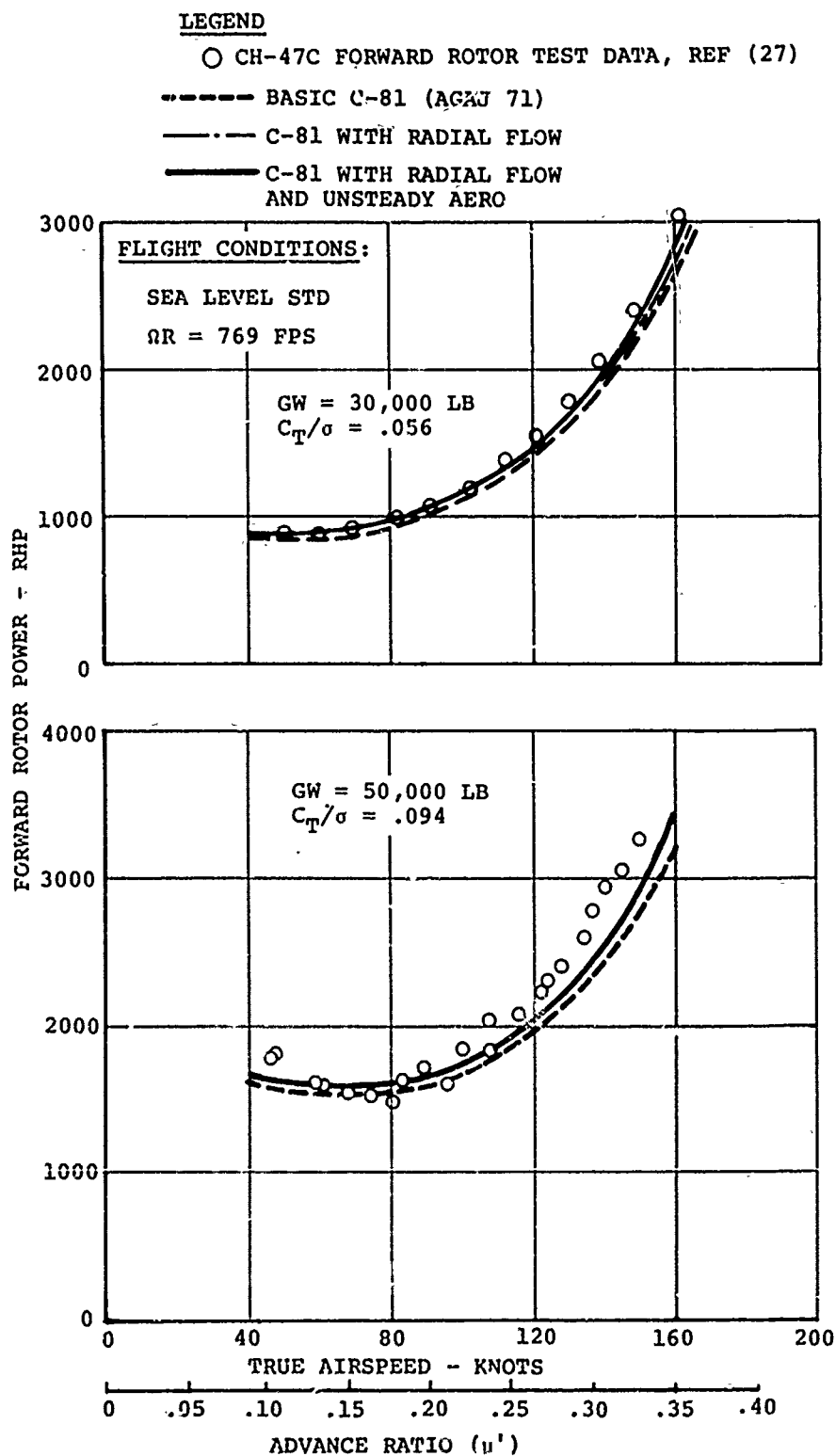


Figure 39. Correlation of Rigid Blade Rotor Theory With CH-47C Force and Rotor Test Data.

Figure 40 includes both the forward and aft rotor correlations for the CH-47C helicopter at a gross weight of 30,000 lb. Since the C-81 analysis does not include an aft rotor interference penalty, a first approximation correction has been applied in order to illustrate the resulting effect on performance level. The forward rotor of a tandem configuration produces an interference velocity which acts on the aft rotor. Due to the interference velocity, the aft rotor essentially operates in a climb condition. The approximation used here combines the interference velocity (v_{INT}) with the aft rotor thrust to obtain an interference power correction. The interference power correction is computed by

$$HP_{INT} = \frac{v_{INT} (T_{AFT ROTOR})}{550} \quad (83)$$

The detailed effects on the aft rotor trim are outside the scope of this report, but should be considered when analyzing aft rotor flight conditions. Derivation of the interference velocity (v_{INT}) is based on considerable theoretical analyses and model tests conducted by The Boeing Company. With the correction applied, the C-81 analysis is shown to give improved correlation when the unsteady aerodynamics and radial flow options are included.

A CH-47C collective pull-up maneuver is illustrated in Figure 40. The maneuver was performed as part of the CH-47C structural demonstration program²⁸. From an initial level flight trim condition, collective pitch was decreased and then rapidly increased to 100% collective in order to demonstrate the "g" capability of the aircraft. Figure 41 compares the load factor (n) time history for the test maneuver with theoretical estimates of C-81. Both versions of the program give adequate correlation with the test data; however, the combined unsteady aerodynamics and radial flow theory is able to predict a slightly higher peak "g" level than the basic C-81 program. Again, the elastic rotor representation could not be utilized for the CH-47C configuration due to numerical instability of the basic C-81 program. Based on the results of Figures 26 and 31, which show that a substantial increase in maximum thrust is predicted when using elastic rotor characteristics, it is anticipated that the revised C-81 program would predict further increases in "g" level if elastic rotor characteristics could be used. The oscillation of the estimated values corresponds to a 3/rev variation of rotor thrust. This vibratory frequency of a three-bladed rotor does not appear in the test data because it was electronically filtered out by the test instrumentation.

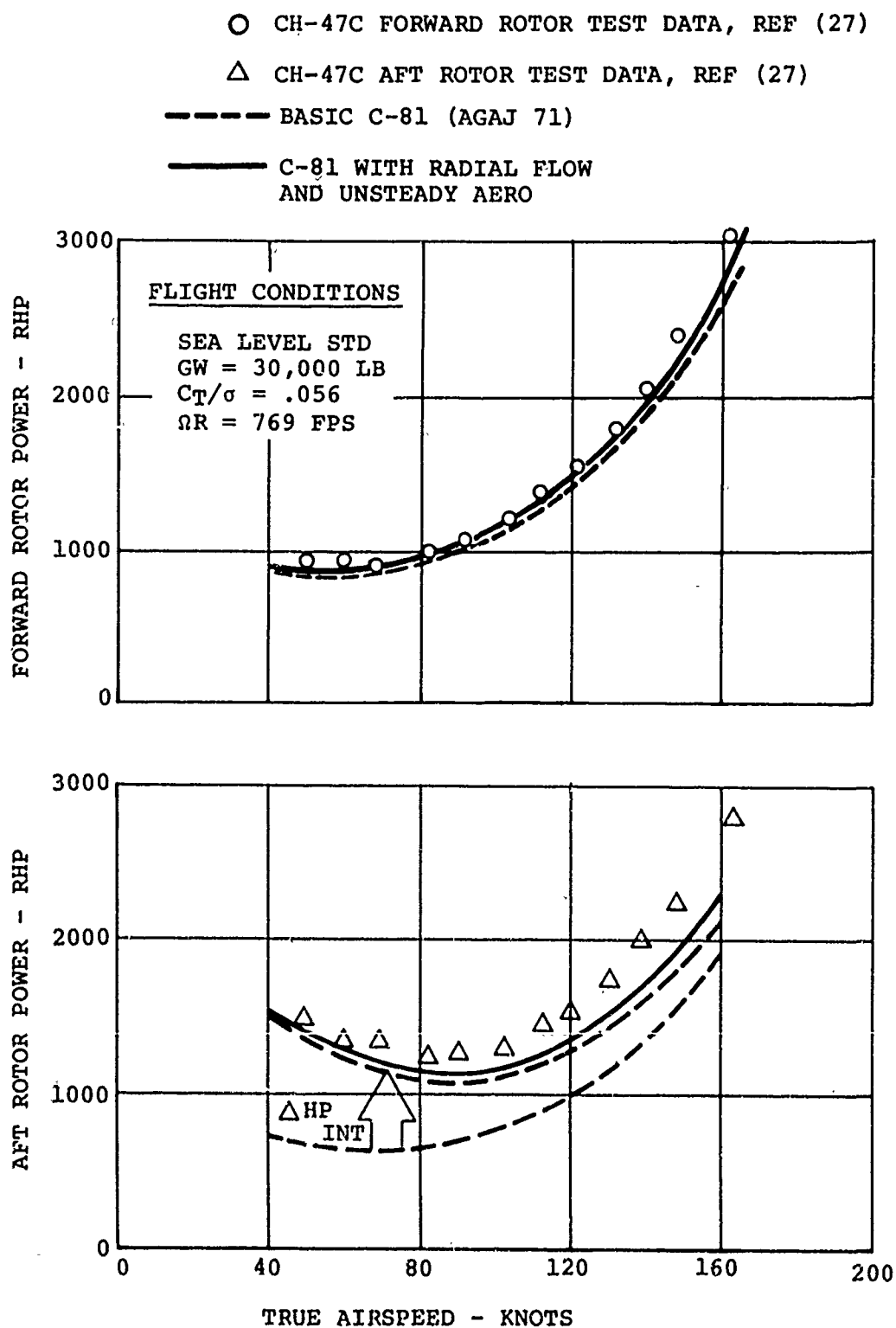


Figure 40. Correlation of Theory With CH-47C Test Data.

LEGEND

CH-47C TEST DATA, REF (28)

BASIC C-81 (AGAJ 71)

C-81 WITH RADIAL FLOW
AND UNSTEADY AERO

FLIGHT CONDITIONS

GW = 33,100 LB

$C_T/\sigma = .068$

$\Omega R = 1,73$ FPS

$V_{FLT} = 165$ KT

$H_D = 3,469$ FT

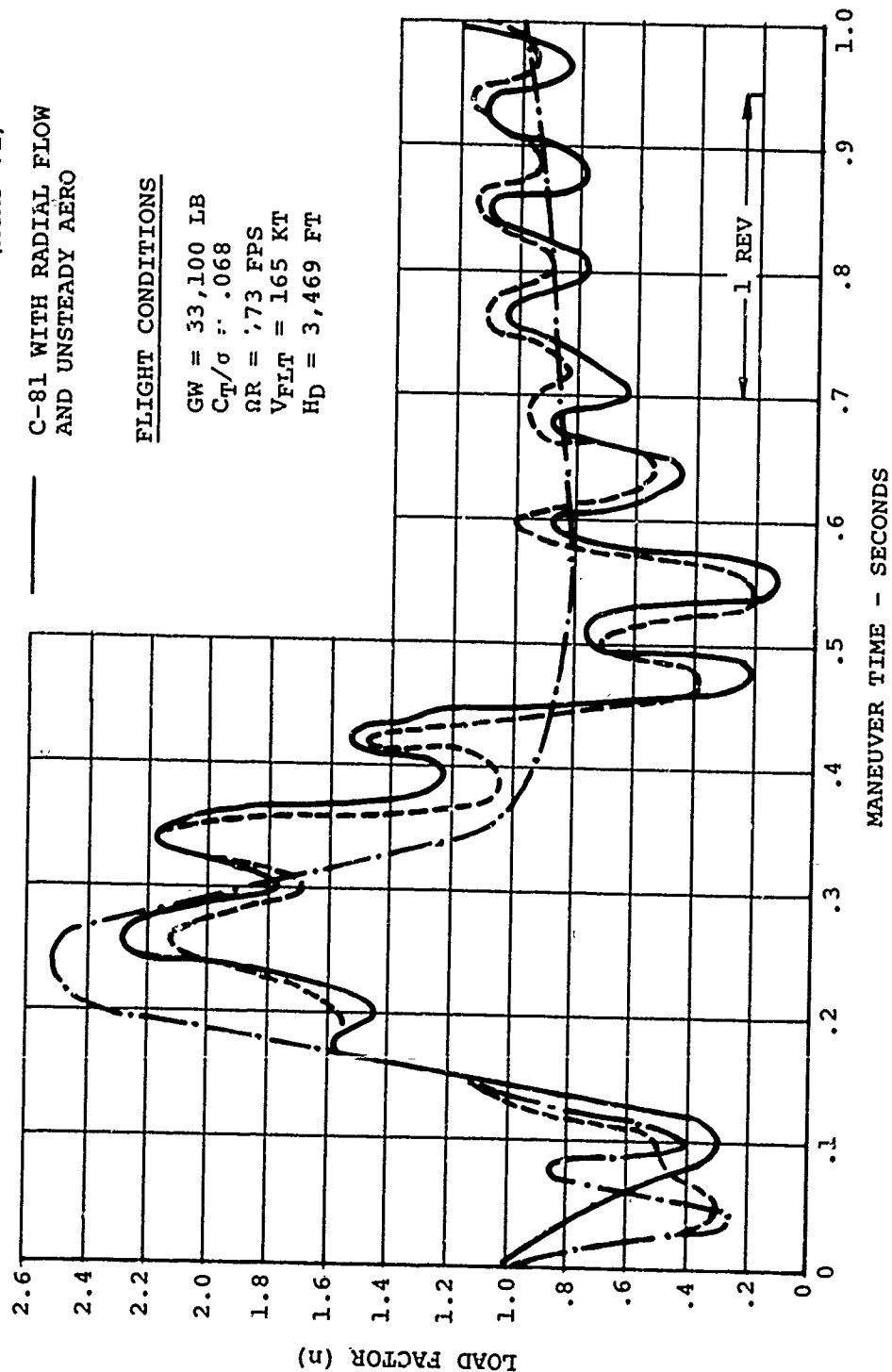


Figure 41. Correlation of Theory With CH-47C Pull-Up Maneuver.

APPENDIX III SAMPLE INPUT AND OUTPUT

Input and output formats of the revised C-81 program are similar to the C-81 (AGAJ71), Reference 24. Changes in input requirements consist of six additional inputs for the forward rotor and aft rotor characteristics. The precise definitions of these additional inputs are described in the USER'S MANUAL section. Figure 42 illustrates a typical input listing. The new inputs are located immediately after the MAIN ROTOR GROUP and immediately after the TAIL ROTOR GROUP.

Headings for the new inputs are:

YAW FLOW: on/off switch for radial flow effects.

ALFACL=0(1) through ALFACL=0(4): coefficients for a third-order curve fit which represents section angle of attack at zero lift coefficient as a function of Mach number.

T/C: thickness ratio of the rotor airfoil section.

(For detailed definition of all other inputs, consult Reference 24.)

All output formats for rotorcraft trim computations remain unchanged from those described in Reference 24. Figure 43 presents a typical final trim output listing.

For maneuver cases, the output also remains unchanged with the exception of the page for Rotor Airload Data. Figure 44 presents a typical airloads output. The revised output consists of:

PSI: blade azimuth position

U-HUB, V-HUB, W-HUB: hub velocity components

GEO. PITCH: blade geometric pitch

BETA (HUB): blade flap angle referenced to hub

STA: blade station

UT, UP, UR: blade element local velocity components

MACH: blade element local Mach number

ALPHA: blade element angle of attack

ALPHAD: time derivative of blade element angle of attack

THETAD: time derivative of blade pitch angle

THETADD: second time derivative of blade pitch angle

CL, CD, CM: blade element lift, drag and moment coefficients (including unsteady aero and radial flow effects, if used)

CDSF: skin friction drag coefficient used in radial flow computations

BELL HELICOPTER COMPANY
 ROTORCRAFT FLIGHT SIMULATION PROGRAM AGAJ71
 COMPILED 06/15/71
 COMPUTED 05/12/72

2 0 CH-47C

INPUT DATA

FUSELAGE GROUP - CH47C

33100.00	348.5899	0.0	26.89999	332.5000	0.0	10.30000
37163.00	201750.0	190059.0	14632.00	0.0	0.0	0.0
-40.00000	70.09000	0.0	11.00000	0.0	-12.00000	4.879999
46.50000	-0.7230000	0.8624997E-01	0.1422000	0.0	6.849999	0.0
0.0	0.0	0.0	0.0	0.0	0.0	0.0

FWD ROTOR GROUP CH-47C

3.000000	0.0	0.0	30.00000	25.25000	-9.139999	30.00000
85.00000	0.0	181.1000	9.000000	0.0	0.1561000E-01	0.0
20.00000	1.000000	0.0	1056.500	0.0	805.0000	5.750000
0.0	-0.6094000	0.0	0.0	1.000000	10.00000	0.0
0.0	0.0	0.0	0.0	0.0	0.0	0.0
6.799999	6.770000	2.150000	0.8649999	1.040000	0.9100000	0.9780000
0.8680000	0.8500000	0.8500000	0.8160000	0.7600000	0.7600000	0.7670000
0.7720000	0.7600000	0.7600000	0.7600000	0.7600000	0.7640000	7.500000
0.0	0.0	0.0	0.0	0.0	0.0	0.0
0.0	0.0	0.0	0.0	0.0	0.0	0.0
0.0	0.0	0.0	0.0	0.0	0.0	0.0
0.1890000	0.1585000	0.4240000E-01	0.1430000E-01	0.1040000	0.7949996E-01	0.7699996E-01
0.7639998E-01	0.7609999E-01	0.7609999E-01	0.7559997E-01	0.7489997E-01	0.7489997E-01	0.8260000E-01
0.8749998E-01	0.7489997E-01	0.7489997E-01	0.7489997E-01	0.7489997E-01	0.8889997E-01	-1.000000
0.8000000	1.200000	1.629999	0.2810000	-1.422999	-0.4870000	1.000000
0.1180000	0.2700000E-01	-0.4650000E-01	0.1580000	0.0	0.0	0.0
0.0	0.0	0.0	-1.000000	0.0	1.000000	1.000000
0.0	0.0	0.0	0.0	0.0	0.0	0.0

YAW FLOW
3.000000

ALFACL=0(1)
0.2000000

ALFACL=0(2)
1.605000

ALFACL=0(3)
-2.815000

ALFACL=0(4)
1.209999

T/C
0.1020000

V23010-1.58/277CL, CD/502-412CM

AFT ROTOR GROUP CH-47C

3.000000	0.0	0.0	30.00000	25.25000	-9.139999	30.00000
552.5000	0.0	157.1000	4.000000	0.0	0.1561000E-01	1.000993

TAIL ROTOR GROUP

Figure 42. Typical Input (Sheet 1 of 3).

20.00000	1.000000	0.0	1056.500	0.0	805.0000	5.750000
0.0	-0.6094000	0.0	0.0	1.000000	10.00000	0.0
0.0	0.0	0.0	0.0	0.0	0.0	0.0
6.799999	6.770000	2.150000	0.8549999	1.040000	0.9100000	0.9780000
0.8680000	0.8500000	0.8500000	0.8160000	0.7600000	0.7600000	0.7679090
0.7720000	0.7600000	0.7600000	0.7600000	0.7600000	0.7640000	7.500000
0.0	0.0	0.0	0.0	0.0	0.0	0.0
0.0	0.0	0.0	0.0	0.0	0.0	0.0
0.0	0.0	0.0	0.0	0.0	0.0	0.0
0.1890000	0.1585000	0.4240000E-01	0.1430000E-01	0.1040000	0.7949996E-01	0.7699996E-01
0.7639998E-01	0.7609999E-01	0.7609999E-01	0.7559997E-01	0.7489997E-01	0.7489997E-01	0.8260000E-01
0.8749998E-01	0.7489997E-01	0.7489997E-01	0.7489997E-01	0.7489997E-01	0.8889997E-01	-1.000000
0.8000000	1.200000	1.629999	0.2810000	-1.422999	-0.4870000	1.000000
0.1180000	0.2700000E-01	-0.4650000E-01	0.1580000	0.0	0.0	0.0
0.0	0.0	0.0	0.0	0.0	1.000000	1.000000
0.0	0.0	0.0	0.0	0.0	0.0	0.0
YAW FLOW	ALFACL=0(1)	ALFACL=0(2)	ALFACL=0(3)	ALFACL=0(4)	T/C	
3.000000	0.2000000	1.605000	-2.815000	1.209999	0.1020000	
WING GROUP - NO WING						
WING GROUP						
0.0	0.0	0.0	0.0	0.0	0.0	0.0
0.0	0.0	0.0	0.0	0.0	0.0	0.0
0.0	0.0	0.0	0.0	0.0	0.0	0.0
0.0	0.0	0.0	0.0	0.0	0.0	0.0
0.0	0.0	0.0	0.0	0.0	0.0	0.0
0.0	0.0	0.0	0.0	0.0	0.0	0.0
0.0	0.0	0.0	0.0	0.0	0.0	0.0
ELEVATOR GROUP - NO ELEVATOR						
ELEVATOR GROUP						
0.0	0.0	0.0	0.0	0.0	0.0	0.0
0.0	0.0	0.0	0.0	0.0	0.0	0.0
0.0	0.0	0.0	0.0	0.0	0.0	0.0
0.0	0.0	0.0	0.0	0.0	0.0	0.0
0.0	0.0	0.0	0.0	0.0	0.0	0.0
0.0	0.0	0.0	0.0	0.0	0.0	0.0
FIN/RUDDER GROUP - NO FIN OR RUDDER						
FIN/RUDDER GROUP						
0.0	0.0	0.0	0.0	0.0	0.0	0.0
0.0	0.0	0.0	0.0	0.0	0.0	0.0
0.0	0.0	0.0	0.0	0.0	0.0	0.0
0.0	0.0	0.0	0.0	0.0	0.0	0.0
0.0	0.0	0.0	0.0	0.0	0.0	0.0
JET GROUP - NO JET						
JET GROUP						
0.0	0.0	0.0	0.0	0.0	0.0	0.0
0.0	0.0	0.0	0.0	0.0	0.0	0.0

Figure 42. Continued (Sheet 2 of 3) .

20.00000	1.000000	0.0	1056.500	0.0	805.0000	5.750000
0.0	-0.6094000	0.0	0.0	1.000000	10.00000	0.0
0.0	0.0	0.0	0.0	0.0	0.0	0.0
6.799999	6.770000	2.150000	0.8649999	1.040000	0.9100000	0.9780000
0.8630000	0.8500000	0.8500000	0.8160000	0.7600000	0.7600000	0.7670000
0.7720000	0.7600000	0.7600000	0.7600000	0.7600000	0.7640000	7.500000
0.0	0.0	0.0	0.0	0.0	0.0	0.0
0.0	0.0	0.0	0.0	0.0	0.0	0.0
0.0	0.0	0.0	0.0	0.0	0.0	0.0
0.1890000	0.1585000	0.4240000E-01	0.1430000E-01	0.1040000	0.7949996E-01	0.7699996E-01
0.7639998E-01	0.7609999E-01	0.7609999E-01	0.7559997E-01	0.7489997E-01	0.7489997E-01	0.8260000E-01
0.8749998E-01	0.7489997E-01	0.7489997E-01	0.7489997E-01	0.7489997E-01	0.8889997E-01	-1.050000
0.8000000	1.200000	1.629999	0.2810000	-1.422999	-0.4870000	1.000000
0.1180000	0.2700000E-01	-0.4650000E-01	0.1590000	0.0	0.0	0.0
0.0	0.0	0.0	0.0	0.0	1.000000	1.000000
0.0	0.0	0.0	0.0	0.0	0.0	0.0
YAW FLOW	ALFACL=0(1)	ALFACL=0(2)	ALFACL=0(3)	ALFACL=0(4)	T/C	
3.000000	0.2000000	1.605000	-2.815000	1.209999	0.1020000	
WING GROUP - NO WING						
WING GROUP						
0.0	0.0	0.0	0.0	0.0	0.0	0.0
0.0	0.0	0.0	0.0	0.0	0.0	0.0
0.0	0.0	0.0	0.0	0.0	0.0	0.0
0.0	0.0	0.0	0.0	0.0	0.0	0.0
0.0	0.0	0.0	0.0	0.0	0.0	0.0
0.0	0.0	0.0	0.0	0.0	0.0	0.0
0.0	0.0	0.0	0.0	0.0	0.0	0.0
0.0	0.0	0.0	0.0	0.0	0.0	0.0
ELEVATOR GROUP - NO ELEVATOR						
ELEVATOR GROUP						
0.0	0.0	0.0	0.0	0.0	0.0	0.0
0.0	0.0	0.0	0.0	0.0	0.0	0.0
0.0	0.0	0.0	0.0	0.0	0.0	0.0
0.0	0.0	0.0	0.0	0.0	0.0	0.0
0.0	0.0	0.0	0.0	0.0	0.0	0.0
0.0	0.0	0.0	0.0	0.0	0.0	0.0
0.0	0.0	0.0	0.0	0.0	0.0	0.0
FIN/RUDDER GROUP - NO FIN OR RUDDER						
FIN/RUDDER GROUP						
0.0	0.0	0.0	0.0	0.0	0.0	0.0
0.0	0.0	0.0	0.0	0.0	0.0	0.0
0.0	0.0	0.0	0.0	0.0	0.0	0.0
0.0	0.0	0.0	0.0	0.0	0.0	0.0
0.0	0.0	0.0	0.0	0.0	0.0	0.0
0.0	0.0	0.0	0.0	0.0	0.0	0.0
JET GROUP - NO JET						
JET GROUP						
0.0	0.0	0.0	0.0	0.0	0.0	0.0
0.0	0.0	0.0	0.0	0.0	0.0	0.0

Figure 42. Continued (Sheet 2 of 3) .

CONTROLS GROUP						
9.120000	7.849999	0.0	CONTROLS GROUP			
0.0	1.000000	0.0	0.0	17.00000	17.00000	0.0
13.00000	-4.000000	8.000000	0.0	0.0	0.0	0.0
-1.000000	1.000000	1.660000	1.000000	3.500000	0.0	0.0
8.360000	-8.000000	16.00000	0.0	0.0	0.0	0.0
0.0	0.0	0.0	0.0	1.000000	0.0	0.0
7.200000	-11.43000	22.85999	0.0	0.0	1.000000	0.0
0.0	0.0	0.0	0.0	-1.000000	0.0	0.0
0.0	0.0	0.0	0.0	0.0	0.0	0.0
ALLOWABLE ERROR GROUP						
100.0000	100.0000	100.0000	ALLOWABLE ERROR GROUP			
			1000.000	100.0000	1000.000	1000.000
ITERATION LOGIC GROUP						
40.00000	0.0	9.000000	ITERATION GROUP			
0.0	0.0	1600.000	0.500000	1.000000	0.0	0.9000000
2.000000	0.0	0.0	1000.000	0.5000000	0.5000000E-01	3000.000
			0.0	0.0	0.0	0.0
FLIGHT CONSTANTS GROUP						
165.0000	0.0	0.0	1000.000	-0.8960000	-4.480000	0.0
54.28000	36.32999	55.53000	55.85999	0.0	0.0	0.0
3.398999	-0.1440000	2.594000	1.681000	17782.00	18308.00	0.0
2.000000	0.0	0.0	15691.00	7500.000	1102.000	0.9022999
BOBWEIGHT GROUP - NO BOBWEIGHT						
0.0	0.0	0.0	BOBWEIGHT GROUP			
			0.0	0.0	0.0	0.0
WEAPONS GROUP - NO WEAPONS						
0.0	0.0	0.0	WEAPON GROUP			
			0.0	0.0	0.0	0.0
SCAS GROUP - NO SCAS						
0.0	0.0	0.0	SCAS GROUP			
0.0	0.0	0.0	0.0	0.0	0.0	0.0
0.0	0.0	0.0	0.0	0.0	0.0	0.0
0.0	0.0	0.0	0.0	0.0	0.0	0.0
STABILITY TIMES GROUP						
0.0	0.0	0.0	STAB TIMES GROUP			
0.0	0.0	0.0	0.0	0.0	0.0	0.0
			0.0	0.0	0.0	0.0
AIRLOAD PRINTOUT TIMES GROUP						
0.0	0.0	0.0	AIRLOAD TIMES GROUP			
0.0	0.0	0.0	0.0	0.0	0.0	0.0
			0.0	0.0	0.0	0.0

Figure 42. Continued (Sheet 3 of 3).

BELL HELICOPTER COMPANY
 ROTORCRAFT FLIGHT SIMULATION PROGRAM AGAJ71
 COMPILED 06/15/71
 COMPUTED 05/12/72

HELICOPTER IS IN STABLE CONDITION.

ROTOR COLLECTIVE PITCH	(DEGREES)	FWD	AFT	WING ANGLE OF ATTACK	(DEGREES)	0.0
F/A CYCLIC PITCH	(DEGREES)	3.500	3.500	BODY Z-FORCE (+DOWN)	(LBS)	0.0
LAT CYCLIC PITCH	(DEGREES)	0.406	1.642	BODY X-FORCE (+FWD)	(LBS)	0.0
F/A FLAPPING	(DEGREES)	4.037	3.007	ELEVATOR ANGLE OF ATTACK	(DEGREES)	0.0
LAT FLAPPING	(DEGREES)	-0.128	1.773	BODY Z-FORCE (+DOWN)	(LBS)	0.0
THRUST	(LBS)	17952.750	18525.152	BODY X-FORCE (+FWD)	(LBS)	0.0
H-FORCE	(LBS)	1773.267	1477.733	RUDDER ANGLE OF ATTACK	(DEGREES)	0.0
Y-FORCE	(LBS)	-118.845	664.069	BODY Y-FORCE (+RIGHT)	(LBS)	0.0
HORSEPOWER		2953.738	2226.312	BODY X-FORCE (+FWD)	(LBS)	0.0
RPM		244.936	244.936	HELICOPTER EULER ANGLE YAW	(DEGREES)	-0.960
MAST TILT ANGLE	(DEGREES)	9.000	4.000	PITCH	(DEGREES)	-5.480
BLADE INERTIA (SLUG-FT-SQ)		2862.826	2862.826	ROLL	(DEGREES)	0.0
JET THRUST, LEFT SIDE	(LBS)	0.0	0.0	RATE OF CLIMB	(FT/SEC)	0.0
RIGHT SIDE	(LBS)	0.0	0.0	FORWARD SPEED	(KNOTS)	165.003
PCT CONTROL USED COLLECTIVE		57.092		GROSS WEIGHT	(LBS)	33100.000
F/A CYCLIC		36.489		ENGINE RPM		15691.000
LAT CYCLIC		56.480		C.G. STATION LINE	(IN)	332.500
PEDAL		52.704		WATER LINE	(IN)	10.200
29 ITERATIONS				MINUTES ELAPSED COMPUTING TIME		7.023

PART 1

Figure 43. Typical Final Trim Output.

PSI =	0.	U-HUB =	269.63	V-HUB =	4.67	W-HUB =	-69.62	GEO. PITCH =	18.22	BETA(HUB) =	-4.04	
STA	UT	JP	UR	MACH	ALPHA	ALPHAD	THETAD	THETADD	CL	CD	CDSF	CM
1	772.25	-66.61	-274.85	0.703	4.15	-150.12	-89.88	269.09	0.7641	0.0258	0.0073	-0.0508
2	733.87	-65.80	-274.80	0.668	4.41	-146.02	-89.88	269.09	0.7754	0.0241	0.0073	-0.0463
3	695.49	-64.99	-274.75	0.633	4.65	-141.26	-89.88	269.09	0.7835	0.0202	0.0074	-0.0402
4	657.11	-64.19	-274.70	0.599	4.87	-135.69	-89.88	269.09	0.7886	0.0140	0.0075	-0.0330
5	618.73	-63.38	-274.65	0.564	5.06	-129.10	-89.88	269.09	0.7906	0.0131	0.0075	-0.0316
6	580.35	-62.57	-274.60	0.529	5.21	-121.23	-89.88	269.09	0.7892	0.0111	0.0076	-0.0298
7	541.97	-61.77	-274.55	0.494	5.32	-111.71	-89.88	269.09	0.7836	0.0086	0.0077	-0.0276
8	503.59	-60.96	-274.50	0.460	5.37	-100.05	-89.88	269.09	0.7677	0.0088	0.0078	-0.0247
9	465.21	-60.15	-274.45	0.425	5.37	-85.53	-89.88	269.09	0.7438	0.0091	0.0079	-0.0210
10	426.83	-59.35	-274.39	0.390	5.27	-67.13	-89.88	269.09	0.7104	0.0094	0.0080	-0.0182
11	388.45	-58.54	-274.34	0.355	5.08	-43.31	-89.88	269.09	0.6644	0.0098	0.0081	-0.0190
12	350.08	-57.73	-274.29	0.320	4.74	-11.69	-89.88	269.09	0.6009	0.0107	0.0083	-0.0192
13	311.70	-56.93	-274.24	0.285	4.21	31.58	-89.88	269.09	0.5128	0.0124	0.0084	-0.0197
14	273.32	-56.12	-274.19	0.251	3.42	93.01	-89.88	269.09	0.3893	0.0139	0.0086	-0.0054
15	234.94	-55.31	-274.14	0.216	2.23	184.39	-89.88	269.09	0.2132	0.0343	0.0088	0.0162
16	196.56	-54.51	-274.09	0.181	0.43	328.59	-89.88	269.09	-0.0516	0.0957	0.0091	0.0799
17	158.18	-53.70	-274.04	0.146	-2.36	574.47	-89.88	269.09	-0.4315	0.3232	0.0094	0.1850
18	119.80	-52.89	-273.99	0.138	0.0	0.0	-89.88	269.09	0.0	0.0	0.0	0.0
19	81.42	-52.08	-273.94	0.132	0.0	0.0	-89.88	269.09	0.0	0.0	0.0	0.0
20	43.04	-51.28	-273.89	0.128	0.0	0.0	-89.88	269.09	0.0	0.0	0.0	0.0

PSI = 120.	U-HUB =	269.60	V-HUB =	4.67	W-HUB =	-69.62	GEO. PITCH =	15.79	BETA(HUB) =	2.13		
STA	UT	JP	UR	MACH	ALPHA	ALPHAD	THETAD	THETADD	CL	CD	CDSF	CM
1	1003.11	-115.10	141.50	0.913	0.09	104.85	53.83	1863.56	-0.0667	0.0447	0.0070	-0.0344
2	961.66	-112.56	141.49	0.878	0.43	103.87	53.83	1863.56	0.0052	0.0315	0.0070	-0.0265
3	923.21	-110.03	141.49	0.844	0.77	102.79	53.83	1863.56	0.0296	0.0234	0.0071	-0.0431
4	884.75	-107.49	141.48	0.809	1.10	101.57	53.83	1863.56	0.1074	0.0173	0.0071	-0.0385
5	846.32	-104.96	141.47	0.774	1.41	100.19	53.83	1863.56	0.1587	0.0159	0.0072	-0.0323
6	807.87	-102.43	141.46	0.739	1.71	98.62	53.83	1863.56	0.2013	0.0146	0.0072	-0.0289
7	769.42	-99.89	141.45	0.704	2.00	96.82	53.83	1863.56	0.2379	0.0119	0.0073	-0.0304
8	730.97	-97.36	141.44	0.669	2.27	94.75	53.83	1863.56	0.2689	0.0113	0.0073	-0.0334
9	692.52	-94.82	141.43	0.634	2.51	92.34	53.83	1863.56	0.2948	0.0102	0.0074	-0.0347
10	654.08	-92.29	141.43	0.599	2.74	89.52	53.83	1863.56	0.3156	0.0094	0.0075	-0.0343
11	615.63	-89.76	141.42	0.564	2.93	86.19	53.83	1863.56	0.3313	0.0084	0.0075	-0.0350
12	577.18	-87.22	141.41	0.529	3.09	82.20	53.83	1863.56	0.3368	0.0084	0.0076	-0.0352
13	538.73	-84.69	141.40	0.494	3.20	77.38	53.83	1863.56	0.3103	0.0086	0.0077	-0.0329
14	500.28	-82.15	141.39	0.460	3.27	71.47	53.83	1863.56	0.2745	0.0089	0.0078	-0.0302
15	461.84	-79.62	141.38	0.425	3.27	64.11	53.83	1863.56	0.3429	0.0092	0.0079	-0.0380
16	423.39	-77.09	141.37	0.390	3.19	54.78	53.83	1863.56	0.3280	0.0094	0.0080	-0.0391
17	384.94	-74.55	141.37	0.355	3.00	42.67	53.83	1863.56	0.2966	0.0097	0.0081	-0.0413
18	346.49	-72.02	141.36	0.320	0.0	0.0	53.83	1863.56	0.0	0.0	0.0	0.0
19	308.05	-69.48	141.35	0.285	0.0	0.0	53.83	1863.56	0.0	0.0	0.0	0.0
20	269.60	-66.95	141.34	0.250	0.0	0.0	53.83	1863.56	0.0	0.0	0.0	0.0

Figure 44. Typical Airloads Output.